Cover Page

The handle holds various files of this Leiden University dissertation.

Author: Franse, J.
Title: Hunting dark matter with X-rays
Issue Date: 2016-12-20

Hunting Dark Matter with X-rays

Jeroen Franse

Hunting Dark Matter with X-Rays

Proefschrift

ter verkrijging van
de graad van Doctor aan de Universiteit Leiden,
op gezag van Rector Magnificus prof. mr. C.J.J.M. Stolker,
volgens besluit van het College voor Promoties
te verdedigen op dinsdag 20 December 2016
klokke 10.00 uur

door

Jeroen Franse

geboren te Maarssen
in 1988

Promotor: Prof. dr. Ana Achúcarro
Co-promotor: Dr. Alexey Boyarsky

Promotiecommissie: Prof. dr. I. Tkachev (Institute of Nuclear Research, Moscow, Russia)
                     Prof. dr. E.R. Eliel
                     Prof. dr. H.J.A. Röttgering
                     Dr. O. Ruchayskiy (Niels Bohr Institute, Copenhagen, Denmark)
                     Dr. J. Vink (Universiteit van Amsterdam)

Cover by Caroline Toxopeus

CONTENTS

1 | Introduction

1.1 The Case for Dark Matter

The first time the existence of Dark Matter was formulated as such was by Zwicky (1933), in order to explain the large discrepancy observed between the velocities of members of the Coma galaxy cluster and the amount of luminous matter present that could induce those velocities. One of the most important bodies of work that led to the common acceptance of Dark Matter as a phenomenon was that regarding the rotation curves of spiral galaxies. As early as the 1940's (Oort, 1940) it was observed that galaxy rotation curves tended to flatten out towards the outskirts and the mass-to-light ratio increased dramatically, and by the 1980's the influential work of e.g. Rubin et al. (1980) had firmly established this line of reasoning.

Currently, the existence of Dark Matter is a well established astrophysical phenomenon and is one of the components of the ΛCDM standard model of cosmology. In that framework, only 6 parameters are required to accurately describe the expansion history of the universe, the cosmic microwave background, the primordial elemental abundances and the formation of the large scale structures of the universe. It tells us that the total energy density of the Universe at current times consists of only about 5% known matter, 70% Dark Energy (denoted by Λ and responsible for the accelerated expansion of the universe although its nature is completely unknown) and 25% of Dark Matter.

Not only in the spiral galaxies that were mentioned above, but in all types of galaxies the presence of Dark Matter is required to explain the dynamics of stars and gas, from the dwarf satellites of the Milky Way, to the largest of elliptical galaxies (Corbelli et al., 2010; Dekel et al., 2005; Bertone et al., 2005; Walker, 2013).

In clusters of galaxies, the dynamics of the member galaxies (measured by their velocity dispersion) imply very large mass-to-light ratios in a similar fashion to the stellar dynamics in elliptical galaxies. This argument is strongly corroborated by X-ray observations. The gas trapped by the gravitational well of the galaxy cluster becomes a very hot plasma, balancing internal thermal pressure and the forces of gravity. The X-rays this plasma emits depend on its temperature and its density, which in turn also depend on the total gravitational mass. It has been shown that the density of the emitting plasma can

only account for about 15% of the total gravitational mass required to induce the high temperature and high emissivity observed (e.g. Vikhlinin et al., 2006).

Studies of the large scale structure of the universe all show that Dark Matter is required for the structures that we observe to have been able to form. This is usually expressed through the matter power spectrum, which describes the amount of clustering on a particular length scale. It is possible to measure the matter power spectrum through various techniques, such as galaxy redshift surveys (e.g. Colless et al., 2001), with the Lyman-alpha forest (Viel et al., 2004), and gravitational lensing cosmic shear surveys (e.g. Kaiser, 1992; Hoekstra & Jain, 2008). These measurements can be compared both to analytical descriptions of the power spectrum at different redshifts based on the theory of gravitational collapse (Press & Schechter, 1974), and to large cosmological simulations (e.g. Springel et al., 2005). In all cases, the observations and the theory (analytical or from simulations) require Dark Matter in order to be consistent (Frenk & White, 2012).

Measurements of the Cosmic Microwave Background (CMB) radiation have been instrumental for our understanding of cosmology in general, but regarding the Dark Matter it is also one of the strongest single pieces of evidence. The fluctuations in the otherwise homogeneous CMB sky are caused by acoustic oscillations of the primordial hot plasma frozen at the moment the plasma recombined. The oscillations were originally seeded by quantum fluctuation that generated small under- and over-densities, which started growing. The potential wells attracted plasma and radiation, which produced its own internal pressure to counteract gravity (Hu & White, 1996; Bennett et al., 2013). This back-and-forth depends on the amount of gravitating matter and the amount of pressure-generating particles. The fluctuations in the CMB at different scales encode information about the scales of the under- and over-densities, and in which phase of the oscillation they existed at recombination (the moment the universe became transparent, and the CMB was emitted). This information is extracted from the statistics of these fluctuations and it indicates that most of the gravitating mass was not producing any internal pressure, and can therefore not be any known form of matter.

In addition to the above, there are also experiments that confirm not necessarily the existence of Dark Matter directly, but rather some of the other ΛCDM-parameters and thereby indirectly the Dark Matter by requiring consistency across observations.

One of these is Big Bang Nucleosynthesis (BBNS), the process by which the first atomic nuclei form out of the primordial plasma, between roughly 1 and 3 minutes after the Big Bang. Although Dark Matter itself does not influence the processes, the abundances of the various elements at the end of BBNS is determined among other things by the density of the baryons participating in the process. By comparing the BBNS calculations with observations of the primordial abundance of the light elements, it was determined that the baryons can only contribute about 5% of the total mass-energy budget of the universe (Dar, 1995; Olive et al., 2014, chap. 23).

The expansion of the universe depends on the content of the universe through the laws of General Relativity, namely the energy density of all gravitating mass and that of Dark Energy (also that of radiation in the early Universe). The expansion of the universe has been measured with Type 1a Supernovae up to high redshift (Kowalski et al., 2008), and together with the CMB is able to constrain both the total mass and the Dark Energy density (about 30% and 70% respectively). Coupling this result to, for example, the results of the

BBNS, the conclusion is that 25% of the universe has to consist of Dark Matter.

Strikingly, the varied and independent evidence described above doesn't just indicate the existence of Dark Matter, they all indicate the *same abundance* of Dark Matter.

1.2   The Nature of the Dark Matter

1.2.1   Known Properties

Although most of the properties of the Dark Matter remain unknown, there are a number of characteristics that it must have that are currently known.

First of all, the Dark Matter can not be made up of any known, baryonic, matter. Although this argument has been touched upon in the previous section, it is important to acknowledge it explicitly. The study of the Bullet Cluster (Markevitch et al., 2004; Clowe et al., 2006) is famous for showing that the baryonic matter and the bulk of the gravitating mass do not spatially coincide. Most of the baryonic matter in galaxy clusters is in the form of hot X-ray emitting plasma and can be mapped using X-ray observations. The Bullet cluster is an ongoing merger of two galaxy clusters, where the cluster cores haves crossed once already. The hot plasmas of both clusters collided with each other, causing observable shock-fronts. The total gravitational mass can be mapped using gravitational lensing techniques, which do not distinguish between any dynamical or internal states of the gravitating mass, as long as it gravitates. This comparison showed that the bulk of the clusters' mass had passed right through each other without interacting (colliding). This is not only evidence for the existence of Dark Matter, but also that it does not interact with itself nor with normal baryonic matter.

The caveat that must be made with the Bullet cluster study is that on its own, it leaves open the possibility that the Dark Matter consists of very compact objects of baryonic matter. If they are compact enough, their number density can be small enough that they hardly interact with each other, and are practically unobservable in any direct manner. This kind of Dark Matter is commonly referred to as MACHOs, Massive Compact Halo Objects. However, this possibility is precluded by micro-lensing studies that have specifically studied the existence of these MACHOs by counting the number of events in which a heavy, compact, dark object passes in front of a star and thereby changes its flux and light curve due to gravitational lensing effects (Alcock et al., 2000; Tisserand et al., 2007; Moniez, 2010). The CMB also rules out any baryonic interpretation of the Dark Matter, as described in the last Section.

Secondly, then, if the Dark Matter is some non-baryonic particle, it must be dark, pressure-less, and non-selfinteracting up to a large extent. As was described, the Dark Matter must not participate in the acoustic oscillations that are inscribed onto the CMB, and it must not influence the BBNS. Interaction with the electromagnetic forces would violate both these conditions, hence it is *dark*. Any considerable self-interaction would contradict the results from the Bullet Cluster.

Thirdly, some restrictions on the Dark Matter particle mass exist. If the particles are fermionic, they have to comply by the Pauli-exclusion principle – essentially setting a maximum phase-space density. It has been found that in dwarf galaxies, this principle would be violated if 100% of the Dark Matter is in the form of particles that are lighter than a few hundred eV, known as the Tremaine-Gunn bound (Tremaine & Gunn, 1979).

Another lower bound on the Dark Matter particle mass, whether it is fermionic or not, comes from structure formation. The velocity distribution of the Dark Matter particles suppresses the gravitational collapse of overdensities below a certain scale, known as the free-streaming length. Since Dark Matter can not cool by radiating energy, an overdensity cannot collapse further than the thermal velocities allow. Structures of a small enough scale are washed out in this manner. The scale below which this happens is set by the particles' (distribution of) velocities, which, if they are produced from the primordial plasma, tend to follow thermal or near-thermal spectra according to their mass; lighter particles have higher velocities. This property can be used to classify particles as being either *hot* or *cold* Dark Matter, where cold Dark Matter becomes non-relativistic (due to the expansion of the universe) before matter-radiation equality, and hot Dark Matter only becomes non-relativistic very late into the matter-dominated epoch. It has been found from cosmological structure formation simulations that hot Dark Matter produces top-down formation of structures, ie., large scales collapse first and then fragment into smaller objects during the expansion of the universe. This is opposite to the behaviour that is observed, where small scales form first to later merge into larger objects, the so-called hierarchical scenario. This rules out hot, and therefore light, Dark Matter (Bertone et al., 2005). A grey area exists in between hot and cold Dark Matter, called *warm*, where current state-of-the-art cosmological measurements and simulations still allow for a particle as light as a few keV (Lovell et al., 2013; Garzilli et al., 2015).

Note that the conditions described above also rule out standard model neutrinos. Although neutrinos are indeed non-baryonic and electrically neutral, their masses are constrained to be at the eV scale or below from both detector and cosmological experiments (Komatsu et al., 2011; Olive et al., 2014). In addition, the relic number density of neutrinos (those having been produced during the early universe) is known, which would require neutrino masses of order 10 eV in order to explain 100% of the Dark Matter (Lesgourgues & Pastor, 2006).

Lastly, the Dark Matter must be stable or at least cosmologically long-lived, and it must have been produced in the early universe in the right quantities.

1.2.2 Dark Matter Candidates

Many explanations for the Dark Matter have been put forward over the years. A limited selection will be discussed in this section.

There are a few theories that attempt to explain the phenomena associated with Dark Matter by modifying the laws of gravity. These include MOND (Milgrom, 1983), TeVeS (Bekenstein, 2004), and various modifications of General Relativity. These modified gravity theories can typically explain observations without the need for Dark Matter in some cases but not in others. For example, both MOND and TeVeS can explain galaxy rotation curves quite well by invoking a pivot scale in the acceleration. However, they fail to explain the physics of galaxy clusters without resorting to extra hidden mass after all. For discussion see f.e. Dodelson (2011); Moffat & Toth (2011) and for a review Sanders (2014) . Regarding the other pillars of the ΛCDM cosmology, the expansion history of the Universe is compatible with many modified gravity theories (due to a certain amount of freedom in those theories, the expansion is not a strict prediction), although the CMB and structure formation are a matter of intense debate hampered by the limited resources

that are available for large scale simulations of modified gravity theories (Famaey & Mc-Gaugh, 2012).

There is no experimental nor theoretical reason that dictates that Dark Matter *can not* be a particle, nor that it *should* be a particle. However, the predominant class of explanation is the particle explanation, where Dark Matter is some kind of as-yet undiscovered particle, since this is extremely plausible. The Standard Model (SM) of particle physics is a very successful theory and can describe a huge wealth of physics, but despite that, there are a few so-called 'beyond the standard model' phenomena that it cannot explain and probably require new physics or new particles (Ellis, 2012; Gripaios, 2015). Fortunately, there is plenty of room in the SM for extensions and new particles where the new parameters are such that constraints from current experiments are avoided.

One of the most popular Dark Matter particle candidates is the Weakly-Interacting Massive Particle, or WIMP for short. This is a particle that interacts with the SM with a cross-section at the scale of other Weak interactions. The popularity of this kind of Dark Matter stems from the fact that at this interaction strength, the Dark Matter can be produced at the correct cosmological abundance for a large range of masses (GeV – TeV; Lee & Weinberg, 1977). Many SM particles are lighter than this mass however, meaning that the WIMP would decay to SM particles quite rapidly unless it is prevented from doing so by having a new symmetry charge. Additionally, many extensions of the SM that had been invented to explain other phenomena (e.g. Supersymmetry), naturally include a WIMP-like particle that can play the role of the cosmological Dark Matter. Many experiments, both direct and indirect, have been performed or are being set up to search for these particles. As of yet, no convincing detections have been reported (Baudis, 2013; Conrad, 2014).

Another possible Dark Matter candidate is the Axion. Some experiments for directly detecting Axions are underway, and like some of the WIMP-like particles, the Axion was not originally 'invented' to explain the Dark Matter. It is required to solve a 'beyond the standard model' problem, and it is often considered that the existence of the Axion is almost guaranteed, albeit not necessarily in a form that can be the the cosmological Dark Matter. The problem the Axion would solve, is that of the suspiciously small neutron electric dipole moment, or more generally the lack of observed CP-violating processes in quantumchromodynamics (Peter, 2012). The kind of Axion that could play the role of cosmological Dark Matter is of the order of 10 μeV. Despite its very low mass, it would not be hot Dark Matter (with all the impossibilities that entails) since they would be created with zero momentum.

The so-called hidden sector may theoretically harbour many particles that have no interaction with the SM electroweak or strong interactions. The existence of a hidden sector is an open question, but the possibility is invoked often in the context of constructing a Grand Unified Theory, or to solve another problem in the SM (like the gauge hierarchy problem). In principle, hidden sector particles are uncharged with respect to the SM, but despite that the hidden sector can have many non-trivial effects on SM phenomenology in complicated ways. With plenty of room for new physics, the hidden (sometimes also called dark) sector contains candidates such as the dark photon or asymmetric Dark Matter (Feng & Kumar, 2008; Ackerman et al., 2009; Kaplan et al., 2009).

Many more Dark Matter hypotheses exist than it is possible to cover in this work. In the next Section, we will examine the class of Dark Matter particle that is most relevant

to the work in this Thesis.

1.3   Decaying Dark Matter

The general class of candidate Dark Matter particles that has not been covered above is the kind of Dark Matter that is allowed to decay. The work in this thesis relates specifically to this class of Dark Matter, but is otherwise largely model-independent. The Section starts with a description of the expected astrophysical signals from this kind of particle, followed by examples of decaying Dark Matter particle from theory, finally one of which - the sterile neutrino - is discussed in a little more detail.

1.3.1   Signal Properties of Decaying Dark Matter

In general, any decaying Dark Matter particle of fermionic nature with a mass below that of two electrons will have a (sub-dominant) decay channel into an active neutrino and a photon. For bosonic particles, the relevant decay channel will be to two photons. Since both products' masses are negligible compared to the Dark Matter particle, both will carry half the centre-of-mass energy, which is half the Dark Matter particle's mass. This creates a monochromatic spectral line. From considerations regarding the minimum mass of the Dark Matter particle from phase-space density arguments and structure formation (Section 1.2.1) and from previous experiments (Section 1.5.3), this line should be emitted at an energy somewhere in the X-ray regime. The signal will have the following characteristics:

- The energy of the monochromatic line is somewhere in the X-ray regime, at half the Dark Matter particle's mass, redshifted according to the cosmological distance to the source of the decay.

- The width of the spectral line is then only due to velocity broadening of the Dark Matter in a particular object ($\Delta E/E$ roughly between 10^{-2} and 10^{-4} depending on the object).

- The strength of the line is a function of lifetime of the particle, the number of particles in the telescope's field-of-view, and the cosmological distance to the object as follows:
$$F_{DM} = \Gamma_{DM} \frac{M_{FoV}}{m_{DM}} \frac{1}{4\pi D_{lum}^2}$$
with F the detected flux, Γ the decay rate, M_{FoV} the total Dark Matter mass in the field-of-view, m_{DM} the Dark Matter particle mass and D_{lum} the luminosity distance to the object.

1.3.2   Cosmological Effects of Decaying Dark Matter

The properties of Dark Matter have an influence on various areas of astrophysics and cosmology, which is why the existence of the Dark Matter could be deduced, and also provides an avenue for testing indirectly the nature of the Dark Matter, as has been discussed before. To date however, no 'exotic' properties have been established. The measurements are consistent with Dark Matter being cold, having no self-interaction nor interaction with

other particles, not annihilating and not decaying (Section 1.2). Limits on these properties have been set though, and there is still a large range of allowed Dark Matter particle candidates with room for currently undetectable exotic properties.

For the specific case of decaying Dark Matter, there are a number of ways that its existence may be tested for indirectly, other that observing its decay products. Conversely, if we know that Dark Matter is of the decaying sort, these are fields that will benefit from this knowledge. Having determined that the decaying Dark Matter mass is likely in keV-regime, this makes the Dark Matter *warm*. The effect of this (see also Section 1.2) is to suppress the formation of small-scale structures. Depending on the exact particle mass and velocity spectrum (linked to its production mechanism), this happens at scales roughly corresponding to dwarf satellite galaxies. This effect can be measured in principle through the power spectrum from Lyman-alpha forest surveys (Garzilli et al., 2015), gravitational lensing, clustering surveys, or a census of the dwarf galaxies of the Milky Way and Andromeda galaxies (Schneider, 2016). In addition, warm Dark Matter is shown to change the mass profiles of dwarf galaxies, making the central densities more cored (Lovell et al., 2012), and modifying the mass-concentration relation (Schneider, 2015). It is currently debated if these effects may be degenerate with baryonic physics and the details of galaxy formation (Weinberg et al., 2013).

1.3.3   Decaying Dark Matter Candidates

The work in this thesis is applicable to any Dark Matter candidate particle that exhibits a signal as described in the section above. Since any potential Dark Matter signal discovered is likely to be discovered at relatively low significance and therefore with large uncertainties, the methods described in this Thesis may also be sensitive (up to a point) to particles that produce X-ray signals with similar but somewhat different behaviour.

The bahaviour described in Section 1.3.1 will be exhibited by any radiative decay process, where the rate is sufficiently independent of prior particle interactions or processes, like slowly decaying or milicharged Dark Matter (El Aisati et al., 2014; Frandsen et al., 2014). Low mass annihilating Dark Matter would show different morphology and scaling between objects since the signal should follow the Dark Matter density squared (Frandsen et al., 2014). Axion or Axion-like particles (ALPs) may decay or convert in magnetic fields, causing an additional scaling with the magnetic field strength (Cicoli et al., 2014; Alvarez et al., 2015; Higaki et al., 2014). Dark Matter that can exist in excited states and therefore emit upon de-excitation, could depend on parameters like the Dark Matter density squared or Dark Matter velocity distribution (Finkbeiner & Weiner, 2014). Additional emission features could also be produced by multi-component or composite Dark Matter, like dark atoms (Cline et al., 2014).

See references in Iakubovskyi (2014) for a more extensive sample of particle models like this.

1.3.4   Sterile Neutrinos

It is informative to describe in a little more detail one specific candidate decaying Dark Matter particle, and it shall be used throughout as our benchmark particle.

The Standard Model (SM) of particle physics can be extended by a number of so-called sterile neutrinos. These particles are similar to the neutrinos found in the SM (referred to as active neutrinos in that case), but carry no charge of any sort and are more massive than the active neutrino. Having no charge, they do not formally participate in any fundamental interactions except through gravity, hence the name. They do however mix with the active neutrinos through the neutrino oscillations, effectively participating in the weak interaction at a suppressed level. A description of this interaction can be expressed in terms of the effective characteristic interaction strength θG_F. Typical interactions of the Weak force have a characteristic strength of G_F, the Fermi constant. The effective interaction of the sterile neutrino with the active neutrinos is *superweak* with the mixing angle $\theta \ll 1$.

The Neutrino Minimal Standard Model (or νMSM for short) is a minimal extension of the SM that introduces three sterile neutrinos and is able to solve three major 'beyond the standard model' problems; the existence of Dark Matter, the generation of the matter-antimatter asymmetry, and the neutrino masses (see Adhikari et al. (2016) for an extensive review).

Active neutrinos are observed to have a non-zero mass through their oscillations. The three flavours of neutrino oscillate between each other, which is only possible if their mass eigenstates are different from their flavour eigenstates. It is not possible to measure the neutrino masses directly, but the squares of the mass differences are available experimentally. In the SM, neutrinos are formally massless however, and to generate their mass new physics is needed beyond the SM. The reason neutrino mass is not included in the SM, is that massive fermions have to come in left- and right-handed chiral states, but only left-handed neutrinos (and right-handed anti-neutrinos) have ever been observed. The sterile neutrinos are the right-chiral counterparts to the left-handed active neutrinos, providing the mechanism for generating active neutrino masses by allowing them to interact with the Higgs field, which is the usual way to generate masses in the SM. The masses of the sterile neutrinos however, are Majorana masses and are not caused by the Higgs mechanism (which is only possible because it is a singlet under all fundamental interactions, in other words it has no charges). This means that it constitutes an entirely new, unrelated mass scale and as such would classify as 'beyond the standard model' physics. In order to generate the masses required for the flavour oscillations for three flavour states, at least two sterile neutrinos are needed (leaving the third active neutrino massless still, which is currently allowed by experiment).

By adding a third sterile state (making all three active neutrinos massive), it becomes possible to simultaneously explain neutrino oscillations and the Dark Matter. Sterile neutrino Dark Matter was first described by Dodelson & Widrow (1994) and the idea was further refined by Shi & Fuller (1999); Abazajian et al. (2001); Dolgov & Hansen (2002); Asaka et al. (2005) and Boyarsky et al. (2009c) among others. In this case the lightest sterile state plays the role of the Dark Matter and is cosmologically long lived. This is possible if the mixing with the active sector is very small ($\theta \ll 1$). Consequently this lightest sterile neutrino cannot generate the active neutrino masses (which is contributed to as $\delta m_\nu \sim \theta^2 m_{DM}$), but the other two sterile neutrinos are massive enough and have enough mixing to explain the observed mass differences in the active neutrino oscillations.

By requiring that the two more massive sterile neutrinos are at least as massive as $\mathcal{O}(100 \text{ MeV})$ and nearly degenerate with each other ($\Delta M_{12} \ll M_{1,2}$), it is possible to

generate the matter-antimatter asymmetry in the early universe. Schematically, at these temperatures, active-sterile mixing is large, changing active neutrinos into the heavier sterile neutrinos which in turn decay into the lightest sterile neutrino. Because the mixing of the lightest sterile state is very weak, these particles are produced out of equilibrium, meaning that the reverse process at this point has a cross-section so small that the reaction rate has become negligibly small. In the presence of CP-violating processes (ie., processes that can violate baryon- or lepton-number), this decay effectively hides away the matter-antimatter (lepton-antilepton) asymmetry in a dark and light sector. This process allows the Dark Matter relic abundance to be set to the required level according to the size of the lepton-asymmetry and the active-sterile mixing.

The choice for the sterile neutrino Dark Matter as a benchmark model and main inspiration for the search for decaying Dark Matter is due to the attractively elegant solution of three of particle physics' and cosmology's largest open questions with a single extension of the SM model. We reiterate nevertheless that the work in this thesis can be applied to any decaying Dark Matter, as described in the previous Sections.

1.4   X-Ray Astronomy

Since the decay of Dark Matter would produce X-ray spectral features, this section will describe aspects of X-ray astronomy relevant to observing it in general terms. Details regarding individual instruments can be found in the relevant Chapters and references therein.

1.4.1   X-ray Instruments and Data Processing

The current generation of X-ray telescopes use hyperbolic mirrors with specialized coatings to direct the incoming high-energy photons to CCD-like detectors for both imaging and spectroscopic analyses. The three major observatories like this in the regime covering roughly 0.1 keV to 10 keV are *XMM-Newton*, *Chandra* and *Suzaku*. They each have their own strengths and weaknesses, but often similar science can be performed with each. With regards to imaging spectroscopy the main differences are that *XMM-Newton* has the largest field-of-view and 'grasp' (the product of the FoV and effective area, see below), while *Chandra* offers the best spatial resolution and *Suzaku* exhibits relatively low background levels.

The X-ray observatories are space telescopes in highly elliptic orbits. In this way, in the phase where they are far away from Earth, they can avoid the radiation belts that would pollute any data taken to a point beyond usability. Even with this precaution however, high-background periods of non-X-ray events still occur, and are often associated with soft proton flares (SPF). These are clouds of highly energetic charged particle emitted by the sun for example, and they create artificial events in the detectors. One of the first steps in the data reduction is therefore to completely remove high-background periods. This is usually referred to as lightcurve cleaning or flare removal.

X-ray imaging CCD's are capable of registering the photons' energy as well, providing imaging spectroscopy capabilities. This is the primary data that is used throughout the work presented in this thesis. The energy registration is not perfect, and the probability

that an incident photon with a particular energy is detected with some other energy depends itself on the photon energy (the typical spectral resolution for such instruments is of the order 100 eV). This can be described by a probability matrix that encodes the chance that a photon of energy E is detected with energy E', and is called the redistribution matrix. Typically, this matrix is recalculated for every observation based on ray-tracing simulations of the telescope assembly, calibration measurements, telescope attitude information, and the actual data. The produced file is usually referred to as the RMF.

Whether or not an incident X-ray photon is detected by the instrument is a complicated function of energy and incident angle. This is mainly caused by the mirror materials and assembly, but other parts of the telescope influence this as well. The resulting detection efficiency is expressed as an effective area in units of cm^2. This represents the total collecting area of the telescope corresponding to the hypothetical situation where the telescope's efficiency would be 100%. The effective area is calibrated by measurements on the ground and in-flight, with varying techniques, but as a function of incident energy it has to be recalculated as well for each observation. This is also because of an effect called vignetting, where the effective area of the telescope assembly is reduced towards the edges of the field-of-view. The resulting description of the effective area for a given observation is referred to as the ancillary response file or ARF for short.

X-ray detectors are prone to exhibiting strong levels of in-flight instrumental backgrounds. These are mostly caused by high-energy particle hitting the telescope and chip assemblies, which induce a cascade of secondary particles that can be in turn detected by the sensor arrays. This instrumental background has a characteristic spatial and spectral distribution related to the construction and materials of the camera. There are various strategies to account or correct for the instrumental backgrounds. One is to determine all the backgrounds (instrumental plus sky) from a nearby detector region outside the region of interest. Another is to obtain observations made while the telescope is in a calibration mode. For example, in the case of *XMM-Newton* this means using a blocking filter to exclude anything but the instrumental backgrounds from being detected. This observation can then be subtracted from the original spectrum. Lastly, one may model the instrumental background simultaneously with the rest of the spectrum. This requires some prior knowledge on the components expected to be present in the instrumental background, for example obtained from the calibration observations mentioned previously. The instrumental background is prone to some variability in time, inducing some systematic uncertainty and necessitating the renormalization of the presumed description of the instrumental background for each (set of) observations.

As mentioned, for every observation the telescope calibration (redistribution matrix and effective area and background if needed) has to be recalculated. In fact, since these are functions of the relative position in the field-of-view (position on the CCD), this will have to be done for every separate extraction region. All necessary data products are generated using analysis software packages particular to the instrument being used (these will be mentioned in the relevant Chapters). Once they have been obtained one can start analyzing the spectra. This is done through a process called forward-modeling. In particular because the redistribution matrix is a very non-trivial matrix, it is mathematically impossible to convert a detected spectrum back to a true emitted spectrum analytically. Therefore the only possibility is to assume a model for the true emission, propagate it through the description of the telescope's response (using the RMF and ARF files), evalu-

ate the goodness-of-fit, and repeat until an acceptable fit to the data is found. The software used in this Thesis for that purpose is XSPEC (Arnaud, 1996), but other packages are also available (f.e. SPEX, Kaastra et al., 1996).

1.4.2   Sources in the X-Ray Sky

In order to search for X-ray signals from decaying Dark Matter, one must be able to identify the X-rays emitted by any other astrophysical sources or backgrounds first. This section offers an overview of the most important and common sources and their X-ray features.

An extended halo of hot, low-density gas surrounds the Milky Way, and emits a thermal brehmstrahlung component peaking in the soft X-rays ($T \approx 0.2$ keV). Even when observing away from the galactic center or the galactic plane, this component is present and may need to be accounted for at lower energies (Lumb et al., 2002).

The point sources that can be found in the X-ray sky mostly include AGN in the extragalactic regions, and stellar binaries or pulsars in the Galaxy (Brandt & Hasinger, 2005). Deep observations will also start to pick up faint starburst galaxies (Worsley et al., 2006). These objects have characteristic X-ray spectra, but can be easily selected and removed due to their point-source nature.

Unresolved point sources lead to (a contribution to) the extragalactic X-ray background. This background has been an object of study for many decades now. It is currently agreed that the major contribution to the XRB is from unresolved AGN, although some uncertainty remains as to the precise make-up of the XRB. Measurements by various X-ray observatories indicate that the spectral shape of the XRB is a relatively simple, clean powerlaw with a slope of ~ -1.4 (De Luca & Molendi, 2004).

Galaxy clusters are the most massive bound structures in the Universe. As a result, their potential wells accrete large amounts of gas and heat this gas to very high temperatures. A relaxed cluster, which is to say a cluster whose gas has reached hydrostatic equilibrium, has a smooth temperature gradient and the main emission component is a brehmstahlung continuum based on the temperature and density of the gas (Arnaud, 2005), typically peaking between 2–10 keV. The other important component of cluster X-ray emission is from the various ions of various elements present in the gas. The atoms in the hot plasma are highly ionized and are continually collisionally and radiatively excited, and subsequently also de-excite and in doing so will emit photons at wavelengths characteristic to the transition. So, each population of ions in the plasma produces its own characteristic set of emission lines. The strength of those emission lines depends on the abundance of the element and the temperature of the plasma. The relationship between the emmissivity of the various lines emitted by a plasma is very non-trivial and non-monotonic due to the complex interplay between the various ionizing, radiative and collisional processes. A particular emission line will typically peak at a single temperature, and have reduced intensity at higher or lower temperatures. Therefore, the relative intensities of lines produced by the same ion are a good tracer of the plasma temperature (Boehringer & Werner, 2009).

Galaxies are less massive and contain less gas than clusters of galaxies, meaning that their X-ray emission is dimmer, and peaks at lower energies. The brighter elliptical galaxies typically show temperatures of ~ 1 keV, dropping to ~ 0.1 keV for fainter

galaxies (Sarazin, 1997; Lehmer et al., 2007). Some atomic lines can still be excited, although at much lower luminosities than in clusters, since the densities are lower.

1.5   Search Strategy for Decaying Dark Matter X-Ray Signals

Taking into account the considerations regarding the properties of the Dark Matter decay signal (Section 1.3.1) and regarding the practicalities of X-ray astronomy (Section 1.4), in this Section the strategy for searching for decaying Dark Matter is detailed.

   Two main modes of reasoning can be applied to the search. In a nutshell, the first one is to rule out, on an object-by-object basis, with high confidence all other interpretations until only one (Dark Matter decay) would be left. The second is to take a more holistic approach and judge measurements from a large range of objects and environments simultaneously against the Dark Matter decay interpretation directly. The latter, the holistic line of argumentation, is expected to yield more useful results in the face of measurements with large uncertainties. This approach receives preference in the work throughout this Thesis. Although the technical aspects of both are essentially the same, it is the 'philosophy' regarding how to answer the fundamental question and judge the measurements that is different for each. Below those differences and similarities, and their strengths and weaknesses are discussed.

1.5.1   Single Objects

To be able to detect a Dark Matter decay spectral line (described in Section 1.3.1), the X-ray spectrum of the object under consideration must be well fit with an appropriate model describing all of the components that may be expected for that object. Since the signal of decaying Dark Matter will be a weak line (seeing as no strong Dark Matter decay lines have been observed yet), it is imperative that the fit is of high quality, with a reduced-χ^2 close to one. If the residuals from the fitting of this spectrum exhibit a significant positive line-like deviation from zero that can not be identified with astrophysical emission or instrumental lines, this may be an indication of a candidate decaying Dark Matter signal.

   If one wants to be able to claim a Dark Matter detection based on a single object (a single spectrum), it is necessary to exclude all possibilities of the spectral line being an artifact or an emission feature from regular astrophysical processes. This requires very careful fitting of the spectrum and thorough testing of these fits. As described in Section 1.4.2, the emission lines from the hot plasma depend non-trivially on the temperature, density and abundances, and is therefore also different for different objects. The positions and possible emissivities of a huge number of lines are known and available in databases. However, the spectral resolution of the current generation of X-ray imaging spectrometers is of the order 100 eV, which means that many lines tend to blend together, and can also obscure the continuum level in spectral regions with many excited lines. In addition, the cumulative spectrum of a relatively large extent of an object will often contain a superposition of multiple different components with different temperatures or elemental abundances, which in some cases may introduce degeneracies in the fitting process. There are various strategies for determining the various continuum and line contributions, and

they will be described in the relevant Chapters in this Thesis. In brief, as also described in Section 1.4.2, it is possible to use certain (combinations) of stronger emission lines to constrain reasonably well temperatures and abundances.

Source selection for this approach is mostly a balancing of the expected signal strength with the expected astrophysical emission 'background' and the associated complications in the spectral modeling (high signal and high background in clusters and the Galactic center, lower signal and lower background in galaxies and dwarf galaxies).

As will be evident throughout the Thesis, this approach delivers results on some single objects where it can be shown that atomic line emission is very unlikely to be the origin a certain candidate signal, although it is very difficult to completely rule out such scenarios. In other objects, however, this is not always the case and multiple valid interpretations of the physical properties of the plasma can be found. Especially with the quality of the current generation of instruments, this issue often can not be easily or definitively resolved for the weak signals that are (expected to be) found.

Therefore, it is prudent to adopt a holistic approach that retains the high quality fitting, but compares results between objects in order to confirm or reject hypotheses as to the origin of a candidate signal.

1.5.2 Holistic Approach

The obtaining of high-quality fits and accurate estimates of possible contaminating factors described above is still part of this approach, but the central methodology by which to differentiate between scenarios is different.

Here, we make us of the fact that the signal strength of a Dark Matter decay signal depends on the total Dark Matter mass inside the field-of-view (FoV) of the telescope and the distance to the object. This is because decay is a single-body process, so that essentially the signal scales as the column-density of objects. Conveniently, as long as a given object fits inside the FoV of the telescope, a more massive but further away object will tend to provide similar signal strength. Therefore, appropriate targets for observations for searching for a decaying Dark Matter signal include all of the following. Dwarf galaxy satellites of the Milky Way halo, the Galactic Center, low redshift galaxies, and galaxy clusters.

Since the astrophysical environments of these objects are very different, and the regular X-ray emission likewise exhibits large differences, this allows for a robust and comprehensive test as to the origin of any unidentified spectral feature. For example, line emission from hot plasma scales with the temperature, with the square of the plasma density and with the elemental abundances. Continuum emission scales with temperature and density squared. But Dark Matter decay just scales with the Dark Matter mass. This holds not just for the expected scaling between objects, but also spatially within each individual object. Comparing the strength of a candidate signal in different environments to the expected scaling in those environments could provide robust conclusions regarding the origin of a potential signal.

With the spectral resolution of the current generation of detectors, a weak spectral feature may be localized to about 50 eV. It should therefore be noted that in this way potential Dark Matter decay spectral features that are detected within 50–100 eV (restframe) of each other in different observations, are to start with implicitly assumed to be emitted
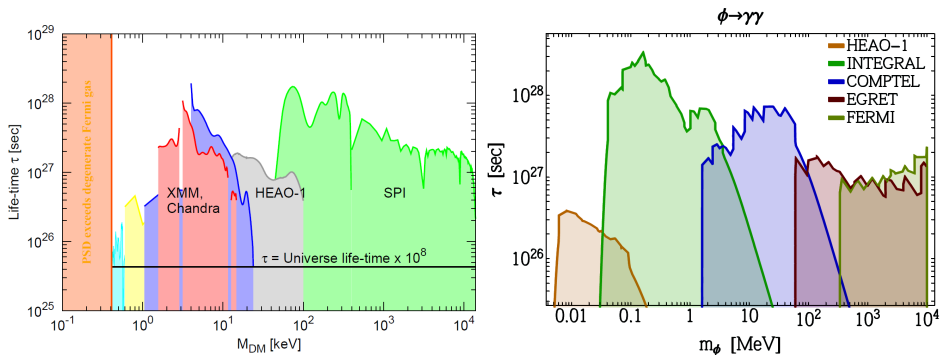
Figure 1.1: *Left:* Bounds on fermionic decaying Dark Matter lifetime from various missions (see text, figure taken from Boyarsky & Ruchayskiy, 2008). *Right:* Bounds on bosonic decaying Dark Matter lifetime from various diffuse X-ray and Gamma-ray observatories (see Essig et al. (2013), figure taken from same).

by the same physical process in each object.

The holistic approach relies on having available a large set of objects covering a wide range of environments, with individual exposures sufficiently deep that a more-or-less significant signal may be expected in each. The accumulation of archival data over the years has made it possible to cover an increasing area of parameter space (see Section 1.5.3), and allows for the effective application of this approach, as shall be seen throughout this Thesis.

1.5.3   Previous Searches

Many searches for the tell-tale X-ray emission from decaying Dark Matter have been performed in the past. All have utilized archival data from various X-ray observatories, most from *XMM-Newton*, since it provides in general the highest sensitivity per unit observing time, but also with *Chandra* (higher spatial resolution), *Suzaku*, *Swift* and INTEGRAL (higher energy range).

There have been three main categories of targets for these searches. Firstly, nearby galaxy clusters for their large Dark Matter masses (Boyarsky et al., 2006b; Riemer-Sørensen et al., 2007; Boyarsky et al., 2008c, 2010b). Secondly, the Milky Way (MW) halo since the expected signal is high due to its proximity (Riemer-Sørensen et al., 2006; Boyarsky et al., 2007b; Abazajian et al., 2007; Boyarsky et al., 2007a; Yuksel et al., 2008; Boyarsky et al., 2008b). And thirdly dwarf galaxy satellites of the MW because those exhibit the faintest astrophysical X-rays (Boyarsky et al., 2006c, 2007b; Loewenstein et al., 2009; Riemer-Sorensen & Hansen, 2009; Loewenstein & Kusenko, 2010; Boyarsky et al., 2010b; Mirabal & Nieto, 2010; Mirabal, 2010; Loewenstein & Kusenko, 2012; Kusenko et al., 2013). Observations of the M31 galaxy have also been performed (Watson et al., 2006, 2012; Boyarsky et al., 2010b, 2008a), that object holding the middle ground between clusters and dwarf galaxies in terms of (dis)advantages with regards to sensitivity to a Dark Matter decay signal. Choice of target objects was further mostly limited by the amount of available archival data. Additionally, the diffuse X-ray background
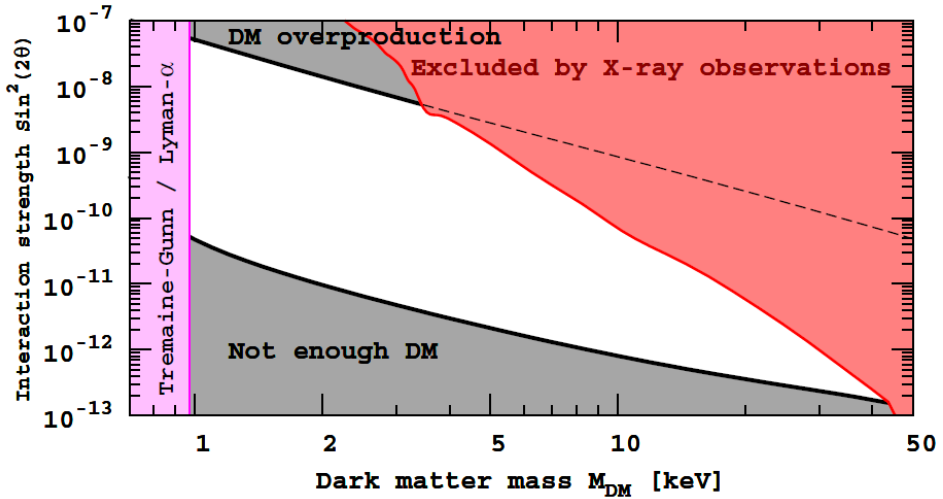
Figure 1.2: Parameters space of the sterile neutrino Dark Matter (see Section 1.3.4), in terms of the particle mass and its mixing angle (the strength of the mixing with the rest of the neutrino sector). The magenta band at low masses refers to the phase-space density constraints from dwarfs (see Section 1.2.1). The gray areas are sterile neutrino model-dependent restrictions from various production mechanisms, requiring that the correct amount of Dark Matter is produced in the early universe. The red area is excluded by non-detections from various previous studies as described in the text. Figure taken from Boyarsky et al. (2013)

as measured by HEAO-1 and *XMM-Newton* was also examined for Dark Matter decay signals (Boyarsky et al., 2006a), as were X-ray microcalorimeter measurements (better spectral resolution) of the MW halo (Boyarsky et al., 2007a). For an overview of these studies, see Table I of Neronov et al. (2014).

Up to February 2014, no convincing Dark Matter decay signals had been found, and the parameter space available was steadily being covered. The bounds on the model-independent particle lifetime obtained from these studies are shown in Figure 1.1, and specifically in terms of the sterile neutrino parameters mass and mixing angle in Figure 1.2.

1.6   Outline

The goal of the studies presented in this Thesis is to search for a signal from the decay of Dark Matter, as described in this Chapter earlier.

The majority of this thesis, namely Chapters 2 through 4, detail in roughly chronological order the discovery of such a Dark Matter decay candidate signal and the subsequent work performed to attempt to determine the origin of this signal.

Chapter 2 starts with a study that was first released in Febuary of 2014, detailing the discovery of an unidentified signal at 3.5 keV in X-ray spectra of both the Andromeda Galaxy and the Perseus Galaxy clusters (Boyarsky et al., 2014a). One week earlier, another work (Bulbul et al., 2014a) had been posted that reported an unidentified feature

at the same energy, but in a stack of galaxy clusters. We note that these works were performed independently. These two papers are often referred to as Bo14 and Bu14 respectively, or together as the discovery papers.

This Chapter further includes a study on the presence of a 3.5 keV feature in the Galactic Center (Boyarsky et al., 2015), as this serves as an important initial consistency check with regards to the origin of this feature. This work was posted within days of a comment regarding both of the discovery papers (Jeltema & Profumo, 2015), which also included a brief analysis of the GC. The response to this comment (Boyarsky et al., 2014b) shall be discussed in this Chapter as well.

Chapter 3 regards an observing campaign of the Draco dwarf galaxy, a Milky Way satellite. This campaign was undertaken with the specific goal of testing the Dark Matter decay origin of the 3.5 keV signal. The Chapter will start by arguing why this approach was taken and then reports on the the analysis of the obtained data and the results.

Chapter 4 is a re-examination of the Perseus Cluster using data from the *Suzaku* telescope. The main motivation for this were the various published studies on this dataset that were starkly inconsistent with each other. In addition, with the previous studies of Perseus in hand, this work allowed for the comprehensive study of the signal's consistency between telescopes and of the signal's spatial behavior in the object.

Chapter 5 contains a proof-of-concept study and report on the development of an original and non-traditional method to search for Dark Matter decay signals. Development had originally started prior to the discovery of the 3.5 keV line, and has been continued concomitant with that work. This enabled the development of this new method to focus on ways to avoid some of biggest disadvantages of the traditional methods employed in the 3.5 keV signal studies, although the statistical power of the dataset used for training and development purposes is not high enough to detect or constrain the origins of the 3.5 keV signal.

The **Appendix** contains comments on some of the other literature concerning the 3.5 keV signals. These concern an alternative atomic interpretation and a spatial study of the signal among others.

A note on terminology; although most of the work presented here, and indeed most of the literature work, put the best-fit energy of the potential Dark Matter decay signal somewhere between 3.51 keV and 3.57 keV, we will refer to this signal simply as the 3.5 keV signal or the 3.5 keV line or similar.

2 | DISCOVERY OF A DARK MATTER DECAY CANDIDATE SIGNAL AT 3.5 KEV

2.1 Introduction

This Chapter will first present the discovery of a potential Dark Matter decay signal at 3.5 keV in the X-ray spectra of the Andromeda Galaxy (M31) and the Perseus Galaxy Cluster. All archival data taken with the *XMM-Newton* telescope for these objects is analyzed over the 2.8–8 keV range. This range avoids the most complicated parts of the spectrum that are crowded with emission or instrumental features. The central parts of Perseus are also avoided, size the cluster core environment is more complicated to model. After modeling, positive line-like residuals at 3.5 keV (restframe) are present in both objects. The possibility that the origin of this signal is an anomalously bright or previously undetected elemental emission line is investigated, but found implausible. In both objects the radial distribution of the signal strength is studied. These are consistent with expectations of Dark Matter decay, although the statistical strength is low upon splitting the data in radial bins. The relative strength of the signal between M31 and Perseus is also found to be consistent under a Dark Matter origin, within the (rather large) error bars. Lastly, a long-exposure blank-sky dataset is investigated in order to exclude an instrumental origin of the signal.

Secondly, an important consistency check is reported in the form of an analysis of the spectrum of the Galactic Center (GC). In archival *XMM-Newton* data of the GC, a feature at 3.5 keV is also found. The details of the spectral modeling are discussed, with special attention for the possibility that the signal originates with emission from Potassium or Argon ions. This interpretation can not be excluded for the GC, but neither is it neccesary that all of the 3.5 keV flux in the GC needs to be of elemental origin. This is mainly due to the extremely complicated and multi-component nature of the GC. The central premise of this work is therefore not to attempt to prove that one particular interpretation is correct, but rather whether one interpretation is *incorrect*. Based on the Dark Matter content of the GC, and given the fluxes and Dark Matter content of the objects considered previously (M31 and Perseus), it is possible to estimate the 3.5 keV line flux that is needed in the GC in order for the Dark Matter decay interpretation to remain valid. The conclusions of this work is that indeed, the Dark Matter origin remains a consistent and valid explanation.

The works considered here have been commented on by Jeltema & Profumo (2015). The comments regard a few subjects; firstly, the commenters' own analysis of the data of M31 does not show a feature at 3.5 keV. Secondly, it is claimed that in the analysis of the Perseus Cluster, and also in the analysis by Bulbul et al. (2014a), which reports a 3.5 keV signal in a stack of galaxy clusters, the 3.5 keV signal can be explained by Potassium and Chlorine emission lines. The last Section of this Chapter contains the response to the criticisms raised, finding that they are mostly unsupported, a conclusion which was later also supported by Bulbul et al. (2014b) and a similar argument being reproduced in Appendix 6.2.

2.2 Detection in the Andromeda Galaxy and Perseus Galaxy Cluster

2.2.1 Data Analysis

We use the data obtained with MOS (Turner et al., 2001) and PN (Strüder et al., 2001) CCD cameras of *XMM-Newton* ("XMM" in what follows). We use SAS v.13.0.0[1] to reduce the raw data and filter the data for *soft solar protons* (Read & Ponman, 2003; Kuntz & Snowden, 2008) using the `espfilt` procedure. Because residual soft proton flares can produce weak line-like features in the spectra at positions where the effective area is non-monotonic (see e.g. Boyarsky et al., 2010b), we apply the procedure described in De Luca & Molendi (2004), based on the comparison of high-energy count rates for "in-FoV" (10-15 arcmin off-center) and out-FoV CCD regions[2]. We selected only observations where the ratio of $F_{in} - F_{out} < 1.15$.[3]

2.2.2 Analysis of M31

We use ~ 2 Msec of raw exposure observations of M31 within the central $1.5°$ (Tables 2.5 and 2.6). We select from the XMM archive 29 MOS observations offset less than $1.5'$ from the center of M31, and 20 MOS observations with offsets $23.7' - 55.8'$ that passed our criterion for residual contamination. Not enough PN observations passed this test to include them. The central and off-center observations were co-added seperately with the `addspec` routine from FTOOLS (Irby, B., 2008). The resulting spectra were binned by 60 eV. This bin size is a factor ~ 2 smaller than the spectral resolution of the XMM at these energies, which makes the bins roughly statistically independent.

We model the contribution of the instrumental (particle induced) background by a combination of an unfolded power law plus several narrow `gaussian` lines. The positions and normalizations of the lines were allowed to vary freely and the most prominent instrumental K-α lines (Cr, Mn, K, Fe, Ni, Ca, Cu) and Fe Kβ have been recovered. The width of the Gaussians was fixed at 1 eV (an infinitely thin line for the XMM spectral resolution). We verified that allowing the line widths to vary freely leaves the results unchanged. We restrict our modeling to the energy interval 2–8 keV. The Galactic foreground is negligible above 2 keV (Nevalainen et al., 2005). The combined emission of unresolved point sources at these energies is modeled by a `powerlaw` (Takahashi et al.,

---

[1]Xmm-newton science analysis system, http://xmm.esa. int/sas/

[2]Fin over fout public script, v. 1.1, `http://xmm.vilspa.esa.es/external/xmm_sw_cal/background/Fin_over_Fout`

[3]Ref. (De Luca & Molendi, 2004) argued that $F_{in} - F_{out} < 1.3$ is a sufficient criterion for flare removal. We find by visual inspection of the resulting spectra that a stricter criterion is needed to reduce artificial line-like residuals (Boyarsky et al., 2010b; Iakubovskyi, 2013). Lowering the threshold further is not feasible as the statistical errorbars on the value of $F_{in} - F_{out}$ are of the order of 5%.

Dataset	Exposure [ksec]	χ^2/d.o.f.	Line position [keV]	Flux [10^{-6} cts/sec/cm^2]	$\Delta\chi^2$	Significance
M31 on-center	978.9	97.8/74	3.53 ± 0.03	$4.9^{+1.6}_{-1.3}$	13.0	3.2σ
M31 off-center	1472.8	107.8/75	$3.50 - 3.56$	$< 1.8\ (2\sigma)$	...	
Perseus (MOS)	628.5	72.7/68	3.50 ± 0.04	$7.0^{+2.6}_{-2.6}$	9.1	2.6σ
Perseus (PN)	215.5	62.6/62	3.46 ± 0.04	$9.2^{+3.1}_{-3.1}$	8.0	2.4σ
Perseus (MOS)	1507.4	191.5/142	3.52 ± 0.02	$8.6^{+2.2}_{-2.3}$ (Perseus)	25.9	4.4σ
+ M31 on-center				$4.6^{+1.4}_{-1.4}$ (M31)	(3 dof)	
Blank-sky	15700.2	33.1/33	$3.45 - 3.58$	$< 0.7\ (2\sigma)$	...	

Table 2.1: Basic properties of combined observations used in this paper. Second column denotes the sum of exposures of individual observations. The improvement in $\Delta\chi^2$ when extra line is added to a model is quoted for each dataset. The last column shows the local significance of such an improvement when 2 extra d.o.f. (position and flux of the line) are added. The energies for Perseus are quoted in the rest frame. Taking into account trial factors, the global (over three datasets) significance is 4.4σ (see Section 2.2.5.1 for details).
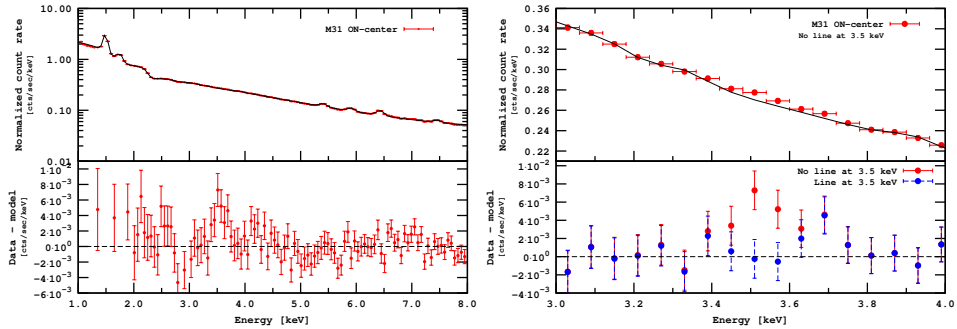
Figure 2.1: *Left:* Folded count rate (top) and residuals (bottom) for the MOS spectrum of the central region of M31. Statistical Y-errorbars on the top plot are smaller than the point size. The line around 3.5 keV is *not added*, hence the group of positive residuals. *Right:* zoom onto the line region.

2004). Several line-like residuals around 2.4 keV and 3.0 keV were identified as Ar and S line complexes and the corresponding thin (1 eV width) lines were added to the model. We verified that adding another `powerlaw` component to model the contribution of the extragalactic X-ray background (De Luca & Molendi, 2004; Nevalainen et al., 2005) does not improve the quality of fit and does not change the structure of the residuals.

The resulting spectrum of the central observations shows a group of positive residuals around 3.5 keV (Fig. 2.1). Adding a thin Gaussian line at that energy reduces the total χ^2 by ~ 13, see Table 2.1 (more than 3σ significance for extra 2 degrees of freedom). Examination of MOS1 and MOS2 observations individually finds the line in both cameras with comparable flux. For the off-center observations, none of the cameras show any detectable residual in the energy range $3.50 - 3.56$ keV. The 2σ upper bound on the flux is given in Table 2.1.

2.2.3 Perseus Cluster

If the candidate weak signal is of astrophysical (rather than instrumental) origin, we should be able to detect its redshift. To this end we have chosen the nearby Perseus cluster (Abell 426). At its redshift the line's centroid would be shifted by 63 eV. As the position of the line is determined with about 30 eV precision, one can expect to resolve the line's shift with about 2σ significance.

We took 16 off-center observations of the Perseus cluster (Table 2.3) and processed them in the same way as for M31. The flare removal procedure left 215 ksec of PN camera's exposure, therefore we also use PN data.

The resulting spectra were then added together and fitted to the combination of `vmekal` (with free abundances for Fe, Ni, Ar, Ca and S) plus (extragalactic) `powerlaw`. The instrumental background was modeled as in the M31 case.

The fit shows significant positive residuals at energies around 3.47 keV (in the detector frame). Adding a `zgauss` model with the redshift of the cluster improves the fit by $\Delta\chi^2 = 9.1$. The line's position is fully consistent with that of M31 (Table 2.1). If we fix the position of the line to that of M31 and allow the redshift to vary, $z = 0$ provides a worse fit by $\Delta\chi^2 = 3.6$ and its best-fit value is $(1.73 \pm 0.08) \times 10^{-2}$ – close to the value $z = 0.0179$ which we have used.

2.2.4 Interpretation

To further study the origin of the new line and possible systematic effects we combine XMM blank-sky observations from (Carter & Read, 2007; Henley & Shelton, 2012) with observations of the Lockman Hole (Brunner et al., 2008). The data were reduced similarly to the other datasets. Fig. 2.3 shows the combined spectrum. A dataset with such a large exposure requires special analysis (as described in (Iakubovskyi, 2013)). This analysis did not reveal any line-like residuals in the range $3.45 - 3.58$ keV with the 2σ upper bound on the flux being 7×10^{-7} cts/cm^2/sec. The closest detected line-like feature ($\Delta\chi^2 = 4.5$) is at $3.67^{+0.10}_{-0.05}$ keV, consistent with the instrumental Ca Kα line.[4]

Finally, we have performed a simultaneous fit of the on-center M31 and Perseus datasets (MOS), keeping a common position of the line (in the rest-frame) and allowing the line normalizations to be different. The line improves the fit by $\Delta\chi^2 = 25.9$ – 4.4σ significance (Table 2.1).

We identified a spectral feature at $E = 3.52 \pm 0.02$ keV in the combined dataset of M31 and Perseus with a statistical significance 4.4σ which does not coincide with any known line. Next we compare its properties with the expected behavior of a DM decay line.

The observed brightness of a decaying DM should be proportional to its column density $S_{DM} = \int \rho_{DM} d\ell$ – integral along the line of sight of the DM density distribution –

---

[4]Previously this line has only been observed in the PN camera (Strüder et al., 2001).
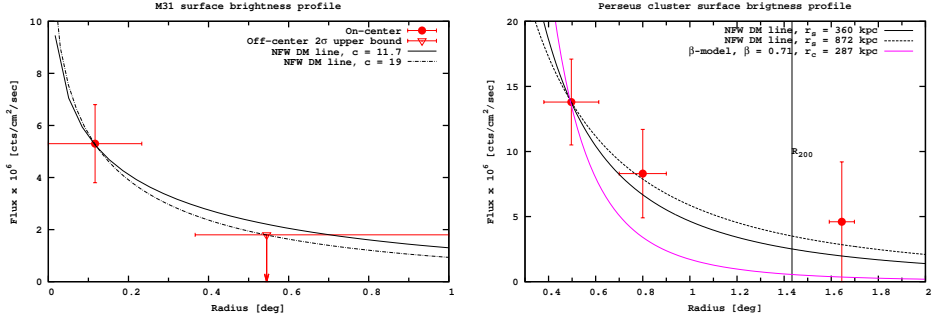
Figure 2.2: The line's brightness profile in M31 (left) and the Perseus cluster (right). A NFW DM distribution is assumed, the scale r_s is fixed to its best-fit values from Corbelli et al. (2010) (M31) or Simionescu et al. (2011) (Perseus) and the overall normalization is adjusted to pass through the left-most point.

and inversely proportional to the radiative decay lifetime τ_{DM}:

$$F_{DM} \approx 2.0 \times 10^{-6} \frac{\text{cts}}{\text{cm}^2 \cdot \text{sec}} \left(\frac{\Omega_{\text{fov}}}{500 \text{ arcmin}^2} \right) \times \qquad (2.1)$$
$$\left(\frac{S_{DM}}{500 \text{ M}_\odot/\text{pc}^2} \right) \frac{10^{29} \text{ s}}{\tau_{DM}} \left(\frac{\text{keV}}{m_{DM}} \right).$$

Using the line flux of the center of M31 and the upper limit from the off-center observations we constrain the spatial profile of the line. The DM distribution in M31 has been extensively studied (see an overview in Boyarsky et al. (2010b)). We take NFW profiles for M31 with concentrations $c = 11.7$ (solid line, Corbelli et al. (2010)) and $c = 19$ (dash-dotted line). For each concentration we adjust the normalization so it passes through first data point (Fig. 2.2). The $c = 19$ profile was chosen to intersect the upper limit, illustrating that the obtained line fluxes of M31 are fully consistent with the density profile of M31 (see e.g. Corbelli et al., 2010; Chemin et al., 2009; Sánchez-Conde et al., 2011, for a $c = 19 - 22$ model of M31).

For the Perseus cluster the observations can be grouped in 3 radial bins by their off-center angle. For each bin we fix the line position to its average value across Perseus (3.47 ± 0.07 keV). The obtained line fluxes together with 1σ errors are shown in Fig. 2.2. For comparison, we draw the expected line distribution from DM decay using the NFW profile of Simionescu et al. (2011) (best fit value $r_s = 360$ kpc ($c \approx 5$), black solid line; 1σ upper bound $r_s = 872$ kpc ($c \approx 2$), black dashed line). The isothermal β-profile from Urban et al. (2014) is shown in magenta. The surface brightness profile follows the expected DM decay line's distribution in Perseus.

2.2.5 Discussion

Finally, we compare the predictions for the DM lifetime from the two objects. The estimated column density within the central part of M31 ranges between $\bar{S} \sim 200 - 1000 \text{ M}_\odot/\text{pc}^2$ with the average value being around $600 \text{ M}_\odot/\text{pc}^2$ (Boyarsky et al., 2010b).

The column density of clusters follows from the $c-M$ relation (Boyarsky et al., 2010a; King & Mead, 2011; Mandelbaum et al., 2008). Considering the uncertainty on the profile and that our observations of Perseus go beyond r_s, the column density in the region of interest is within $\bar{S} \sim 100 - 600\,\mathrm{M_\odot/pc^2}$. Therefore the ratio of expected signals between Perseus and the center of M31 can be $0.1 - 3.0$, consistent with the ratio of measured fluxes $0.7 - 2.7$.

If DM is made of right-handed (sterile) neutrinos (Dodelson & Widrow, 1994), the lifetime is related to its interaction strength (*mixing angle*):

$$\tau_{DM} = \frac{1024\pi^4}{9\alpha G_F^2 \sin^2(2\theta) m_{DM}^5} = 7.2 \times 10^{29}\,\mathrm{sec} \left[\frac{10^{-8}}{\sin^2(2\theta)}\right] \left[\frac{1\,\mathrm{keV}}{m_{DM}}\right]^5.$$

Using the data from M31 and taking into account uncertainties in its DM content we obtain the mass $m_{DM} = 7.06 \pm 0.06$ keV and the mixing angle in the range $\sin^2(2\theta) = (2-20) \times 10^{-11}$ (taking the column density $\bar{S} = 600\,\mathrm{M_\odot/pc^2}$ and using only statistical uncertainties on flux we would get $\sin^2(2\theta) = 4.9^{+1.6}_{-1.3} \times 10^{-11}$). This value is fully consistent with previous bounds, Fig. 2.4. Moreover, it is intriguing that this value is consistent with the result of Bulbul et al. (2014a), which appeared when our paper was in preparation. Indeed, our value of $\sin^2(2\theta)$ is based on completely independent analysis of the signal from M31 and our estimates for its DM content, whereas the result of Bulbul et al. (2014a) is based on the signal from stacked galaxy clusters and on the weighted DM column density from the full sample.

These values of $\sin^2(2\theta)$ means that sterile neutrinos should be produced resonantly (Shi & Fuller, 1999; Shaposhnikov, 2008; Laine & Shaposhnikov, 2008), which requires the presence of significant lepton asymmetry in primordial plasma at temperatures few hundreds MeV. This produces restrictions on parameters of the νMSM (Boyarsky et al., 2009c).

The position and flux of the discussed weak line are inevitably subject to systematical uncertainties. There are two weak instrumental lines (K Kα at 3.31 keV and Ca Kα at 3.69 keV), although formally their centroids are separated by more than 4σ. Additionally, the region below 3 keV is difficult to model precisely, especially at large exposures, due to the presence of the absorption edge and galactic emission. However, although the residuals below 3 keV are similar between the M31 dataset (Fig. 2.1) and the blank sky dataset (Fig. 2.3), the line is *not detected* in the latter.

If the feature were due to an unmodelled wiggle in the effective area, its flux would be proportional to the continuum brightness and the blank-sky dataset would have exhibited a 4 times smaller feature with roughly the same significance (see Section 2.2.5.2). In addition, the Perseus line would not be properly redshifted.

The properties of this line are consistent (within uncertainties) with the DM interpretation. To reach a conclusion about its nature, one will need to find more objects that give a detection or where non-observation of the line will put tight constraints on its properties. The forthcoming *Astro-H* mission (Takahashi et al., 2012) has sufficient spectral resolution to spectrally resolve the line against other nearby features and to detect the candidate line in the "strong line" regime (Boyarsky et al., 2007a). In particular, *Astro-H* should be able to resolve the Milky Way halo's DM decay signal and therefore all its observations can be used. Failure to detect such a line will rule out the DM origin of the Andromeda/Perseus signal presented here.
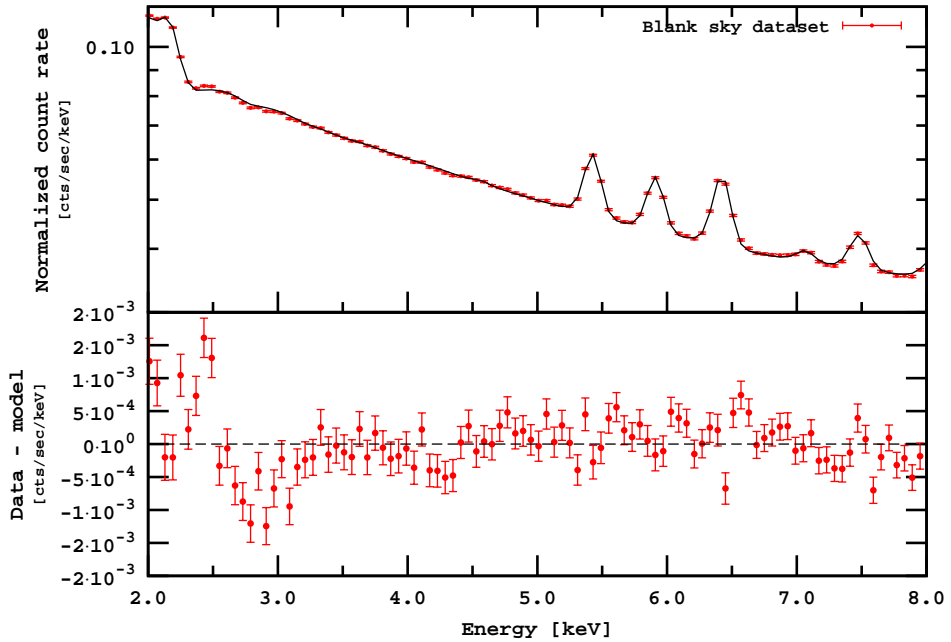
Figure 2.3: Combination of 382 MOS blank sky observations.

2.2.5.1 Global significance estimate

Significances quoted in the main body of the paper (Table 2.2) reflect the local significance of the signal. Since the position of the line is unknown *a priori* we need to take into account the probability of falsely detecting a statistical fluctuation of equal or higher significance at any position in the entire fitting range (2.0–8.0 keV). In addition, having found a signal in the same energy bin in three separate datasets, we compute this global significance taking into account the probability of such signals showing in the same resolution element by chance. Given the local significance of the signal in each dataset (based on the $\Delta\chi^2$ values and the number of degrees of freedom), and the number of independent resolution elements, we can determine the global significance of the combination of all signals. The number of independent resolution elements, N_E, for our datasets is about 40 (6 keV energy range divided by 150 eV — average energy resolution of the *XMM-Newton*).

The global significance per dataset is computed from the two-sided p-value p_i (directly related to the number of σ of the signal) by multiplying by N_E (see Table 2.2). We took a "two-sided" p-value to take into account both positive and negative residuals.

The combined global significance then is

$$\frac{\prod_i p_i N_E}{N_E^{N_d-1}} = 1.1 \cdot 10^{-5} \tag{2.2}$$

where $N_d = 3$ is the number of datasets. This corresponds to a false detection probability
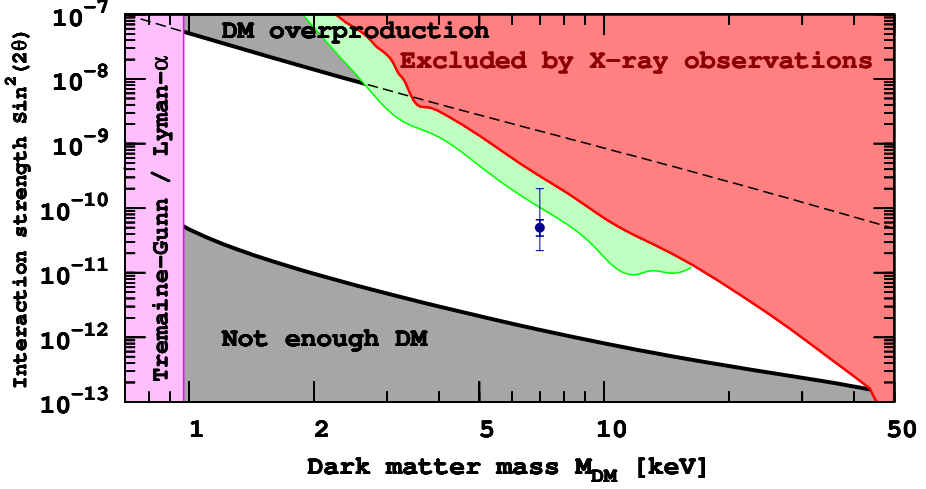
Figure 2.4: Constraints on sterile neutrino DM within νMSM (Boyarsky et al., 2012). Recent bounds from Watson et al. (2012); Horiuchi et al. (2014) are shown in green. Similar to older bounds (marked by red) they are smoothed and divided by factor 2 to account for possible DM uncertainties in M31. In every point in the white region sterile neutrino constitute 100% of DM and their properties agree with the existing bounds. Within the gray regions too much (or not enough) DM would be produced in a minimal model like νMSM. At masses below ~ 1 keV dwarf galaxies would not form (Boyarsky et al., 2009a; Gorbunov et al., 2008). The blue point would corresponds to the best-fit value from M31 if the line comes from DM decay. Thick errorbars are $\pm 1\sigma$ limits on the flux. Thin errorbars correspond to the uncertainty in the DM distribution in the center of M31.

Dataset	$\Delta\chi^2$	d.o.f.	local significance	local p-value	false detection probability	global significance
M31-oncen (MOS)	13	2	3.18σ	$1.5 \cdot 10^{-3}$	0.06	1.89σ
Perseus (MOS)	9.1	2	2.56σ	$1.05 \cdot 10^{-2}$	0.42	0.81σ
Perseus (PN)	8	2	2.36σ	$1.83 \cdot 10^{-2}$	0.73	0.35σ
All combined					$1.1 \cdot 10^{-5}$	4.4σ

Table 2.2: Table of significances per dataset. Quoted p-values refer to the two-sided case (one-sided p-values are half of the two-sided ones). The false detection probability refers to the probability of falsely detecting a signal in that dataset like the one under consideration or stronger at any energy in the range considered. The global significance was converted from the false detection probability per dataset. The combined false detection probability and global significance of these three datasets is also given (computed from the individual detections, not from a single combined dataset).

for the combination dataset of **0.0011%**. Converted to the significance this p-value gives 4.4σ **global significance**.

Alternatively, we could have taken into account only probability of positive fluctuations (so "two-sided" p-values in the Table 2.2 should be divided by 2). Using the same formula (2.2) we would obtain 4.7σ global significance.

Introducing systematic uncertainties into all our datasets at the level of $\sim 1\%$, the local significances drop by about 1σ each.

	ObsID	Off-axis angle arcmin	Cleaned exposure MOS1/MOS2 [ksec]	FoV [arcmin^2] MOS1/MOS2	F_{in}-F_{out}
1	0305690301	22.80	18.6 / 18.6	473.6 / 574.3	1.266 / 1.340
2	0085590201	25.01	40.1 / 40.5	564.6 / 572.1	1.290 / 1.336
3	0204720101	27.87	14.1 / 14.5	567.7 / 574.5	2.373 / 2.219
4	0673020401	29.48	15.6 / 17.6	479.6 / 574.0	1.318 / 1.331
5	0405410201	29.52	16.1 / 16.6	480.8 / 573.9	1.354 / 1.366
6	0305690101	29.54	25.1 / 25.4	476.0 / 573.5	1.231 / 1.247
7	0405410101	31.17	15.8 / 16.8	481.8 / 572.9	1.235 / 1.195
8	0305720101	31.23	11.5 / 11.8	476.8 / 573.9	1.288 / 1.296
9	0673020301	36.54	13.9 / 15.4	485.4 / 573.8	1.211 / 1.304
10	0305690401	36.75	25.9 / 26.0	479.1 / 573.8	1.158 / 1.156
11	0305720301	41.92	16.7 / 17.5	464.7 / 573.6	1.433 / 1.447
12	0151560101	47.42	23.7 / 23.6	572.1 / 573.6	1.294 / 1.206
13	0673020201	53.31	22.8 / 23.4	479.5 / 573.9	1.262 / 1.228
14	0204720201	54.11	22.4 / 22.9	564.0 / 573.2	1.153 / 1.195
15	0554500801	95.45	15.0 / 15.3	480.8 / 572.7	1.098 / 1.113
16	0306680301	101.88	12.3 / 13.0	468.1 / 574.0	1.177 / 1.089

Table 2.3: Parameters of the *XMM-Newton* spectra of the Perseus cluster used in our analysis. The observations are sorted by the off-axis angle from the center of the Perseus cluster. Two central observations (ObsIDs 0305780101 and 0085110101) were not included in the analysis to avoid modeling of the emission from the core of the Perseus cluster. Notice that only these two central observations were used in Boyarsky et al. (2008a), therefore that dataset and our dataset are independent from each other. The difference in FoVs between MOS1 and MOS2 cameras is due to the loss CCD6 in MOS1 camera. The parameter F_{in}-F_{out} (last column) estimates the presence of residual soft protons according to the procedure of http://xmm.vilspa.esa.es/external/ xmm_sw_cal/background/Fin_over_Fout. Note, however, that for the bright extended sources, such an estimate is not appropriate, see http://xmm2.esac.esa.int/external/xmm_sw_ cal/background/epic_scripts.shtml for details). Horizontal lines shows how we group observations for building the surface brightness profile of the line (as shown in Fig. 2, right panel).

Range of offsets	Exposure [ksec]	Flux [cts/sec/cm^2]
$23 - 37'$	400	13.8 ± 3.3
$42' - 54'$	230	8.3 ± 3.4
$96' - 102'$	56	4.6 ± 4.6

Table 2.4: Definitions of the radial bins used for the data analysis of the Perseus cluster.
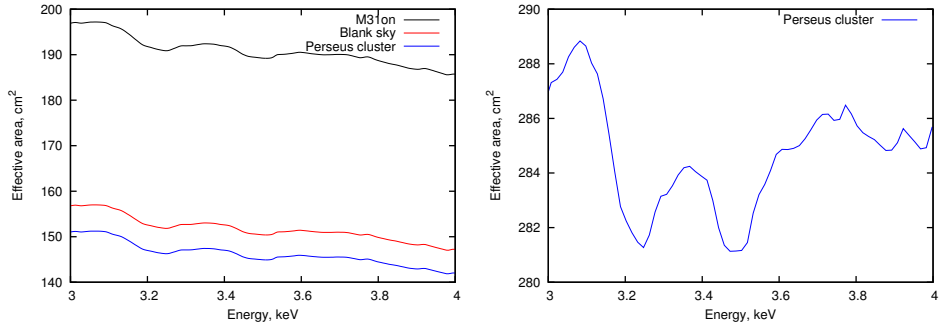
Figure 2.5: Exposure averaged effective area of the XMM MOS camera for the combination of observations of Perseus galaxy cluster, M31 and blank-sky (*left panel*). For Perseus galaxy cluster we also show the exposure averaged PN camera's effective area (*right panel*).
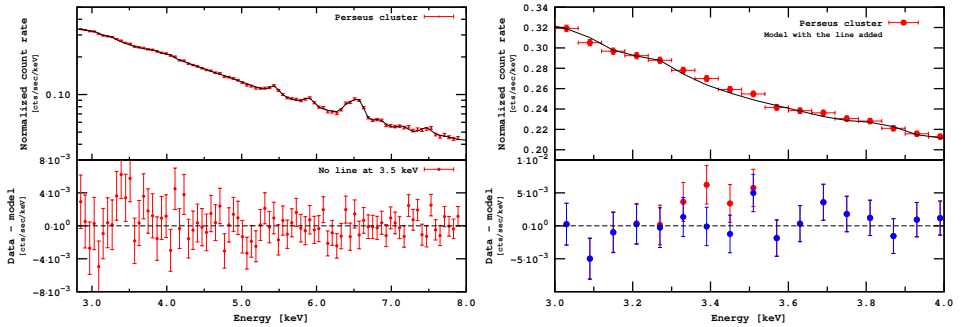
Figure 2.6: *Left:* Folded count rate (top) and residuals (bottom) for the combined spectrum of 16 observations of MOS cameras (listed in the Tabel 2.3) of the Perseus cluster. Statistical Y-errorbars on the top plot are smaller than the point size. The line around 3.5 keV is *not added*, hence the group of positive residuals. *Right*: zoom onto the line region. The spectrum is shown in the detector restframe, therefore the line is shifted left according to the Perseus redshift.

2.2.5.2 Effective area

In this Appendix we show the effective area of the Perseus, M31 and blank-sky datasets (Fig. 2.5). One sees that all three datasets exhibit a (known) wiggle at energy $E \sim 3.5$ keV in the detector frame (about 1.5% deviation from the monotonic behaviour). This kind of behavior of the effective area is due to K-, L- and M-shell transitions of Al, Sn and Au. The SAS software uses calibration files based on ray-tracing calculations through numerical models of the telescope assemblies (Gondoin et al., 2000; Turner et al., 2001; Strüder et al., 2001). The effective area curves differ between datasets mostly due to the vignetting effect, which depends on energy and on the weighting during the data stacking.

Looking at the left panel of Fig. 2.5 one sees that the effective area of all MOS observations is self-similar. The variation in shape between three datasets in the energy range 3.4-3.6 keV is less than 0.1% and less than 0.4% in the 3-4 keV range. If the line is due to an unmodeled wiggle, this would mean that a 10 times larger unmodeled feature (line

is 3-4% of the continuum level) is present in the datasets of M31 and Perseus, but *not* in the blank sky. As all datasets are combinations of observations taken over long period of lifetime of the XMM, the existence of such a feature is difficult to imagine.

Notice that if this wiggle would be the cause of the signal, reported in this paper, it would fail to explain why the redshift of the line in the Perseus cluster is correctly detected (at energies $3.5/1 + z = 3.4$ keV the effective area has a local maximum, rather than minimum). It would also fail to explain the detection of the line in the combined dataset of 70 clusters at different redshifts, presented in Bulbul et al. (2014a).

Additionally, if the feature is due to an *unmodelled* wiggle in the effective area, its flux in each dataset should be proportional to the continuum brightness. Comparing the M31 and blank-sky datasets we see that the count rate at energies of interest is 4 times larger for M31, so that the blank-sky dataset would have exhibited a 4 times smaller (instrumental) feature with a flux $\sim 1.2 \times 10^{-6}$ cts/sec/cm^2, were it due to a wiggle in the effective area. Notice that the exposure for the blank sky is 16 times larger and such a line would have been resolved with sufficient statistical significance. The upper (non-detection) limit from the blank-sky dataset is ~ 2 lower (0.7×10^{-6} cts/sec/cm^2).

2.2.5.3 Flare removal

In this Section we investigate how sensitive the derived bounds are to the imposed $F_{in} - F_{out}$ cut. To this end we have imposed a number of different cuts in $F_{in} - F_{out}$ and rederived the 2σ upper bound in the blank sky dataset. We see (Fig. 2.7) that the bound derived in the paper does not really change until we start to impose very stringent cuts $F_{in} - F_{out} < 1.06$, which starts to drastically reduce the statistics (clean exposure) as the blue squares in Fig. 2.7 demonstrate).

	ObsID	Off-axis angle arcmin	Cleaned exposure MOS1/MOS2 [ksec]	FoV [arcmin^2] MOS1/MOS2	F_{in}-F_{out}
17	0405320501	0.02	12.3/13.6	480.6/573.2	1.132/1.039
18	0405320701	0.02	14.8/14.9	480.7/572.8	1.046/1.057
19	0405320801	0.02	13.1/13.1	488.2/573.0	1.160/1.117
20	0405320901	0.02	15.5/15.6	488.0/574.3	1.099/1.065
21	0505720201	0.02	25.2/26.2	485.6/572.1	1.079/1.057
22	0505720301	0.02	25.4/24.3	486.0/573.9	1.129/1.105
23	0505720401	0.02	19.9/20.2	488.6/573.1	1.113/1.108
24	0505720501	0.02	12.9/13.9	480.3/574.1	1.151/1.064
25	0505720601	0.02	20.2/20.4	488.3/571.4	1.085/1.108
26	0551690201	0.02	20.5/20.3	486.5/574.2	1.099/1.072
27	0551690301	0.02	19.7/19.4	479.3/573.0	1.109/1.117
28	0551690501	0.02	16.9/18.4	486.3/573.2	1.095/1.109
29	0600660201	0.02	17.4/17.5	487.0/572.9	1.080/1.041
30	0600660301	0.02	16.1/16.1	488.6/572.0	1.054/1.041
31	0600660401	0.02	15.0/15.5	479.9/573.1	1.078/1.072
32	0600660501	0.02	13.5/14.3	488.2/573.4	1.079/1.083
33	0600660601	0.02	15.2/15.1	481.8/573.6	1.073/1.041
34	0650560201	0.02	21.0/21.3	488.1/573.3	1.198/1.140
35	0650560301	0.02	26.9/29.0	487.9/572.6	1.082/1.095
36	0650560401	0.02	12.4/13.5	488.0/573.1	1.157/1.069
37	0650560501	0.02	15.8/21.6	487.8/573.4	1.162/1.114
38	0650560601	0.02	20.8/21.5	487.5/572.2	1.085/1.068
39	0674210201	0.02	19.6/19.6	478.6/573.3	1.094/1.083
40	0674210301	0.02	14.9/15.0	488.1/573.6	1.052/1.043
41	0674210401	0.02	17.9/18.1	485.7/572.7	1.071/1.081
42	0674210501	0.02	16.2/16.3	488.8/573.5	1.192/1.139
43	0202230201	1.44	18.3/18.4	567.1/572.8	1.089/1.108
44	0202230401	1.44	17.0/17.1	566.5/573.6	1.118/1.109
45	0202230501	1.44	9.2/9.4	568.1/574.1	1.048/1.129

Table 2.5: Parameters of the *XMM-Newton* spectra of M31 used in our on-center analysis. The significant difference in FoVs between MOS1 and MOS2 cameras is due to the loss CCD6 in MOS1 camera. Off-center observations are found in Table 2.6.

	ObsID	Off-axis angle arcmin	Cleaned exposure MOS1/MOS2 [ksec]	FoV [arcmin^2] MOS1/MOS2	F_{in}-F_{out}
46	0402560201	23.71	16.0/16.6	478.7/574.0	1.096/1.095
47	0505760201	23.71	35.2/38.6	476.6/571.6	1.065/1.058
48	0511380201	23.71	15.3/15.4	485.0/572.7	1.126/1.047
49	0511380601	23.71	14.8/17.2	485.4/573.1	1.041/1.074
50	0402560901	24.18	42.4/42.9	475.0/572.8	1.118/1.071
51	0672130101	24.24	73.0/78.6	473.1/572.8	1.088/1.064
52	0672130501	24.24	22.7/25.4	477.0/574.8	1.097/1.110
53	0672130601	24.24	67.8/67.3	471.8/571.4	1.115/1.101
54	0672130701	24.24	70.7/74.3	484.8/573.5	1.076/1.052
55	0410582001	26.29	13.2/13.9	485.4/575.0	1.073/1.030
56	0402561001	28.81	48.0/49.4	478.4/572.5	1.084/1.042
57	0402560301	30.34	43.9/45.7	474.6/573.1	1.037/1.027
58	0505760301	39.55	41.0/41.3	485.0/570.8	1.022/1.022
59	0402561101	39.56	44.8/44.8	478.7/571.4	1.121/1.067
60	0404060201	42.94	19.1/19.1	480.7/573.7	0.993/1.045
61	0402561201	47.37	38.1/39.2	478.5/573.3	1.077/1.034
62	0402560501	49.06	48.8/50.6	487.2/572.9	1.102/1.079
63	0511380301	49.06	31.5/31.0	482.0/572.3	1.105/1.082
64	0151580401	50.89	12.3/12.3	567.2/574.1	1.131/1.020
65	0109270301	55.81	25.5/25.0	562.6/571.6	1.110/1.106

Table 2.6: Parameters of the *XMM-Newton* spectra of M31 used in our off-center analysis. The significant difference in FoVs between MOS1 and MOS2 cameras is due to the loss CCD6 in MOS1 camera. On-center observations are found in Table 2.5, and .
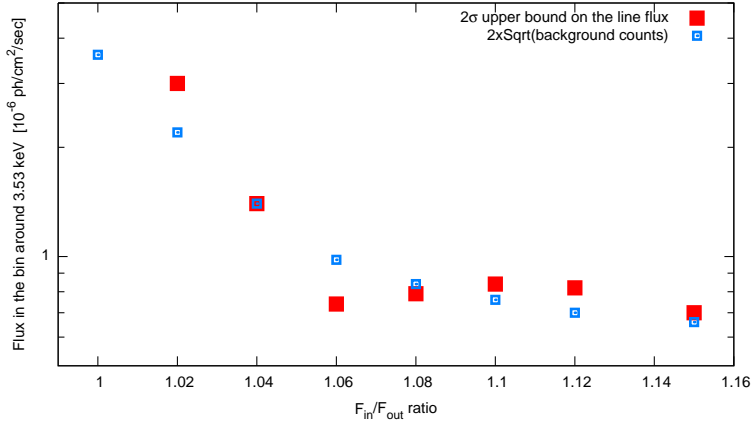
Figure 2.7: The dependence of the 2σ upper bound on the flux in the blanksky dataset on the imposed $F_{in} - F_{out}$ criterion. The statistical error on this parameter is about 5%. The bound on the flux remains at the quoted level until we start to lose significant fraction of observations for $F_{in} - F_{out} < 1.06$. Blue squares are defined as $2 \times \sqrt{N_{bg}}$ where N_{bg} is the number of background counts in the energy bin, equal to spectral resolution. The difference between blue and red squares appears because spectral modeling trakes into account also the line shape.
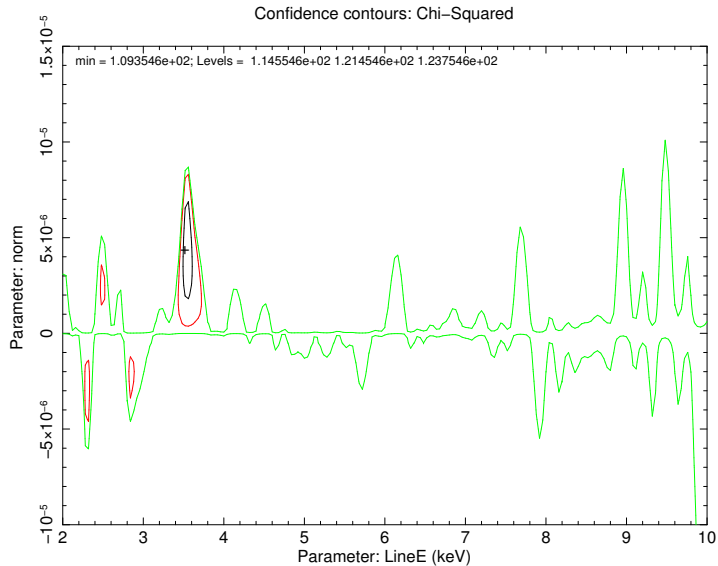
Figure 2.8: Structure of the residuals (both positive and negative) around the best fit model for M31 central observation. Red contours show residuals that are above 1σ. Black contour shows more than 3σ residual (3.53 keV line). The other residuals are below 1σ.

2.3   Detection in the Galactic Center

BASED ON
Checking the dark matter origin of 3.53 keV line with the Milky Way center
Alexey Boyarsky, Jeroen Franse, Dmytro Iakubovskyi, Oleg Ruchayskiy
Published in *Physical Review Letters*

2.3.1   Data and Analysis

We use all archival data of the Galactic Center obtained by the EPIC MOS cameras (Turner et al., 2001) with Sgr A* less than $0.5'$ from the telescope axis (see Table 2.7). The data are reduced by the standard SAS[5] pipeline, including screening for the time-variable soft proton flares by espfilt. We removed the observations taken during the period MJD 54000–54500 due to strong flaring activity of Sgr A* (see Fig. 2.11). The data reduction and preparation of the final spectra are similar to Section 2.2. For each reduced observation we select a circle of radius $14'$ around Sgr A* and combine these spectra using the FTOOLS (Irby, B., 2008) procedure addspec.

To account for the cosmic-ray induced instrumental background we have subtracted the latest closed filter datasets (Nevalainen et al. (2005)exposure: 1.30 Msec for MOS1 and 1.34 Msec for MOS2). The rescaling of the closed filter data has been performed such that the flux at energies $E > 10$ keV reduces to zero (see (Nevalainen et al., 2005) for details). We model the resulting physical spectrum in the energy range 2.8–6.0 keV. The X-ray emission from the inner part of the Galactic Center contains both thermal and non-thermal components (Kaneda et al., 1997; Muno et al., 2004). Therefore, we chose to model the spectrum with a thermal plasma model (vapec) and a non-thermal powerlaw component modified by the phabs model to account for the Galactic absorption.[6] We set the abundances of all elements – except for Fe – to zero but model the known astrophysical lines with gaussians (Bulbul et al., 2014a; Boyarsky et al., 2014a; Riemer-Sorensen, 2014). We selected the $\geq 2\sigma$ lines from the set of astrophysical lines of (Uchiyama et al., 2013; Bulbul et al., 2014a)[7]. The intensities of the lines are allowed to vary, as are the central energies to account for uncertainties in detector gain and limited spectral resolution. We keep the same position of the lines between the two cameras.

The spectrum is binned to 45 eV to have about 4 bins per resolution element. The fit quality for the dataset is $\chi^2 = 108/100$ d.o.f. The resulting values for the main continuum components – the folded powerlaw index (for the integrated point source contribution), the temperature of the vapec model (~ 8 keV), and the absorption column density – agree well with previous studies (Kaneda et al., 1997; Muno et al., 2004).

2.3.2   Results

The resulting spectra of the inner $14'$ of the Galactic Center show a $\sim 5.7\sigma$ line-like excess at 3.539 ± 0.011 keV with a flux of $(29 \pm 5) \times 10^{-6}$ cts/sec/cm^2 (see Fig. 2.9). It

---

[5]v.13.5.0 http://xmm.esa.int/sas

[6]The Xspec (Arnaud, 1996) v.12.8.0 is used for the spectral analysis.

[7]Unlike Bulbul et al. (2014a) we do not include K XVIII lines at 3.47 and 3.51 keV to our model. See the discussion below
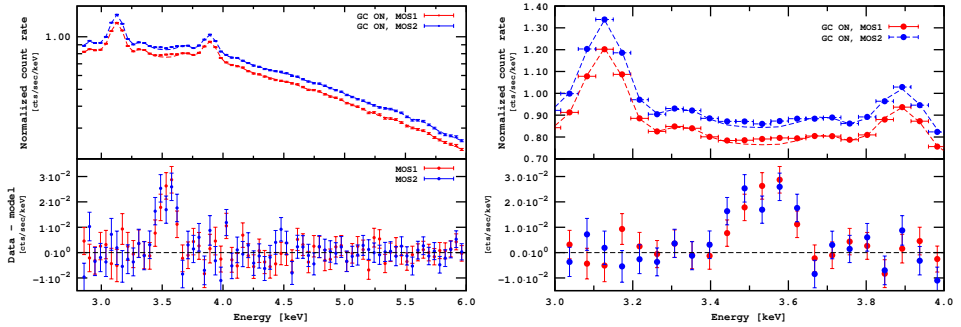
Figure 2.9: *Left:* Folded count rate for MOS1 (lower curve, red) and MOS2 (upper curve, blue) and residuals (bottom) when the line at 3.54 keV is *not added*. The difference between the cameras is due to detector gaps and bad pixels. *Right*: Zoom at the range 3.0–4.0 keV.

should be stressed that these 1σ error-bars are obtained with the xspec command error (see the discussion below). The position of the excess is very close to the similar excesses recently observed in Andromeda (3.53 ± 0.03 keV) and Perseus (3.50 ± 0.04 keV) reported in Boyarsky et al. (2014a), and is less than 2σ away from the one described in Bulbul et al. (2014a).

We also performed combined fits of the GC dataset with those of M31 and Perseus from Boyarsky et al. (2014a). As mentioned, the data reduction and modeling were performed very similarly, so we suffice with repeating that the inner part of M31 is covered by almost 1 Msec of cleaned MOS exposure, whereas a little over 500 ksec of clean MOS exposure was available for Perseus (see Section 2.2 for details).

We first perform a joint fit to the Galactic Center and M31, and subsequently to the Galactic Center, M31 and Perseus. In both cases, we start with the best-fit models of each individual analysis without any lines at 3.53 keV, and then add an additional gaussian to each model, allowing the energy to vary while keeping the same position between the models. The normalizations of this line for each dataset are allowed to vary independently. In this way, the addition of the line to the combination of Galactic Center, M31 and Perseus gives 4 extra degrees of freedom, which brings the joint significance to $\sim 6.7\sigma$.

To further investigate possible systematic errors on the line parameters we took into account that the gaussian component at 3.685 keV may describe not a single line, but a complex of lines (Table 2.8). Using the steppar command we scanned over the two-dimensional grid of this gaussian's intrinsic width and the normalization of the line at 3.539 keV. We were able to find a new best fit with the 3.685 keV gaussian width being as large as 66 ± 15 eV. In this new minimum our line shifts to 3.50 ± 0.02 keV (as some of the photons were attributed to the 3.685 keV gaussian) and has a flux of 24×10^{-6} cts/sec/cm^2 with a 1σ confidence interval of $(13 - 36) \times 10^{-6}$ cts/sec/cm^2. The significance of the line is $\Delta\chi^2 = 9.5$ (2.6σ for 2 d.o.f.). Although the width in the new minimum seems to be too large even for the whole complex of Ar XVII lines (see 2.3.3), we treat this change of line parameters as the estimate of systematic uncertainties. To reduce these systematics one has either to resolve or to reliably model a line complex around 3.685 keV instead of representing it as one wide gaussian component.
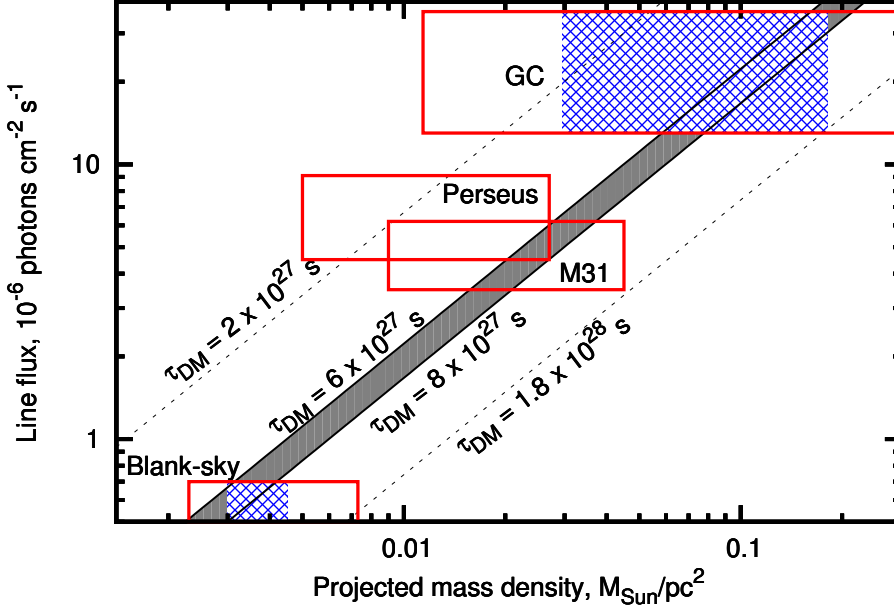
Figure 2.10: The flux of the 3.53 keV line in the spectra of the GC (this work), the Perseus cluster outskirts, M31 and the upper bound from blank sky (from Boyarsky et al. (2014a)) as a function of the mass within the XMM's field-of-view divided by the distance squared. Diagonal lines show the expected behaviour of a decaying DM signal for a given DM particle lifetime. The vertical sizes of the boxes are $\pm 1\sigma$ statistical error on the line's flux – or the 2σ upper bound for the blank-sky dataset. The horizontal sizes of the boxes represent systematic errors in the mass modeling by bracketing the literature values (see text). The Milky Way halo contribution to M31 is included (but not for Perseus, because the line is redshifted by $\sim$60 eV). As mentioned in the text, the distributions of the different objects are related to a greater or lesser extent, and the GC and blank-sky measurements in particular; the blue shaded regions give an example of this by showing one particular literature model of the Milky Way by Smith et al. (2007), its horizontal size indicating uncertainties in galactic disk modeling. This figure indicates that $\tau_{DM} \sim 6 - 8 \times 10^{27}$ sec is consistent with all datasets.

As was argued in Boyarsky et al. (2014a), an interpretation of the signal as an un-modelled wiggle in the effective area is not favoured because it should have produced a very significant signal in the blank-sky dataset as well. This is because an effect like this would produce a line-like residual proportional to the continuum level. In addition, the line would not be redshifted properly for Perseus (Boyarsky et al., 2014a) and the cluster stack from Bulbul et al. (2014a).

2.3.3 Discussion

In order to place this signal in context with respect to the DM interpretation of Bulbul et al. (2014a) and Boyarsky et al. (2014a), we need to compare the DM content of all relevant objects. A more detailed discussion of the following can be found in Section 2.3.4. We obtained literature DM distributions for Perseus, M31 and the MW. The latter applies

both to our GC results and the blank-sky upper limits. We are interested in the potential DM decay-product flux in each of our observations, and therefore require the detailed DM distributions rather than total mass. Any DM decay signal is expected to scale as the DM mass in the field-of-view divided by the distance squared to the DM, which we refer to as projected DM density. This quantity has a large uncertainty when we determine it from the literature distributions. The spread between the distributions is larger than the statistical errors quoted on the distribution parameters. For the GC, the case is even more complicated because there are no measurements of the DM distribution available within the inner 3 kpc, and they rely on extrapolating the distributions to small radii.

The situation is summarized in Fig. 2.10. It depicts all the measurements as a function of projected DM density against the expectations of a decaying DM scenario. This shows that a decaying DM with a lifetime of $\tau_{DM} \sim 6 - 8 \times 10^{27}$ sec would explain the signals from the GC, Perseus and M31, and the non-detection in the blank-sky dataset, given the uncertainties on the mass modeling. It should be noted that a correlation between the GC and blank-sky projected DM densities is necessarily present, since these are just different parts of the same halo; the blank-sky upper limit and the GC measurement require a cuspy DM profile. In addition, M31 and the Milky Way are expected to have (self)similar distributions, providing another consistency check. Boyarsky et al. (2014a) showed that in order to explain the signal from central $14'$ and non-observation from M31 outskirts, the Andromeda DM density profile should be cuspy, as predicted also for the Milky Way. This matter is also investigated using simulations in Lovell et al. (2015) and reports consistency of all measurements between objects as well. Lastly, in cluster outskirts the hydrostatic mass may be under-estimated (see e.g., Okabe et al., 2014), which would only improve the consistency between the data sets.

The non-detection of the signal in stacked dSphs by Malyshev et al. (2014) rules out the central values of the decay lifetime from Bulbul et al. (2014a) but is consistent with Boyarsky et al. (2014a) in case of large project DM mass (also preferred from comparison with other signals, Fig. 2.10). The signal was not detected in stacked galaxy spectra Anderson et al. (2015). However, the novel method of Anderson et al. (2015) has pronounced systematic effects (see their Appendix B) and is the least sensitive exactly at energies $E \sim 3.5$ keV. Iakubovskyi (2014) used a stacked dataset of nearby galaxies from Iakubovskyi (2013) and showed that systematic effects and uncertainty in dark matter distributions Boyarsky et al. (2010a) lead to the bound $\tau_{DM} \gtrsim 3.5 \times 10^{27}$ sec, consistent with our findings. Other bounds on decaying dark matter in the ~ 3.5 keV energy range (see Iakubovskyi (2013); Horiuchi et al. (2014); Sekiya et al. (2015) and references therein) are also consistent with our detections for lifetimes that we discuss in this work.

As mentioned in the Section 2.3.2, there is a degeneracy between the width of the Ar XVII complex around 3.685 keV and the normalization of the line in question. If we allow the width of the Ar XVII line to vary freely we can decrease the significance of the line at 3.539 keV to about 2σ. However, in this case the width of the `gaussian` at 3.685 keV should be $95 - 130$ eV, which is significantly larger than we obtain when simulating a complex of four Ar XVII lines wit the `fakeit` command. In addition, in this case the total flux of the line at 3.685 keV becomes *higher* than the fluxes in the lines at 3.130 and 3.895 in contradiction with the atomic data (Table 2.8).

Another way to decrease the significance of the line at 3.539 is to assume the presence

of a potassium ion (K XVIII) with a line at 3.515 keV and a smaller line at 3.47 keV. If one considers the abundance of potassium as a completely free parameter (as was done in Riemer-Sorensen (2014) for the Chandra data of the Galactic Center), one can find an acceptable fit of the XMM GC data without an additional line at 3.539 keV, for potassium abundances as low as $\sim$1 solar. As described in Section 2.3.5, due to the complicated internal temperature and abundance structures it is not possible to reliably constrain the overall potassium abundance of the GC to a degree that rules out the K XVIII origin of the 3.539 keV line *in this dataset*.

However, if we are to explain the presence of this line in the spectra by the presence of K XVIII, we have to build a model that consistently explains the fluxes in this line in different astronomical environments: in galaxy clusters (in particular Perseus) at all off-center distances from the central regions (Bulbul et al., 2014a) to the cluster outskirts up to the virial radius (Boyarsky et al., 2014a); in the central part of M31; and in the Galactic Center. In addition, we need to explain that this line is not observed – and therefore that this transition *should not* be excited – in the outskirts of the Milky Way and of M31 (Boyarsky et al., 2014a). Such a consistent model does not look convincing. In particular, in the case of M31 there are no strong astrophysical lines between 3 and 4 keV. The powerlaw continuum is well determined by fitting the data over a wider range of energies (from 2 to 8 keV) and allows a clear detection of the line at 3.53 ± 0.03 keV with $\Delta\chi^2 = 13$ (Boyarsky et al., 2014a), which is also the largest line-like feature in the entire 3–4 keV range. Were this signal in M31 due to K XVIII, there should be plenty of stronger emission lines present. In addition, the authors of Bulbul et al. (2014a) conclude that strongly super-solar abundances of K XVIII are required to explain the observed excess of this line in their stacked cluster analysis.

We conclude that although it is hard to exclude completely an astrophysical origin of the 3.539 keV line in the spectrum of the GC (due to the complicated nature of this object), the detection of this line in this object is an essential cross-check for the DM interpretation of the signal observed in Perseus and M31 (Boyarsky et al., 2014a) and in the stacked spectra of galaxy clusters (Bulbul et al., 2014a). A non-detection in the GC or a detection with a too high flux would have immediately ruled out this interpretation. As it is, the GC data rather supports this interpretation as the line is not only observed at the same energy, but also its flux is consistent with the expectations about the DM distribution of the GC.

To study this intriguing possibility further, a measurement with higher spectral resolution with respect to the atomic lines, an independent measurement of the relative abundances of elements in the GC region, or analyses of additional deep exposure datasets of DM-dominated objects are needed (Koyama et al., 2014; Lovell et al., 2015; Figueroa-Feliciano et al., 2015; Iakubovskyi, 2015; Speckhard et al., 2016).

	ObsID	Off-center angle arcmin	Cleaned exposure MOS1/MOS2 [ksec]	FoV [arcmin^2] MOS1/MOS2
1	0111350101	0.017	40.8/40.7	570.5/570.3
2	0111350301	0.017	7.2/6.8	565.8/573.4
3	0112972101	0.087	20.8/21.4	571.4/572.0
4	0202670501	0.003	21.4/26.5	564.9/573.4
5	0202670601	0.003	29.6/31.1	563.8/574.1
6	0202670701	0.003	76.0/80.0	570.4/573.3
7	0202670801	0.003	86.9/91.0	569.2/572.8
8	0402430301[a]	0.002	57.6/60.2	475.8/572.1
9	0402430401[a]	0.002	37.3/37.8	476.2/572.3
10	0402430701[a]	0.002	23.1/25.2	478.5/573.1
11	0504940201[a]	0.286	7.7/8.5	487.6/572.6
12	0505670101[a]	0.002	65.7/73.7	472.0/573.2
13	0554750401	0.003	31.6/31.5	483.4/574.0
14	0554750501	0.003	39.6/39.2	487.0/574.0
15	0554750601	0.003	35.5/36.4	487.0/573.3
16	0604300601	0.003	28.9/30.0	487.1/573.1
17	0604300701	0.003	35.1/37.1	487.4/572.7
18	0604300801	0.003	34.9/34.2	487.8/572.5
19	0604300901	0.003	21.1/20.7	485.1/574.0
20	0604301001	0.003	35.3/38.6	487.4/573.6
21	0658600101	0.078	46.5/47.6	477.2/573.0
22	0658600201	0.078	38.3/39.7	478.3/572.3
23	0674600601	0.002	9.0/9.4	483.2/573.8
24	0674600701	0.003	12.8/13.5	484.9/575.0
25	0674600801	0.003	17.9/18.2	481.4/574.1
26	0674601001	0.003	20.0/21.5	480.9/573.7
27	0674601101	0.003	10.1/10.7	480.4/573.8

Table 2.7: Properties of the XMM observations of the Galactic Center used in our analysis. We have only used observations with centers located within 0.5' around Sgr A*. The difference in FoVs between MOS1 and MOS2 cameras is due to the loss CCD6 in MOS1 camera, see (Abbey et al., 2006) for details.
[a] Observation discarded from our analysis due to flares in Sgr a*, see Fig. 2.11 and (Porquet et al., 2008).

2.3.4 Dark Matter Profiles of the Milky Way

The distribution of dark matter in galaxies, galaxy groups and galaxy clusters can be described by several density profiles. In this work we concentrated on four popular choices for dark matter density profiles.

I. Numerical (N-body) simulations of the cold dark matter model have shown that the dark matter distribution in all relaxed halos can be fitted with the universal Navarro-Frenk-White (NFW) profile (Navarro et al., 1997)

$$\rho_{\mathrm{NFW}}(r) = \frac{\rho_s r_s}{r(1 + r/r_s)^2} \tag{2.3}$$
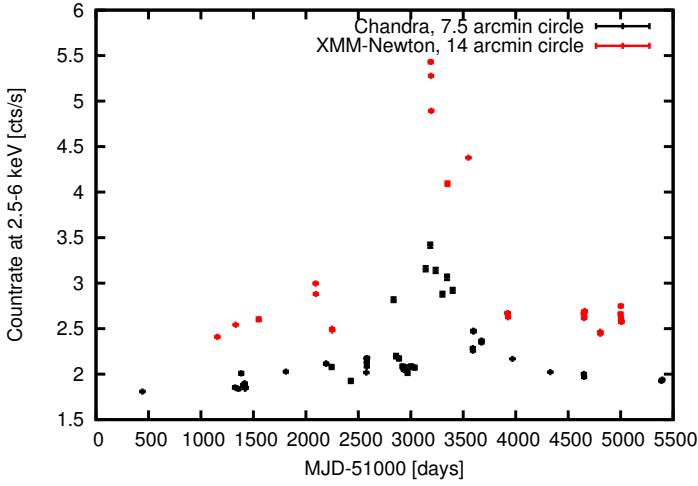
parametrised by ρ_s and r_s.

Figure 2.11: Average count rates on regions centered in Sgr a* using *XMM-Newton* (red) and *Chandra* (black). The enhancement at MJD 54000-54500 are due to strong flaring activity of Sgr a*, see (Porquet et al., 2008) for details. 5 *XMM-Newton* observations during this flaring period were discarded from our analysis, see Table 2.7 for details.

Ion	Position keV	Upper level	Lover level	Emissivity ph cm^3 s^{-1}	T_e peak keV	Relative intensity
Ca XIX	3.902	7	1	3.913e-18	2.725e+0	0.59
Ca XIX	3.883	5	1	6.730e-19	2.725e+0	0.10
Ca XIX	3.861	2	1	1.242e-18	2.165e+0	0.19
Ar XVII	3.685	13	1	8.894e-19	1.719e+0	0.13
Ar XVII	3.683	11	1	3.729e-20	1.719e+0	0.01
Ar XVII	3.618	10077	2	3.627e-20	1.366e+0	0.01
Ar XVII	3.617	10078	3	9.355e-20	1.366e+0	0.01
Ar XVIII	3.323	4	1	4.052e-18	3.431e+0	0.61
Ar XVIII	3.318	3	1	2.061e-18	3.431e+0	0.31
S XVI	3.276	12	1	9.146e-19	2.165e+0	0.14
Ar XVII	3.140	7	1	6.604e-18	1.719e+0	1.00
Ar XVII	3.126	6	1	7.344e-19	1.719e+0	0.11
Ar XVII	3.124	5	1	1.018e-18	1.719e+0	0.15
S XVI	3.107	7	1	3.126e-18	2.165e+0	0.47
S XVI	3.106	6	1	1.584e-18	2.165e+0	0.24
Ar XVII	3.104	2	1	2.575e-18	1.719e+0	0.39
S XV	3.101	37	1	7.252e-19	1.366e+0	0.11
S XV	3.033	23	1	1.556e-18	1.366e+0	0.24

Table 2.8: List of astrophysical lines at 3-4 keV expected in our model. Basic line parameters such as energy, type of ion, type of transition – are taken from AtomDB database. Only the strongest lines are shown. Close lines of the same ion are grouped with horizontal lines.

II. The Burkert (BURK) profile (Burkert, 1995) has been shown to be successful in

explaining the kinematics of disk systems (e.g. Gentile et al., 2004):

$$\rho_{\text{BURK}}(r) = \frac{\rho_B r_B^3}{(r_B + r)(r_B^2 + r^2)}. \tag{2.4}$$

III. Another common parametrizations of cored profiles are given by the pseudo-isothermal (ISO) profile (Kent, 1986)

$$\rho_{\text{ISO}}(r) = \frac{\rho_c}{1 + r^2/r_c^2}. \tag{2.5}$$

IV. The profile found by Moore et al. (1999) from simulations is described by:

$$\rho_{\text{MOORE}}(r) = \frac{\rho_c}{\sqrt{r/r_s}(1 + \sqrt{r/r_s})} \tag{2.6}$$

V. Binney & Evans (2001) found a profile from lensing data of the MW with the following general shape (BE in the following):

$$\rho_{\text{BE}}(r) = \frac{\rho_c}{(r/r_s)(1 + (r/r_s))^{2.7}} \tag{2.7}$$

Because we reside in the inner part of Milky Way dark matter halo, it is the only object whose dark matter decay signal would be spread across the whole sky. The dark matter column density for the Milky Way halo can be calculated using the expression (Boyarsky et al., 2007b)

$$S_{DM}^{MW}(\phi) = \int\limits_0^\infty \rho_{DM}\left(r(z,\phi)\right) dz \tag{2.8}$$

where $r(z, \phi) = \sqrt{r_\odot^2 + z^2 - 2zr_\odot \cos\phi}$ is the distance from the galactic center with z the distance along the line of sight and ϕ the angle away from the GC for an observer at earth (itself at $r_\odot$ from the GC). Expressed in galactic coordinates (l, b)

$$\cos\phi = \cos b \cos l. \tag{2.9}$$

It can be seen (e.g., Boyarsky et al., 2006c, 2008b, 2007b) that the function S_{DM}^{MW} can change only by a factor of few, when moving from the Galactic center ($\phi = 0°$) to the anti-center ($\phi = 180°$). That is, the Milky Way contribution to the decay is an all-sky signal.

The flux received at earth produced by dark matter decaying inside the cone of view, we can approximate by

$$F_{DM}^{FoV} = S_{DM}^{MW}(\phi)\Omega\Gamma/4\pi \tag{2.10}$$

in photons s^{-1} cm^{-2}, with Ω the size of the field of view in sr, Γ the decay width and the 4π to complete the distance modulus (the distance is already included in the Ω).

The exact solution, taking into account the varying density over the field of view, is

$$F_{DM}^{FoV} = \Sigma_{DM}^{FoV}\Gamma/4\pi \tag{2.11}$$

$$\Sigma_{DM}^{FoV} = 2\pi \int\limits_{\phi=0}^{\phi=\omega} \int\limits_{z=o}^{z=\infty} \frac{\rho(r(z,\phi))}{z^2} z^2 \sin(\phi) d\phi dz \tag{2.12}$$

for a circular field of view centered on the GC, with a radius of ω.

The mass modeling of the Milky Way is continuously updated and improved (see e.g., Nesti & Salucci, 2013; Deason et al., 2012; Bernal & Palomares-Ruiz, 2012; McMillan, 2011; Sofue et al., 2009; Xue et al., 2008; Smith et al., 2007; Battaglia et al., 2006; Alcock et al., 1996; Merrifield, 1992; Weber & de Boer, 2010). In Table 2.9 we summarize recent results. We are interested in predicting the flux from dark matter decay based on the dark matter content. Therefore, using the DM distributions in the MW as reported in this table, we compute Σ_{DM}^{FoV} for the galactic center and blank sky observations. In the galactic center case, we perform the integral in eq. 2.12 for $\omega = 14'$, and then correct the results for detector gaps with the ratio of the exposure-weighted average FoV size (corrected for detector gaps) to the size of an ideal 14' FoV. For the blank sky dataset, we computed $S_{DM}^{MW}\Omega$ (see eq. 2.8) for each blank sky pointing (each with its own ϕ), therefore assuming that so far away from the GC the DM density does not vary appreciably over the FoV, and take the exposure and FoV weighted average of all those pointings. It is then, just like the case for the GC, corrected for detector gaps.

Regarding the mass modeling of the Galactic Center, there are additional complications. Firstly, even tough according to Donato et al. (2009) and Gentile et al. (2009), the central surface densities of spiral galaxies are comparable, our field-of-view is only 14' in radius which translates to a physical scale of order 30 pc at the center of the halo, which is much smaller than one scale length. It is unfortunately not possible to observationally determine the DM distribution of the Milky Way within about 3 kpc from the halo center. Secondly, at these small scales, baryons dominate the mass budget and baryon physics may play an important role in shaping the DM distribution, in addition to possible warm dark matter effects. However, the extent of the influence of the processes is not well known. Thirdly, the central 3 kpc of the NFW distributions in Table 2.9 contribute between roughly 80% (least concentrated) to 90% (most concentrated) of the total Σ_{DM}^{FoV} for the GC observations. Therefore the best we can do is extrapolate profiles measured at larger radii down to the lower radii. We remain agnostic about the very central DM distribution and assume that uncertainty is enclosed within the spread in the different types of profiles that we already examined.

Recently, Lovell et al. (2015) analysed the high-resolution Aquarius simulations specifically in order to predict dark matter decay fluxes. Milky Way and Andromeda-like halos from these simulations were selected, and the fluxes determined based on the exposure times and position angles as used in this work and in Boyarsky et al. (2014a). Since the flux in this case is determined solely from the mass inside the field-of-view and the assumed DM particle lifetime, flux and projected mass are interchangeble in this study. This produced a range of fluxes that are in agreement with our projected mass brackets for the GC, and the flux ratios of the GC to M31, and GC to blank-sky. The confidence ranges from Lovell et al. (2015) are tighter than our literature-brackets, therefore we retain the latter in all joint analyses.

To round of this discussion about the dark matter masses, we shortly touch upon the dark matter content of Perseus and Andromeda in order to compare our observations in Figure 2 of our paper. As for the Milky Way, we compile available literature profiles of these objects and use those to determine the total dark matter mass present in the field of view of our observations (Boyarsky et al., 2014a). This is a more straightforward calculation as the physical size of these objects is much smaller than their distance to

Authors	Profile	$r_\odot$ kpc	r_* kpc	ρ_* $10^6 M_\odot/kpc^3$	$\Sigma_{DM,GC}^{FoV}$ $10^{-3}M_\odot/pc^2$	$\Sigma_{DM,BS}^{FoV}$ $10^{-3}M_\odot/pc^2$	GC/BS ratio
Smith et al. (2007)[a]	NFW	8	$25.2^{+6.2}_{-3.8}$	$10.6^{+1.5}_{-1.8}$	$142.6^{+33.3}_{-21.6}$	$5.6^{+1.8}_{-1.1}$	$25.6^{+13.9}_{-9.1}$
	NFW	8	$1.4^{+1.2}_{-0.5}$	$39.6^{+4.5}_{-3.2}$	$35.2^{+11.6}_{-5.7}$	$3.5^{+1.0}_{-0.5}$	$9.9^{+5.5}_{-3.4}$
Weber & de Boer (2010)	NFW[b]	8.33	$20.4^{+17.11}_{-6.4}$	$10.8^{+3.4}_{-3.4}$	$118.0^{+11.0}_{-4.0}$	$4.5^{+0.4}_{-0.4}$	$26.1^{+5.4}_{-3.1}$
	NFW[b]	8.33	$6.32^{+1.26}_{-0.78}$	$25.2^{+4.6}_{-4.6}$	$95.1^{+2.6}_{-2.2}$	$7.1^{+0.6}_{-0.6}$	$13.3^{+1.6}_{-1.3}$
	BE	8.33	$6.58^{+1.3}_{-1.3}$	10.2	$22.0^{+3.5}_{-3.5}$	$4.0^{+0.8}_{-0.8}$	$5.5^{+2.4}_{-1.6}$
	Moore[c]	8.33	$6.58^{+1.3}_{-1.3}$	30	$306.3^{+60.7}_{-60.7}$	$4.0^{+0.8}_{-0.8}$	$77.5^{+38.2}_{-25.6}$
	PISO[d]	8.33	$5.264^{+1.04}_{-1.04}$	5	$11.4^{+2.6}_{-1.8}$	$3.7^{+0.7}_{-0.7}$	$3.1^{+1.7}_{-0.9}$
Battaglia et al. (2005)[e]	NFW	8	11.4	$14.86^{+0.71}_{-0.49}$	$95.1^{+5.3}_{-3.5}$	$5.0^{+0.5}_{-2.3}$	$19.0^{+2.4}_{-2.3}$
&Battaglia et al. (2006)	NFW	8	11.4	$16.12^{+0.44}_{-0.46}$	$103.9^{+3.5}_{-3.5}$	$5.9^{+0.3}_{-0.3}$	$17.7^{+1.6}_{-1.4}$
McMillan (2011)	NFW	8.29	$10.4^{+4.57}_{-2.3}$	$18^{+4.3}_{-4.3}$	$107.4^{+3.1}_{-0.4}$	$6.4^{+0.5}_{-0.5}$	$16.8^{+1.9}_{-1.3}$
Nesti & Salucci (2013)	NFW	8.08 ± 0.2	$13.8^{+20.7}_{-6.6}$	$16.1^{+12.2}_{-5.6}$	$125.9^{+75.6}_{-26.1}$	$7.0^{+3.6}_{-1.3}$	$18.0^{+17.3}_{-8.5}$
	BURK	7.94 ± 0.3	$4.13^{+4.4}_{-1.1}$	$9.26^{+4.0}_{-3.0}$	$22.9^{+42.8}_{-10.1}$	$7.3^{+23.1}_{-4.3}$	$3.2^{+18.9}_{-2.7}$
Xue et al. (2008)[f]	NFW	8	$4.2^{+0.3}_{-0.3}$	$21.9^{+-1}_{1.4}$	$54.6^{+7.0}_{-6.2}$	$3.8^{+0.7}_{-0.5}$	$14.4^{+4.5}_{-3.6}$
	NFW	8	$4.4^{+0.2}_{-0.4}$	$20.8^{+1.1}_{-1}$	$52.8^{+7.0}_{-6.2}$	$3.6^{+0.6}_{-0.6}$	$14.6^{+5.1}_{-3.5}$
	NFW[g]	8	$0.9^{+0.85}_{-0.36}$	$41.1^{+8.3}_{-5.8}$	$25.5^{+12.3}_{-8.8}$	$2.6^{+1.0}_{-0.7}$	$9.8^{+9.9}_{-5.1}$
	NFW[g]	8	$0.47^{+0.32}_{-0.18}$	$60.2^{+7.2}_{-7.2}$	$18.5^{+8.8}_{-5.3}$	$2.3^{+0.9}_{-0.6}$	$8.1^{+7.9}_{-3.9}$

Table 2.9: Overview of dark matter distributions as determined in the literature. r_* and ρ_* refer to the relevant characteristic radius and density for that particular type of profile. Where the profile was given in a different parametrization of the same profile (for example, concentration and virial mass), the values have been converted to r_* and ρ_*. The errors given are 1σ, which are naively converted from the error range given in that work if that range was not 1σ. $\Sigma_{DM,GC}^{FoV}$ (see Eq. 2.12) is the integral over the density of the galactic center inside the field of view of our observations, divided by the distance squared to each infinitesimal mass. $\Sigma_{DM,BS}^{FoV}$ is the same, but for the blank-sky dataset from Boyarsky et al. 2014. The errors on these projected mass densities are either 0.5σ to account for the degeneracy between the 2 parameters of the DM distribution, or 1σ if the fit from that study fixed one of those parameters (for example using a scaling relation between c and M_{vir}). *a)* the two descriptions are using different baryonic disks. *b)* some baryonic parameters are fixed in the fits. These two NFW's are the two extremes with reasonably good fits. *c)* the Moore model is very cuspy by design. *d)* the pseudo-isothermal sphere has an almost flat profile in the center. *e)* the second NFW takes anisotropy into account, and is a better fit that the first. *f)* analysis calibrated on two different simulations. *g)* includes an adiabatic correction.

us. We compute the enclosed projected mass of these literature profiles within the field of view (corrected for detector gaps), weighting by the exposure time of the different exposures, and then divide by the distance to the object squared to arrive at $\Sigma_{DM}^{Perseus}$ and Σ_{DM}^{M31}. For Perseus, we consider the profiles as determined by Reiprich & Boehringer (2002); Chen et al. (2007); Simionescu et al. (2012b); Storm et al. (2013); Ettori et al. (2002); Wojtak & Łokas (2007), and those by Klypin et al. (2002); Geehan et al. (2006); Widrow & Dubinski (2005); Seigar et al. (2008); Tempel et al. (2007); Chemin et al. (2009); Corbelli et al. (2010) for Andromeda.

2.3.5 Ion Abundances and Emission Lines

The Galactic Center is an object with a complicated signature in the X-rays. As Muno et al. (2004) show, not only does the GC show multi-temperature components in the X-ray spectra, these components also vary quite dramatically spatially over the field-of-view of Chandra, which is about half as large as that of XMM-Newton. The low temperature component as measured by Muno et al. (2004) typically has values of $0.7 - 0.9$ keV, while

the high temperature component can be as hot as $6-9$ keV. The spatial variations in the elemental abundances of Si, S, Ar and Ca are reported to be as high as a factor 2 or 3, with only Fe having a reasonable homogeneous distribution. Our integrated spectrum of the entire inner 14' of the GC therefore will be a superposition of all these components, complicating our analysis significantly.

Restricting our modelling to the cleaner parts of the spectrum, 2.8–6.0 keV, we could find a reasonable fit using a single-temperature `vvapec` component with the elemental lines added manually as gaussians, and a folded powerlaw to account for non-thermal emission. No satisfactory two-temperature fits were found for temperatures in the range given by Muno et al. (2004), even when extending the energy range of our analysis[8]. We did not consider more than two temperature components, because it introduces too many degeneracies.

As mentioned, the emission lines from heavy ions are added by hand. We start with the strongest lines known (see Table 2.8), and work our way down so long as the fit requires it. As mentioned, the line detected at 3.539 keV might be influenced by the Ar XVII complex at 3.685 keV and the K XVIII lines at 3.515 and 3.47 keV. To explain the 3.539 keV line with Ar XVII, the width of this line should be much larger $(95-130$ eV) than what can be expected from the instrumental response based on simulations of this Ar complex. In addition, the flux in this Ar XVII complex would be higher than that of the same ion at 3.13 keV, which should not be possible based on the atomic data in Table 2.8.

For the K XVIII lines, it is unfortunately not possible to constrain their contribution to the 3.539 keV line in the same way as for Ar XVII, since we do not have other, stronger, detected lines of the same ion in our spectrum. In this case, one may attempt to predict the ratio of K XVIII flux to the fluxes of ions of other elements such as Ar XVII, Ca XIX, Ca XX, S XVI, etc. based on temperature and relative abundances. Since the GC emission consists of many different temperature and abundance components, it should be necessary to compute an estimate of the K XVIII flux for many different combinations of temperature and abundance. Based on the flux of each of the different detected strong lines in turn and assuming solar abundance (similarly to the analysis of Section 4 of Bulbul et al. (2014a)), the predictions for the K XVII flux can vary by more than an order of magnitude. Even without considering deviations from solar abundance (which may be as large as a factor 3 (Jeltema & Profumo, 2015)), the detected flux in the 3.539 keV line falls within these predictions for a respectable fraction of these physically plausible scenarios. It is therefore not possible *based on the GC data alone* to exclude the astrophysical origin of this 3.539 keV line in the GC.

---

[8]The two-temperature fit can be made satisfactory e.g. by adding 1.2% systematic error in quadrature – a value much larger than the typical systematic errors for line-like uncertainties ($\sim$0.5%, see Sec. 5 of Iakubovskyi (2013) for details). When adding such large errors, the `vvapec` temperatures become consistent with previous works (e.g. Muno et al. (2004)) and the abundances of S, Ar, Ca and K are 0.8-1.2, 1.2-1.8, 1.6-2.4 and 0.3-3.4 Solar values at 68% level, respectively, in full accordance with (Jeltema & Profumo, 2015).

2.4   Literature Response

BASED ON

*Comment on the paper "Dark matter searches going bananas: the contribution of
Potassium (and Chlorine) to the 3.5 keV line" by T. Jeltema and S. Profumo*
Alexey Boyarsky, Jeroen Franse, Dmytro Iakubovskyi, Oleg Ruchayskiy
Published on *arXiv*

In response to Boyarsky et al. (2014a) and Bulbul et al. (2014a), the authors of Jeltema & Profumo (2015) have argued that if one restricts the modeling of the emission of the central part of M31 to the energy range $3 - 4$ keV, and uses a single `powerlaw` as a model of the continuum, the significance of the detection of the line at 3.53 keV in the spectrum of M31 drops below 2σ. They also argued that when one ignores the detection in M31, the line in the spectra of the galaxy clusters and of the Galactic Center can be explained by an atomic transition in the K XVIII ion, provided one also assumes both an abundance of K XVIII and a set of physical conditions in these objects that are hard to exclude.

In this Section we show that restricting the analysis of the M31 spectrum to $3-4$ keV is not justified. The continuum is well modelled by a power law model up to 8 keV and the parameters of this model are well constrained at this wider interval. Limiting the analysis to $3 - 4$ keV only results in increased uncertainty and, although the flux in the 3.53 keV line is consistent with the one reported in (Boyarsky et al., 2014a), the significance of its detection is naturally smaller on the $3-4$ keV than on the whole $2-8$ keV interval, where the astrophysical background is better constrained. We also argue that with the M31 data included, the interpretation of the 3.53 keV line as a K XVIII line in several studied objects together is problematic.

We start by repeating the analysis of (Jeltema & Profumo, 2015): we fit the M31 spectrum over the interval 3–4 keV with a single `powerlaw` (in order to avoid having to model the instrumental background, we subtract it from our spectra.)[9] The fit is good ($\chi^2 = 22.4$ for 27 d.o.f.).[10] The parameters of the `powerlaw` are: PL index 1.65 ± 0.05 (3% relative error), and PL norm $(1.19 \pm 0.07) \times 10^{-3}$ cts/sec/cm^2/keV at 3.5 keV (the relative error being 6.3%). An additional line is detected against this continuum at energy 3.53 keV and with normalization $(2.7 \pm 1.5) \times 10^{-6}$ cts/sec/cm^2 (less than 2σ significance, $\Delta\chi^2 = 3.4$ when adding this line). Thus, we have reproduced both the flux and the significance reported in (Jeltema & Profumo, 2015).

However, once we extend the powerlaw obtained over the interval $3 - 4$ keV to higher energies, we see that it *significantly overpredicts* the count rate in all energy bins above 4 keV as Fig. 2.12 demonstrates.

Let us now compare this result with the fit over the whole interval 2–8 keV (as in Ref. (Boyarsky et al., 2014a)). The wider range of energies allows us to determine the parameters of the `powerlaw` with better precision: PL index 1.71 ± 0.01 (0.5% relative error), PL norm = $(1.18 \pm 0.01) \times 10^{-3}$ cts/sec/cm^2/keV at 3.5 keV (0.7% relative

---

[9]The spectral modeling has been performed with the X-Ray Spectral Fitting Package `Xspec` (Arnaud, 1996) v.12.8.0.

[10]Unlike (Jeltema & Profumo, 2015) we have binned the spectrum by 60 eV (as in (Boyarsky et al., 2014a)) to make bins roughly statistically independent. We verified that our conclusion does not change for finer binning.
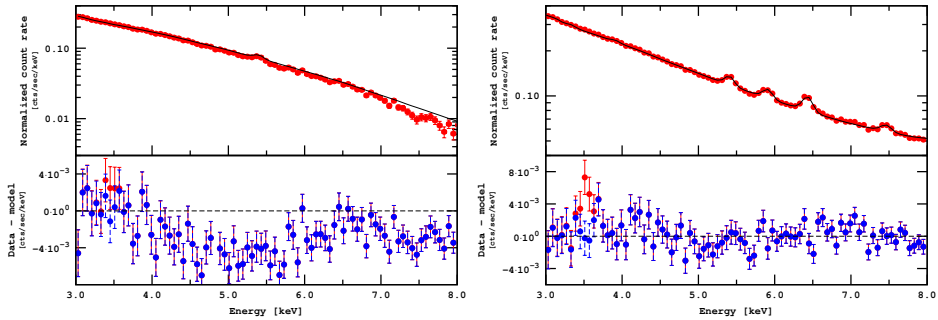
Figure 2.12: *Left panel:* Best fit powerlaw, as determined over the 3–4 keV interval in (Jeltema & Profumo, 2015), extended to higher energies. Such a powerlaw significantly overpredicts the count rate in all bins at $E > 4$ keV. A wide group of near-zero residuals around 6.5 keV corresponds to the complex of lines of iron and other elements (unmodeled). *Right panel:* The data over a wider range of energies processed and fitted in (Boyarsky et al., 2014a)) with the line at 3.53 keV unmodeled. Other lines in the range $3 - 4$ keV are included in the model.

error). The improvement of the quality of fit when adding the line around 3.53 keV was $\Delta\chi^2 = 13$ (which is about 3σ for 2 degrees of freedom: position and normalization of the line). This is the most significant feature in the 3–4 keV range. In Table 2.10 we list all the lines detected in the interval 3–4 keV with significance more than 1σ. Unlike the results of (Jeltema & Profumo, 2015) (see Fig. 3 therein), the lines at 3.91 keV (complex of CA XIX and AR XVII lines) have also been detected in this case with the significance above 2σ. In the case of the fit over the $3 - 4$ keV range, these lines were partially compensated by the powerlaw continuum. In addition, the parameters of the continuum as determined over the narrow range of energies naturally suffer from larger errors (around $3 - 6\%$ for the fit over $3 - 4$ keV interval vs. $0.5 - 0.7\%$ for the fit of (Boyarsky et al., 2014a)). As the flux in the line in question is about 4% of the continuum at these energies, the parameters of the background model should be determined with a precision greater than that in order to reliably detect such a weak line. This explains the reduced best-fit flux and the diminished significance of the line at 3.53 keV.

Finally, we make the observation that complexes of argon, calcium and sulphur at energies 3.14 keV, 3.37 keV and 3.91 keV (of which only the 3.91 keV complex is detected at more than 2σ) have fluxes *lower* than that of the unidentified spectral feature at 3.53 keV. This *challenges* the interpretation of the feature as a K XVIII complex. Indeed,

Line	Position, keV	Flux, ph/sec/cm^2
AR XVII/S XV	3.14 ± 0.04	$2.3 \pm 1.4 \times 10^{-6}$
AR XVIII/S XVI/CL XVI	3.37 ± 0.03	$3.6 \pm 1.4 \times 10^{-6}$
AR XVII/CA XIX	3.91 ± 0.02	$4.3 \pm 1.3 \times 10^{-6}$
DM line candidate	3.53 ± 0.03	$4.9^{+1.6}_{-1.3} \times 10^{-6}$

Table 2.10: Position and flux of lines found in the central part of M31 (Boyarsky et al., 2014a), together with 1σ error ranges.

according to AtomDB v2.0.2 (Foster et al., 2011) K XVIII emissivity is at least an order of magnitude lower than emissivities of the complexes in the intervals $3.85 - 3.95$ keV and $3.08 - 3.18$ keV (see Fig. 2.13 based on the data from (Foster et al., 2011)). This relation between emissivities is based on the assumption of solar abundances for these elements. To change this conclusion a strongly super-solar abundance of K XVIII would be required.

In conclusion: the line 3.53 keV is detected at $\sim 3\sigma$ level in the spectrum of the Andromeda galaxy against a background model with the continuum component constrained at the 2–8 keV interval as in (Boyarsky et al., 2014a). Fitting the data in the much narrower $3 - 4$ keV range reduces the significance of the detection as the sensitivity likewise reduces with less data, however this does not contradict the flux in the line detected in (Boyarsky et al., 2014a). The fit over the narrow interval of energies, as performed in (Jeltema & Profumo, 2015), provides a best fit value of the slope of the power law background that systematically over-predicts the value of the flux above 4 keV, and is therefore significantly ruled out by the whole spectrum.

The observation of the line at 3.53 keV in the center of M31 is in stark contradiction with its interpretation as a K XVIII atomic transition – it would require an extremely supersolar abundance of K XVIII *and* a super-solar ratio of abundance of K XVIII relative to AR XVII and CA XIX. The presence of this line in different types of objects – galaxy clusters, M31, and the Galactic Center – makes it challenging to explain all these signals together by emission from K XVIII, even if this interpretation is hard to exclude from the GC data only.
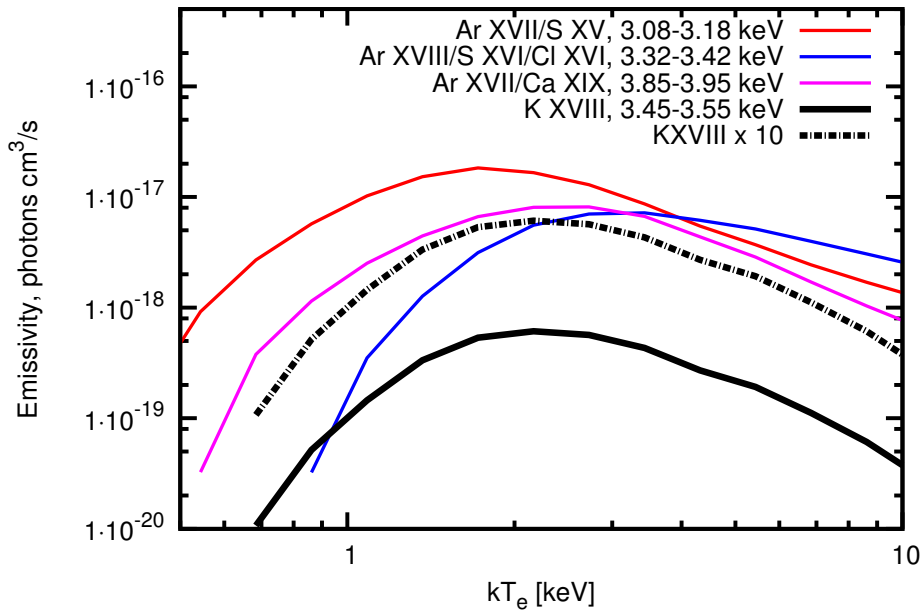
Figure 2.13: Emissivities of different line complexes as a function of plasma temperature (assuming solar abundances of all elements). The emissivity of the K XVIII line complex near 3.5 keV is at least an order of magnitude below those of the other complexes. The data is from AtomDB v2.0.2 (Foster et al., 2011).

3 | DEVOTED OBSERVATIONS OF THE DRACO DWARF SPHEROIDAL

BASED ON

Searching for decaying dark matter in deep XMM-Newton observation of the Draco dwarf spheroidal
Oleg Ruchayskiy, Alexey Boyarsky, Dmytro Iakubovskyi, Esra Bulbul, Dominique Eckert, Jeroen Franse, Denys Malyshev, Maxim Markevitch, Andrii Neronov
Published in *Monthly Notices of the Royal Astronomical Society*

3.1 Introduction

An emission line-like spectral feature at energy $E \sim 3.5$ keV has recently been observed in the long-exposure X-ray observations of a number of dark matter-dominated objects: in a stack of 73 galaxy clusters (Bulbul et al., 2014a) and in the Andromeda galaxy and the Perseus galaxy cluster (Boyarsky et al., 2014a). The possibility that this spectral feature may be the signal from decaying dark matter has sparked a lot of interest in the community, and many dark matter models explaining this signal have been proposed (see e.g. Iakubovskyi (2014) and refs. therein). The signal was subsequently detected in the Galactic Center (Riemer-Sorensen, 2014; Boyarsky et al., 2015; Jeltema & Profumo, 2015; Carlson et al., 2015), in the center of the Perseus galaxy cluster with *Suzaku* (Urban et al., 2015), in a stacked spectrum of a new set of galaxy clusters (Iakubovskyi et al., 2015), but not found in stacked spectra of dwarf spheroidal galaxies (Malyshev et al., 2014), in outskirts of galaxies (Anderson et al., 2015), in the diffuse X-ray background (Figueroa-Feliciano et al., 2015; Sekiya et al., 2015).

There are three classes of non-dark matter explanations: a statistical fluctuation, an unknown systematic effect or an atomic line. Instrumental origins of this signal have been shown to be unlikely for a variety of reasons: the signal is present in the spectra of galaxy clusters in all of *XMM-Newton* detectors and also in *Chandra*, yet it is absent in a very-long exposure *XMM-Newton* (Boyarsky et al., 2014a) or *Suzaku* (Sekiya et al., 2015) blank sky backgrounds. The position of the line in galaxy clusters scales correctly with redshift (Bulbul et al., 2014a; Boyarsky et al., 2014a; Iakubovskyi et al., 2015), and the line has radial surface brightness profiles in the Perseus cluster (except its core (Bul-

bul et al., 2014a)) and Andromeda galaxy (Boyarsky et al., 2014a) consistent with our expectations for decaying dark matter and with the mass distribution in these objects.

The astrophysical explanation of this signal (e.g., an anomalously bright K XVIII line (Bulbul et al., 2014a; Riemer-Sorensen, 2014; Boyarsky et al., 2015; Jeltema & Profumo, 2015; Carlson et al., 2015; Iakubovskyi et al., 2015) or Ar XVII satellite line (Bulbul et al., 2014a), or a Sulfur charge exchange line (Gu et al., 2015)) require a significant stretch of the astrophysical emission models, though they can be unambiguously tested only with the high spectral resolution of the forthcoming *Astro-H* and *Micro-X* (Mitsuda et al., 2014; Koyama et al., 2014; Kitayama et al., 2014; Figueroa-Feliciano et al., 2015; Iakubovskyi, 2015) microcalorimeters.

The dark matter interpretation of the origin of the line allows for a non-trivial consistency check by comparing observations of different objects: the intensity of the line should correlate with the *dark matter column density* – a quantity that is bracketed between roughly $10^2 \, M_\odot/\text{pc}^2$ and few $\times \, 10^3 \, M_\odot/\text{pc}^2$ for all objects from smallest galaxies to larger clusters (Boyarsky et al., 2010a, 2009b). For example, the observation of the 3.5 keV line in M31 and the Perseus cluster puts a *lower limit on the flux* expected from the Galactic Center (GC). On the other hand, the non-detection of any signal in the off-center observations of the Milky Way halo (the blank sky dataset of Boyarsky et al., 2014a) *provides an upper limit* on the possible flux from the GC, given the observational constraints on the DM distribution in the Galaxy. Boyarsky et al. (2015) demonstrated the flux of the 3.5 keV line detected in the GC, falls into this range.

To study this question further, we observed the central $r = 14'$ of the Draco dwarf spheroidal galaxy with *XMM-Newton* with a very deep exposure of 1.4 Msec. Dwarf spheroidal galaxies (dSphs) are the most extreme dark matter-dominated objects known. The observations of thousands of stars in the "classical" dwarf satellites of the Milky Way make possible the determination of their DM content with very low uncertainties, with the Draco dSph being one of the best studied (see Geringer-Sameth et al. (2015) for the latest mass modeling). The relatively small uncertainty on the dark matter column density in Draco and its "faintness" in X-rays due to lack of gas or X-ray binaries allows us to devise a test of the decaying dark matter interpretation of the ∼3.5 keV line, as we have a clear prediction of the expected line flux for Draco based on the masses of this galaxy and the other objects.

A clear detection of the ∼3.5 keV line in Draco would provide very convincing evidence for the decaying DM interpretation, as there is no known physical process that would produce *the same signal* over such a broad range of objects and environments, with an intensity that scales with the DM content, from galaxy clusters of huge masses and large abundances of hot gas, through spiral galaxies, and then all the way down to dwarf galaxies of very low magnitude and negligible gas content.

The estimated column density within the central $14'$ is a factor of a few lower in dSphs (including Draco) than in the centers of nearby spiral galaxies or clusters (albeit has a much lower uncertainty). Therefore, to achieve the same signal-to-noise for a dSph as for a spiral galaxy for all observationally possible ratios of the DM column density, one would need a prohibitively long observation. The uncertainty in DM content of the galaxies becomes crucial. Therefore, the raw exposure time of the Draco observation (1.4 Msec) has been chosen to match the shortest exposure expected to still allow for detection of the weakest possible line (compatible with previous observations).

In this paper we describe the results of the analysis of these Draco observations. We do find weak positive residuals at the predicted energy above the (carefully-modeled) continuum in the PN spectrum and in one of the two MOS spectra, but at a low statistical significance that allows only an upper limit on the line flux to be set. The upper limit is consistent with most of the previous positive line detections, thus, we *cannot exclude dark matter decay* as origin of the 3.5 keV line.

3.2   Data preparation and analysis

We analysed observations of Draco dSph performed in 2015 by the European Photon Imaging Cameras (EPIC; Strüder et al., 2001; Turner et al., 2001) on-board of the X-ray Multi-Mirror Observatory *XMM-Newton* (Jansen et al., 2001) as a part of the AO-14 campaign (proposal 76480, PI: A. Boyarsky). The 1.4 Ms total requested exposure was divided into 26 observations (Table 3.3). We processed these observations from raw data using Extended Source Analysis Software (ESAS; Kuntz & Snowden, 2008) provided as part of the *XMM-Newton* Science Analysis System SAS v.14.0.0, with calibration files current as of December 1, 2015. Time intervals affected by soft proton flares were rejected using ESAS procedure `mos-filter` with standard spectral cuts. This rejection removed $\sim$30% ($\sim$50%) of raw exposure for MOS (PN) cameras, comparable to other methods described in e.g. Sec. 8.4.1 of Iakubovskyi (2013). While the exposure reduction is significant, our tests showed that the sensitivity to the line does not increase if we use less-rigorous cleaning, because of the resulting increase of the continuum brightness. We excised the unrelated X-ray point sources using the ESAS procedure `cheese`, which masks the sky regions *around the detected point sources* of $\geq$36" radius which corresponds to the removal of $\geq$70% per cent of total encircled energy. For each observation, exposures and fields-of-view after removal of proton flares and point sources are listed in Table 3.3. Spectra and response matrices from MOS and PN cameras produced by ESAS procedure `mos-spectra` were then combined using FTOOL `addspec` and binned with FTOOL `grppha` by 65 eV to have excellent statistics ($\sim 1 - 2\%$ rms variation per bin obtained from $\gtrsim 2000$ counts per bin in our spectra – comparable to the expected line excess above the continuum) while still resolving the spectral lines. For PN camera, we additionally corrected the obtained spectra for out-of-time events using the standard procedure.

We stress that for our current purpose, given the low expected flux of the spectral line in question and the limited spectral resolution of the CCD detectors, accurate modeling of the continuum emission in the immediate vicinity of the line is crucial. For this, we must account for all the faint detector lines and features that may bias the continuum even at a percent level. We do this by creating a spectral model that includes the detector and sky X-ray background components as described below. We analyse the spectra in the band 2.8–10 keV (for MOS spectra) and 2.8–6.8 + 10–11 keV for PN spectra (to stay well away from the mirror edges found at $E \lesssim 2.5$ keV) using standard X-ray spectral fitting tool `Xspec`. The region 6.8-10 keV was removed from PN camera to avoid modeling very strong instrumental lines (Ni Kα, Cu Kα, Ni Kβ and Zn Kα, see Table 3.1) that cannot be modeled adequately with simple Gaussian profiles at such good statistics. However, adding the high energy bins (at 10-11 keV) allows us to constrain the slope of

the instrumental continuum.

The instrumental background is modeled by a sum of unfolded broken `powerlaw` continuum and several narrow `gaussians` corresponding to bright fluorescent lines originating inside the instrument. Because astrophysical emission from dwarf spheroidal galaxies is negligible (Gizis et al., 1993; Boyarsky et al., 2007b; Jeltema & Profumo, 2008; Riemer-Sorensen & Hansen, 2009; Boyarsky et al., 2010b; Sonbas et al., 2015), the astrophysical model represents the contribution of the Cosmic X-ray background (CXB) as modeled by a folded `powerlaw` continuum. The best-fit values of the flux and powerlaw index of Cosmic X-ray background were allowed to change within 95% CL to the best-fit values from Moretti et al. (2009). Neutral hydrogen absorption column density was fixed to the weighted value $n_H = 2.25 \times 10^{20}$ cm^{-2} obtained from Leiden-Argentine-Bonn survey (Kalberla et al., 2005) in the direction of Draco. The obtained CXB parameters from MOS1, MOS2 and PN are consistent with each other and with those summarized in Moretti et al. (2009) at < 90 % level. Moreover, if one freezes the CXB parameters in PN camera at the level of MOS1/MOS2 or at the level of Moretti et al. (2009) the best-fit normalization of 3.5 keV line in PN camera changes by no more than 10%, much beyond its statistical errors ($\sim$40 %, according to Eq. 3.1). We conclude therefore that the origin of the positive line-like residual at 3.5 keV seen in PN camera is not due to variation of CXB parameters from its 'conventional' level.

To check for possible instrumental gain variations, we split our datasets into three smaller subsets grouped by observation time, see observations 1-9, 10-17, and 18-26 in Table 3.3. For each dataset, we present the average position for Cr Kα and Mn Kα instrumental lines, see Table 3.2 for details. No systematic gain variations across the datasets is detected.

3.3   Results

The extracted spectra are shown in Fig. 3.1. They are dominated by the instrumental and Cosmic (CXB) X-ray backgrounds, which we will carefully model below to see if there is any residual flux at 3.5 keV. As has been stressed in our previous works, the 3.5 keV line feature is so weak that the continuum in its spectral vicinity has to be modeled to a very high precision to be able to detect the line – more precisely than what's acceptable in the usual X-ray observation.

The basic information about the observations is listed in Table 3.3. As a baseline model, we used the combination of Cosmic X-ray Background (extragalatic `powerlaw` folded with the effective area of the instrument) and instrumental background (instrumental `powerlaw` not folded with instrument response, plus several narrow `gaussians` describing fluorescence lines) components. The model parameters are summarized in Table 3.1; they are consistent with previous measurements and are consistent among MOS1, MOS2 and PN cameras. Particular differences of the models among individual cameras are described below.

Parameter	MOS1	MOS2	PN
CXB `powerlaw` index	$1.40^{+0.32}_{-0.06}$	$1.36^{+0.07}_{-0.08}$	$1.61^{+0.13}_{-0.06}$
CXB `powerlaw` flux at 2-10 keV [10^{-11} erg/sec/cm^2/deg^2]	$1.37^{+0.34}_{-0.67}$	$1.40^{+0.30}_{-0.40}$	$2.03^{+0.38}_{-0.30}$
Instrumental background `powerlaw` index	$0.31^{+0.06}_{-0.05}$	$0.26^{+0.05}_{-0.04}$	$0.36^{+0.03}_{-0.02}$
Extra gaussian line position at $\sim$3.0 keV [keV]	—	$3.045^{+0.032}_{-0.031}$	—
Extra gaussian line flux at $\sim$3.0 keV [10^{-3} cts/s]	—	$0.3^{+0.1}_{-0.2}$	—
K Kα line position [keV]	$3.295^{+0.039}_{-0.046}$	$3.380^{+0.025}_{-0.020}$	—
K Kα line flux [10^{-3} cts/s]	$0.3^{+0.1}_{-0.2}$	$0.5^{+0.1}_{-0.2}$	—
Ca Kα line position [keV]	—	$3.770^{+0.017}_{-0.023}$	—
Ca Kα line flux [10^{-3} cts/s]	—	$0.5^{+0.2}_{-0.1}$	—
Ti Kα line position [keV]	$4.530^{+0.028}_{-0.028}$	—	$4.530^{+0.002}_{-0.014}$
Ti Kα line flux [10^{-3} cts/s]	$0.4^{+0.1}_{-0.1}$	—	$4.6^{+0.4}_{-0.3}$
Cr Kα line position [keV]	$5.420^{+0.005}_{-0.005}$	$5.431^{+0.004}_{-0.005}$	$5.445^{+0.001}_{-0.001}$
Cr Kα line flux [10^{-3} cts/s]	$2.1^{+0.1}_{-0.2}$	$3.7^{+0.2}_{-0.1}$	$11.2^{+0.4}_{-0.3}$
Mn Kα line position [keV]	$5.919^{+0.006}_{-0.008}$	$5.901^{+0.005}_{-0.005}$	$5.910^{+0.014}_{-0.015}$
Mn Kα line flux [10^{-3} cts/s]	$1.8^{+0.1}_{-0.1}$	$3.2^{+0.2}_{-0.1}$	$3.3^{+0.4}_{-0.3}$
Fe Kα line position [keV]	$6.386^{+0.020}_{-0.025}$	$6.424^{+0.006}_{-0.018}$	$6.395^{+0.014}_{-0.013}$
Fe Kα line flux [10^{-3} cts/s]	$1.6^{+0.4}_{-0.5}$	$3.7^{+0.2}_{-1.0}$	$9.7^{+1.1}_{-1.0}$
Fe Kβ line position [keV]	$7.128^{+0.038}_{-0.025}$	$7.148^{+0.037}_{-0.038}$	n/i[a]
Fe Kβ line flux [10^{-3} cts/s]	$0.5^{+0.1}_{-0.1}$	$0.4^{+0.1}_{-0.2}$	n/i[a]
Ni Kα line position [keV]	$7.460^{+0.016}_{-0.015}$	$7.479^{+0.006}_{-0.008}$	n/i[a]
Ni Kα line flux [10^{-3} cts/s]	$0.8^{+0.2}_{-0.1}$	$2.2^{+0.1}_{-0.2}$	n/i[a]
Cu Kα line position [keV]	$8.021^{+0.029}_{-0.026}$	$8.045^{+0.015}_{-0.025}$	n/i[a]
Cu Kα line flux [10^{-3} cts/s]	$0.5^{+0.1}_{-0.1}$	$0.9^{+0.2}_{-0.1}$	n/i[a]
Ni Kβ line position [keV]	$8.251^{+0.039}_{-0.037}$	$8.267^{+0.042}_{-0.052}$	n/i[a]
Ni Kβ line flux [10^{-3} cts/s]	$0.4^{+0.1}_{-0.2}$	$0.4^{+0.1}_{-0.2}$	n/i[a]
Zn Kα line position [keV]	$8.620^{+0.023}_{-0.016}$	$8.629^{+0.021}_{-0.015}$	n/i[a]
Zn Kα line flux [10^{-3} cts/s]	$0.8^{+0.1}_{-0.1}$	$0.9^{+0.2}_{-0.1}$	n/i[a]
Au Lα line position [keV]	$9.716^{+0.007}_{-0.005}$	$9.710^{+0.009}_{-0.004}$	n/i[a]
Au Lα line flux [10^{-3} cts/s]	$3.0^{+0.2}_{-0.2}$	$3.4^{+0.1}_{-0.2}$	n/i[a]
Overall quality of fit (χ^2/dof)	73.8/86	79.3/75	47.0/58

Table 3.1: Model parameters for MOS1, MOS2 and PN cameras including positions and fluxes of instrumental line candidates.

[a] In PN, bright instrumental lines at 7-10 keV are not included (n/i) to our model due to large residuals appearing when these lines are modeled. Instead, we included high-energy range above 10 keV to our PN to improve the instrumental continuum modeling.

Parameter	Cr Kα position [keV]	Mn Kα position [keV]
MOS1, obs. 1-9	$5.427^{+0.013}_{-0.012}$	$5.922^{+0.013}_{-0.013}$
MOS1, obs. 10-17	$5.416^{+0.009}_{-0.006}$	$5.914^{+0.011}_{-0.010}$
MOS1, obs. 18-26	$5.402^{+0.014}_{-0.011}$	$5.930^{+0.031}_{-0.031}$
MOS1, full dataset	$5.420^{+0.005}_{-0.005}$	$5.919^{+0.006}_{-0.008}$
MOS2, obs. 1-9	$5.436^{+0.005}_{-0.007}$	$5.895^{+0.009}_{-0.009}$
MOS2, obs. 10-17	$5.431^{+0.005}_{-0.006}$	$5.918^{+0.008}_{-0.007}$
MOS2, obs. 18-26	$5.431^{+0.008}_{-0.007}$	$5.888^{+0.008}_{-0.008}$
MOS2, full dataset	$5.431^{+0.004}_{-0.005}$	$5.901^{+0.005}_{-0.005}$
PN, obs. 1-9	$5.443^{+0.002}_{-0.013}$	$5.916^{+0.042}_{-0.036}$
PN, obs. 10-17	$5.431^{+0.014}_{-0.001}$	$5.955^{+0.059}_{-0.059}$
PN, obs. 18-26	$5.446^{+0.013}_{-0.001}$	$5.909^{+0.016}_{-0.016}$
PN, full dataset	$5.445^{+0.001}_{-0.001}$	$5.910^{+0.014}_{-0.015}$

Table 3.2: Best-fit positions and 1σ errors for Cr Kα and Mn Kα instrumental lines detected in three different subsets of our dataset grouped by the time of observation, see observations 1-9, 10-17 and 18-26 from Table 3.3. The lines position listed for our full dataset also listed in Table 3.1 is shown for comparison. No systematic gain variations across the datasets is detected.
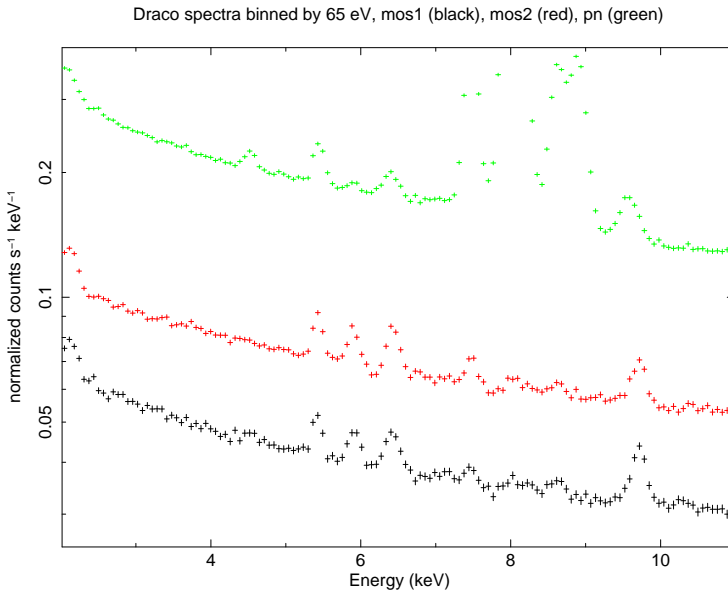

Figure 3.1: Spectra of Draco dwarf spheroidal seen by MOS1 (black), MOS2 (red) and PN (green) cameras.

	ObsID	Observation date MOS1/MOS2/PN	Cleaned exposure [ksec] MOS1/MOS2/PN	Cleaned FoV [arcmin^2] MOS1/MOS2/PN
28	0764800101	2015-03-18	31.6/36.0/12.4	320.7/573.7/553.1
29	0764800301	2015-03-26	23.9/28.2/13.5	319.4/575.2/549.8
30	0764800401	2015-03-28	41.3/42.0/30.5	316.8/571.6/545.3
31	0764800201	2015-04-05	26.1/27.6/17.2	315.4/571.5/549.0
32	0764800501	2015-04-07	47.5/49.5/24.7	314.6/567.1/543.4
33	0764800601	2015-04-09	52.5/52.0/38.9	314.2/568.5/542.9
34	0764800801	2015-04-19	25.4/29.3/12.8	320.3/573.7/554.8
35	0764800901	2015-04-25	36.0/44.2/16.5	318.3/574.3/550.7
36	0770180101	2015-04-27	34.1/35.9/20.9	323.8/579.5/548.2
37	0770180201	2015-05-25	51.9/53.4/32.4	314.2/569.4/541.2
38	0764800701	2015-06-15	54.2/54.5/47.7	312.9/566.3/530.0
39	0770180401	2015-06-18	50.5/50.1/40.3	315.4/564.1/536.2
40	0770180301	2015-07-01	52.5/54.8/47.4	311.4/565.9/535.2
41	0770180501	2015-07-31	49.1/50.2/41.0	315.6/571.0/538.9
42	0770180701	2015-08-22	38.0/38.5/25.2	320.1/572.8/546.8
43	0770180601	2015-09-01	46.6/49.0/26.2	318.5/573.9/548.7
44	0770180801	2015-09-03	64.2/65.8/48.0	322.1/577.9/537.7
45	0770190401	2015-09-11	50.1/50.0/40.2	328.2/583.9/565.8
46	0770190301	2015-09-21	22.5/24.8/11.6	324.1/578.6/554.0
47	0770190101	2015-09-23	18.1/19.5/0.9	334.1/590.5/566.5
48	0770190201	2015-09-25	18.8/20.1/9.3	322.3/579.5/553.9
49	0770190501	2015-10-11	30.8/31.5/20.3	320.2/576.8/542.9
50	0770180901	2015-10-13	19.2/20.8/11.4	324.6/579.1/560.9
51	0770190601	2015-10-15	7.6/11.2/4.6	329.1/584.0/553.8
52	0770190701	2015-10-17	43.7/45.0/35.5	320.5/572.8/537.4
53	0770190801	2015-10-19	31.7/32.5/22.4	326.2/583.2/547.2
	Total		967.8/1016.1/651.8	318.9/573.5/543.9

Table 3.3: Cleaned exposures and fields-of-view for 26 AO14 observations of Draco dSph used in our analysis, see Appendix 3.2 for details. Notable difference between MOS1 and MOS2 fields of view is due to micrometeoroid damages in MOS1, see e.g. Abbey et al. (2006).
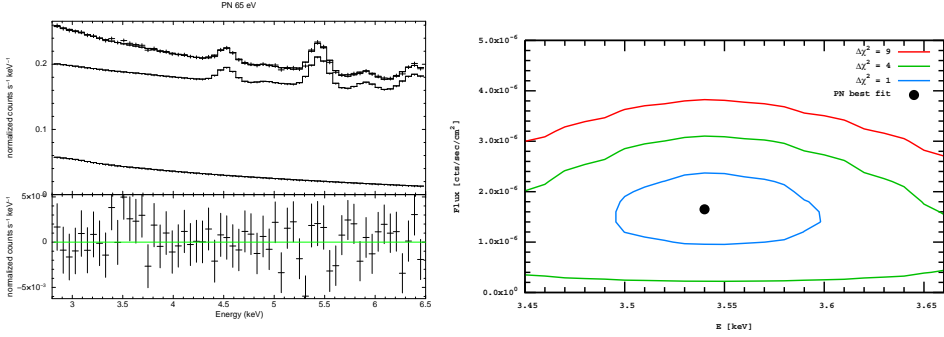
Figure 3.2: Left panel: PN spectrum with *unmodeled* feature at 3.54 keV. Also shown instrumental (upper) and astrophysical (lower) components of the background model. Right panel: Best fit value (black square) and $\Delta\chi^2 = 1, 4, 9$ contours for the line in the PN camera.

3.3.1 Line detection in PN camera

We obtained an excellent fit to the EPIC PN spectrum, with $\chi^2 = 47.0$ for 58 d.o.f. (Table 3.1). The spectrum shows a faint line-like residual at the right energy, $E = 3.54^{+0.06}_{-0.05}$ keV. Its flux is

$$F_{\mathrm{PN}} = \begin{cases} 1.65^{+0.67}_{-0.70} \times 10^{-6} \text{ cts/sec/cm}^2 \\ 3.0^{+1.23}_{-1.29} \times 10^{-9} \text{ cts/sec/cm}^2/\text{arcmin}^2 \end{cases} \tag{3.1}$$

(where the bottom value corresponds to the surface brightness). The improvement of fit when adding the line is $\Delta\chi^2 = 5.3$ for 2 additional d.o.f.. Thus, the detection has a relatively low significance of 2.3σ. The PN spectrum with the unmodeled line-like residual together with the $\Delta\chi^2 = 1, 4, 9$ contours is shown in Figure 3.2. In this Figure, we show only 2.8-6.5 keV range for clarity, while the fit includes higher energies, as described in Appendix 3.2.

3.3.2 MOS cameras

Next we turn to MOS1 and MOS2 cameras. In MOS2 camera, we detected line-like residuals at ~ 3.38 keV (significance 3.2σ) and ~ 3.77 keV (significance 3.5σ), see Table 3.1 in Appendix 3.2. The positions of these residuals are consistent with K Kα and Ca Kα fluorescent lines, respectively. These fluorescent lines have not been previously detected in the MOS cameras, but have been detected in the PN camera with the enhanced calibration source (the so-called `CalClosed` mode, see Fig. 6 of Strüder et al. (2001) for details). Another line-like residual at ~ 3.05 keV is visible (in the MOS2 spectrum only) at a 1.9σ significance; we could not identify it, though its energy is consistent with L and M lines of several heavy metals. In order to get as accurate a continuum model as possible, we have included these weak detector lines as narrow `gaussian` components in our spectral model.

Camera	PN flux [10^{-6} cts/sec/cm^2]	Predicted flux [10^{-6} cts/sec/cm^2]	$\Delta\chi^2$
MOS1, PN best-fit	1.65	0.97	1.58
MOS2, PN best-fit	1.65	1.74	2.23
MOS1, PN 1σ lower	0.95	0.56	0.27
MOS2, PN 1σ lower	0.95	1.00	0.25

Table 3.4: Consistency check of MOS1 and MOS2 cameras with rescaled flux from PN camera. Line position is allowed to vary within 1σ bound for PN, i.e. 3.49–3.60 keV. See also Figures 3.3 and 3.4.
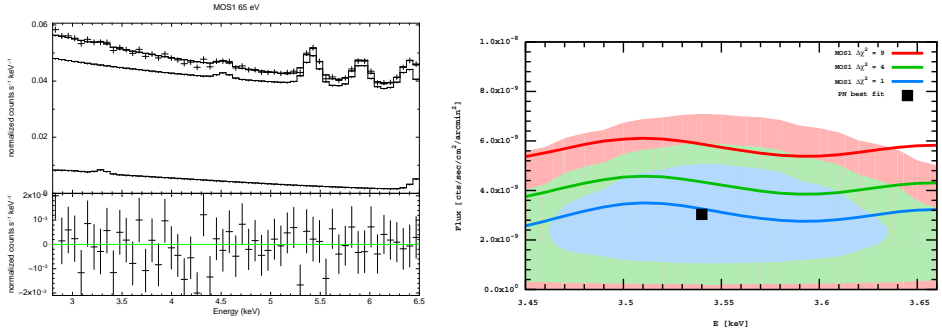

Figure 3.3: *Left panel:* MOS1 spectrum and residuals. *Right panel:* $\Delta\chi^2 = 1, 4, 9$ contours from the MOS1 camera (thick lines). The PN camera contours with $\Delta\chi^2 = 1, 4, 9$ are shown as shaded regions (identical to the contours in Fig. 3.2).

The MOS1 camera reveals no other lines in the region 3–4 keV, see left panel in Figure 3.3. The MOS2 camera has a hint of a residual ($\Delta\chi^2 = 1.2$) in the position 3.60 ± 0.07 keV, see left panel in Figure 3.4. Assuming that the line detected in the PN camera is a physical line, we rescale the PN flux, given by Eq. (3.1), according to the ratio of MOS1 and MOS2 FoV to that of the PN camera (see Table 3.3). Table 3.4 shows the change in the χ^2 (after running the new fit) when one adds a line with a fixed flux to the spectrum of MOS1 and MOS2 (allowing its position to vary within $\pm 1\sigma$ – from 3.49 to 3.60 keV). Clearly the non-observation in MOS1 and MOS2 are consistent with PN observation at $\lesssim 1\sigma$ level.

3.3.3 Common fit of MOS1, MOS2 and PN cameras

Having shown that the three XMM cameras are consistent with each other, we now perform a common fit of all three. We kept the ratio of the gaussian normalisations at ~ 3.5 keV fixed to the ratios of the corresponding FoVs. This is justified if the surface brightness is uniform across the FoV of the XMM cameras. We estimated that assuming instead cuspy Navarro-Frenk-White dark matter profile, the expected surface brightness of 3.5 keV features caused by decaying dark matter differs
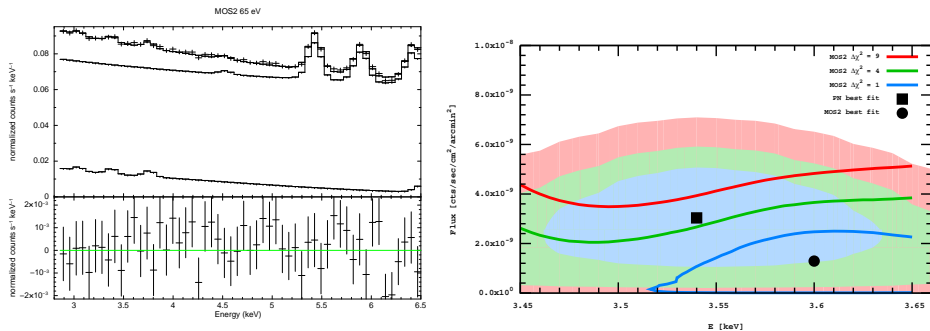
Figure 3.4: *Left panel:* MOS2 spectrum with *unmodeled* feature at ∼3.5 keV and residuals. *Right panel:* $\Delta\chi^2 = 1, 4, 9$ contours from the MOS2 camera (thick lines) and the best fit value (black circle). The PN camera contours with $\Delta\chi^2 = 1, 4, 9$ are shown as shaded regions (identical to the contours in Fig. 3.2).

between the cameras by no more than 15%[1]. This different scaling of the signal between cameras would affect the results of our combined fit by less than 5%. The common fit finds a positive residual with $\Delta\chi^2 = 2.9$ at $E = 3.60 \pm 0.06$ keV and the flux $F = 1.3^{+0.9}_{-0.7} \times 10^{-9} \, \mathrm{cts/sec/cm^2/arcmin^2}$. The resulting flux is compatible with the best-fit PN flux (Eq. 3.1) at a 2σ level.

3.4   Discussion

We analysed 26 observations of Draco dSph performed with the *XMM-Newton* during its AO14 programme. We find a 2.3σ significant positive line-like residual at $E = 3.54 \pm 0.06$ keV in the PN spectrum. A positive 1σ residual is also seen at $E = 3.60 \pm 0.07$ keV with a flux of $F_{\mathrm{MOS2}} = (0.76 \pm 0.66) \times 10^{-6} \, \mathrm{cts/sec/cm^2}$. Their centroids are within 1σ as the right panel of Fig. 3.4 illustrates. The MOS1 camera had the lowest statistics due to the loss of two CCDs. It does not show the line but the absence of the signal is consistent with PN and MOS2 at the 1σ level. The common fit of MOS1, MOS2 and PN camera performed in Sec. 3.3.3 does not show the presence of a significant positive residual at ∼3.5 keV. As it is unclear how the common fit is affected by the uncertainties of cross-calibration between the three cameras, and because we are conservatively interested in this work in exclusion rather than detection, we will use as our main result the 2σ upper bound from the common fit $F_{2\sigma} < 2.9 \times 10^{-9} \, \mathrm{cts/sec/cm^2/arcmin^2}$, which approximately coincides with the best-fit PN flux, see Fig. 3.5.

---

[1]While FoV of MOS1 is smaller than that of MOS2 by 44%, this decrease is largely compensated by the fact that *non-central* CCDs are shut down. So the observation of the central densest part of Draco is not affected.
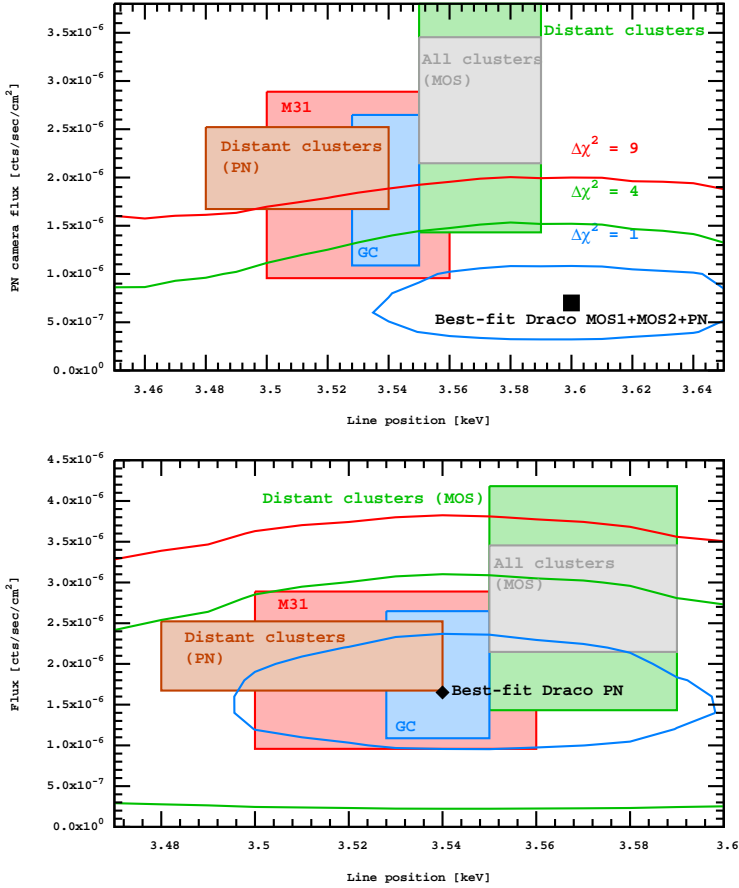
Figure 3.5: *Top:* Common fit to the MOS1, MOS2, and PN cameras (see text for details). The normalization of the 3.5 keV line between cameras is fixed according to the $\Omega_{\rm fov}$ ratios (see Table 3.3). Filled rectangles show the range of fluxes predicted from previous works. The sizes of the regions take into account $\pm 1\sigma$ errors on the measured line fluxes and positions. The height of the rectangles also reflects additional spread in expected DM signals from the specified objects. The previous bounds are based on: Bulbul et al. (2014a) ("All clusters" and "Distant clusters" samples), Boyarsky et al. (2014a) ("M31") and Boyarsky et al. (2015) ("GC"). In particular, for "All clusters" and "Distant clusters" samples, we included an additional 20% uncertainty on its expected DM signal compared to the average values shown in Table 5 of Bulbul et al. (2014a), see Sec. 4.1.2 of Vikhlinin et al. (2009) for detailed discussion. *Bottom:* same as the left panel, but showing the Draco best fit for the PN camera only and the corresponding $\Delta\chi^2$ contours (note the different x and y ranges).

3.4.1 Implications for dark matter decay lifetime

If one interprets this signal as a line from the dark matter decay, its flux is related to the dark matter particle's lifetime τ_{DM} via

$$F = \frac{M_{\text{fov}}}{4\pi D_L^2} \frac{1}{\tau_{DM} m_{DM}} = \frac{\Omega_{\text{fov}}}{4\pi} S_{DM} \frac{1}{\tau_{DM} m_{DM}} \tag{3.2}$$

where m_{DM} is the DM particle mass (equal to $2 \times E_{\text{line}}$), M_{fov} is the DM mass in the field-of-view of the camera, D_L is the luminosity distance, and in the second equality we introduced the *average DM column density*, S_{DM} within the FoV Ω_{fov}.

The expected DM signal from Draco dSph is estimated based on the most recent stellar kinematics data, modeled in Geringer-Sameth et al. (2015). The average column density of Draco within the central $14'$ is $S_{\text{Dra}} = 168 \, \text{M}_\odot/\text{pc}^2$ (with a typical error of $\sim 20\%$; Geringer-Sameth et al., 2015). An additional contribution from the Milky Way halo in the direction of the Draco dSph was adopted at the level of $S_{\text{MW}} = 93 \, \text{M}_\odot/\text{pc}^2$ – based on the profile of Weber & de Boer (2010). The scatter in the values of the MW column density ranges from $56 \, \text{M}_\odot/\text{pc}^2$ (Xue et al., 2008) to $141 \, \text{M}_\odot/\text{pc}^2$ (Nesti & Salucci, 2013). The resulting column density we adopt in the direction of Draco is $S_{\text{Dra}} = 261^{+82}_{-65} \, \text{M}_\odot/\text{pc}^2$.

The corresponding lifetime, inferred from the Draco PN camera observation is $\tau_{\text{Dra}} = (5.1 - 21.9) \times 10^{27}$ sec depending on dark matter column densities in the direction of Draco:

$$\tau_{\text{Dra}} = \begin{cases} 9.6^{+7.1}_{-2.8} \times 10^{27} \text{sec} & S_{\text{Dra}} = (168 + 93) \text{M}_\odot/\text{pc}^2 \\ 7.2^{+5.3}_{-2.1} \times 10^{27} \text{sec} & S_{\text{Dra}} = (140 + 56) \text{M}_\odot/\text{pc}^2 \\ 12.6^{+9.3}_{-3.7} \times 10^{27} \text{sec} & S_{\text{Dra}} = (202 + 141) \text{M}_\odot/\text{pc}^2 \end{cases} \tag{3.3}$$

3.4.2 Comparison with the previous studies of the 3.5 keV line

Is this lifetime of this line compatible with the previous observations of 3.5 keV line? The answer is affirmative (see Fig. 3.5). The comparison with the previous detection in the central $14'$ of the Andromeda galaxy (M31) depends on both uncertainty of the flux measurement and the column density in the direction of the central part of M31, S_{M31}. The DM column density in the central $14'$ has been estimated in Boyarsky et al. (2008a, 2010b, 2014a) and references therein. In this work, we adopt two values of S_{M31}: $S_{\text{M31,med}} = 600 \, \text{M}_\odot/\text{pc}^2$ (based on profile from Widrow & Dubinski, 2005) and $S_{\text{M31,max}} = 1000 \, \text{M}_\odot/\text{pc}^2$ (based on Geehan et al. (2006); Tempel et al. (2007), see Boyarsky et al. (2008a, 2010b) for the discussion of various profiles). The typical errors on M31 column densities are at the order of 50%. Notice, that a maximal disk large core profile of Corbelli et al. (2010) having $S \approx 120 \, \text{M}_\odot/\text{pc}^2$ would be incompatible with DM interpretation of the signal. The predicted lifetime would be too short to be consistent with the strength of the signal. This reiterates the conclusion, already made in Boyarsky et al. (2015) – the dark matter interpretation of the 3.5 keV line holds only if the density profiles of spiral galaxies (M31 and Milky Way) are cuspy.

The DM distributions in the Galactic Center region have been summarized in Boyarsky et al. (2015). As a DM column density proxy, we used the distribution of Smith et al. (2007) that gives $S_{\text{GC}} = 3370 \, \text{M}_\odot/\text{pc}^2$. The spread of allowed values of column

Object/ Camera	Observed flux [10^{-6} cts/sec/cm^2]	S_{DM} [$M_\odot$/pc^2]	τ_{DM} [10^{27} sec]	Predicted flux [10^{-6} cts/sec/cm^2] MOS1	MOS2	PN
M31 (MOS)	$4.9^{+1.6}_{-1.3}$	600	$7.3^{+2.6}_{-1.8}$	$1.28^{+0.42}_{-0.34}$	$2.31^{+0.76}_{-0.61}$	$2.20^{+0.72}_{-0.58}$
		1000	$12.2^{+4.4}_{-3.0}$	$0.77^{+0.25}_{-0.20}$	$1.38^{+0.45}_{-0.37}$	$1.32^{+0.43}_{-0.35}$
73 (all) stacked clusters (MOS)	$4.0^{+0.8}_{-0.8}$	430	$5.7^{+1.7}_{-1.5}$	$1.65^{+0.59}_{-0.38}$	$2.98^{+1.06}_{-0.68}$	$2.82^{+1.01}_{-0.65}$
69 (distant) stacked clusters (MOS)	$2.1^{+0.4}_{-0.5}$	255	$6.8^{+2.1}_{-2.1}$	$1.38^{+0.43}_{-0.43}$	$2.50^{+0.77}_{-0.77}$	$2.36^{+0.73}_{-0.73}$
Perseus with core (MOS)	$52.0^{+24.1}_{-15.2}$	682	$0.75^{+0.23}_{-0.27}$	$12.5^{+7.0}_{-2.9}$	$22.7^{+12.8}_{-5.3}$	$21.4^{+12.0}_{-5.0}$
GC (MOS)	24^{+12}_{-11}	3370†	$7.9^{+6.7}_{-2.6}$	$1.19^{+0.58}_{-0.55}$	$2.15^{+1.05}_{-0.99}$	$2.03^{+1.00}_{-0.93}$

Table 3.5: Predicted line flux based on Boyarsky et al. (2015); Boyarsky et al. (2014a); Bulbul et al. (2014a). The value for the Draco-deduced lifetime, τ_{Dra} is show in Eq. (3.3).
†: from Smith et al. (2007)

density for the Galactic Center distributions is larger than an order of magnitude, see Fig. 2 of Boyarsky et al. (2015).

Lovell et al. (2015) analysed Milky Way-like halos in the Aquarius simulation, identifying DM halos that could be considered as hosting Draco dSph. It was found that the best agreement between the simulations and observational constraints is for $\tau \sim (6-10) \times 10^{27}$ sec (with which the Draco-deduced lifetime from Eq. 3.3 is fully consistent). They also predicted the ratio of fluxes $F_{\mathrm{Dra}}/F_{\mathrm{GC}}$ to peak at 0.09 with the scatter ranging from 0.04 to 0.2 (95% range). Again, the ratio of the fluxes (~ 0.07) inferred in this paper based on Draco PN data is close to the most probably value predicted by Lovell et al. (2015).

The dark matter column density of the combined sample of galaxy clusters is given by Table 5 of Bulbul et al. (2014a). For the sample of "all distant clusters" considered here, the mean value of DM column density is $S_{\mathrm{clusters}} = 255\,\mathrm{M}_\odot/\mathrm{pc}^2$ and we assign an additional 20% error to this data according to Sec. 4.1.2 of Vikhlinin et al. (2009). Notice that the relative errorbars on individual central column densities are of the order ~ 2, see e.g. Table I of Iakubovskyi et al. (2015). The resulting lifetime is again listed in Table 3.5 and is consistent with our measurements.

Finally, a number of works (Bulbul et al., 2014a; Urban et al., 2015; Boyarsky et al., 2015; Tamura et al., 2015) already observed that the line from the central region of Perseus galaxy cluster is too strong to be compatible with other detections. This signal can only be reconciled with the simple decaying DM hypothesis either if there is a strong additional emission from the atomic lines (e.g., Ar XVII satellite line; Bulbul et al., 2014a) in the central region, or if there is a clump of dark matter, making the central column density much larger than estimated based on the temperature profiles (Bulbul et al., 2014a). The forthcoming *Astro-H* mission (Kitayama et al., 2014; Mitsuda et al., 2014; Takahashi et al., 2012) will be able to resolve the issue with the origin of the emission from the Perseus center, both in core and outskirts, as well as in other bright clusters. On the other hand, outskirts of the Perseus cluster, considered in Boyarsky et al. (2014a) are compatible with the decaying DM interpretation for lifetimes up to 8×10^{27} sec, compatible with Draco-deduced lifetime within 1σ.

3.4.3   Comparison with another recent analysis of Draco extended dataset

In a recent paper (Jeltema & Profumo, 2016, JP16 in what follows), different results of the analysis of the same Draco dSph data have been reported claiming that the dark matter interpretation of the 3.5 keV line is excluded at 99% CL. It is difficult to explain the discrepancies with our results without knowing the details of their data analysis. But we expect that the combination of the following factors may be important here. *(i)* The continuum model of JP16 does not include the extragalactic `powerlaw` component, which affects the shape of the continuum in the 3–4 keV range at the level of a few % in a non-trivial, non-monotonic way due to the energy dependence of the effective area. *(ii)* The lines at ~ 3.3 keV and 3.7 keV are detected but unmodeled in JP16. Again, this increases the best-fit continuum level in the energy range 3–4 keV, which would artificially strengthen the upper bound on a 3.5 keV line. *(iii)* JP16 give the highest weight to their more stringent MOS upper limit. As we see in our spectra, the PN camera shows a positive $\sim 2\sigma$ residual at the expected line energy. When searching for weak signals at or below the telescope sensitivity, it is statistically proper to combine results from the independent detectors (provided they are mutually consistent), as we do. There is no reason to neglect the PN constraint – especially since in this case it is the most sensitive camera of the three, even with the shortest clean exposure.

4 | PERSEUS OUT TO R_{200} WITH SUZAKU

4.1 Introduction

The recent discovery of the unidentified X-ray line at $\sim$3.5 keV in the stacked *XMM-Newton* and *Chandra* observations of 73 galaxy clusters and in M31 and its possible interpretation as a decaying dark matter have attracted great attention from the community (Bulbul et al. (2014a); Boyarsky et al. (2014a), Bu14 and Bo14 respectively from here on). The signal is significantly detected in the center of Perseus (the X-ray brightest cluster on the sky) by the *XMM-Newton* and *Chandra* satellites (and later confirmed with *Suzaku*; see Urban et al., 2015) and in its outskirts with *XMM-Newton* (Bo14). The signal is also observed in the Galactic Center (Boyarsky et al., 2015; Jeltema & Profumo, 2015).

Although there has been an extensive effort in the community, the origin of the line is still quite uncertain. Among the three possible interpretations of the line are an instrumental feature, an astrophysical line (e.g., from the intracluster plasma), and emission from dark matter decay or annihilation processes. An instrumental line or calibration errors as possible origins of the 3.5 keV line are extensively studied in the original discovery papers by Bu14 and Bo14. Bu14's analysis, in particular, argues that stacking blue-shifted spectra of a large sample of galaxy clusters with a wide redshift range excludes the instrumental artifact. The detection of the line by several detectors on board of *Chandra*, *XMM-Newton*, and *Suzaku* indicates that it is unlikely due to an instrumental artifact. Furthermore, non-detections in deep exposures of 'blank-sky' background observations with *XMM-Newton* and *Suzaku* also exclude an instrumental artifact (Bo14; Sekiya et al., 2015).

Another possible interpretation of the $\sim$3.5 keV line is spectral confusion with one

of a number of nearby weak astrophysical lines of K XVIII, Cl XVII, and Ar XVII, or possible lines from charge exchange in the intra-cluster medium. This has been extensively discussed in Bu14. Atomic transitions, specifically from the K XVIII and Ar XVII ions are hard to unambiguously distinguish from the 3.5 keV line due to the instruments' spectral resolution (CCD resolution is 100–120 eV FWHM at this energy). Bu14 report that abundances of a 10–20 times solar are required to explain the 3.5 keV excess with any of these lines based on the estimates obtained from the observed S and Ca line ratios. Jeltema & Profumo (2014, 2015) and Carlson et al. (2015) argue that an atomic transition from K XVIII in cool <1 keV plasma is likely to be responsible for the 3.5 keV line. In a comment to these studies, Bulbul et al. (2014b) showed that the observed line ratios are inconsistent with the existence of any significant quantities of cool gas in clusters used in the Bu14 sample. We address further issues with the updated paper by Jeltema & Profumo (2015) and Carlson et al. (2015) in Appendix 6.3. A recent study by (Gu et al., 2015) suggests an alternative explanation for the line, i.e. charge exchange with bare sulfur ions at 3.48 keV. This interpretation is discussed in Appendix 6.1.

A more exotic explanation of the 3.5 keV line is emission from decaying dark matter (Bu14; Bo14; Boyarsky et al. (2014a); Boyarsky et al. (2014b)). Although the line intensity in the Perseus cluster core appears to be five times brighter than the flux in the stacked clusters if one scales the predicted fluxes with cluster mass as expected for dark matter decay (see Bu14), the relative intensities between other objects (M31, Galactic Center, clusters), and the surface brightness distribution within the Perseus cluster (from *XMM-Newton* measurements outside the core) are consistent with a decaying dark matter feature (Boyarsky et al., 2014a; Boyarsky et al., 2015). The detection in the Galactic center is consistent with the decaying dark matter interpretation, although this result does not exclude K XVIII as a possible origin (Boyarsky et al., 2015). The upper limits derived from the blank-sky observations (since these contain dark matter in the field of view from the Galaxy's dark matter halo) are consistent with the fluxes reported by previous studies. On the other hand, non-detections in several other studies, for instance, in stacked galaxies (Anderson et al., 2015) and in dwarf galaxies (Malyshev et al., 2014) challenge the decaying dark matter interpretation of the line. However, the reported statistical tensions across these objects are mild, at a level of 2–3σ (with the exception of the stacked galaxies). Recently, Ruchayskiy et al. (2015) reported on the analysis of newly obtained very-long-exposure *XMM-Newton* data of the Draco satellite galaxy. A small hint of ∼3.5 keV emission was identified although the authors conservatively focus on the upper limits and determine that it is consistent with a decaying dark matter origin based on the dark matter content of the object. In another work regarding the same Draco data, Jeltema & Profumo (2016) claim a much stronger limit on the possible ∼3.5 keV line flux that is at odds with a dark matter decay interpretation. Ruchayskiy et al. (2015) suggests mainly that their more thorough spectral modeling provides a more accurate continuum model. Primary differences include additional physically motivated model components and a wider spectral fitting range (Iakubovskyi et al. (in prep.) offers a quantitative description of this effect). This influences the line flux limits and brings them in agreement with the previous detections of the 3.5 keV line. Most recently, Bulbul et al. (2016a) reported a weak spectral excess around 3.5 keV in the stacked *Suzaku* observations of 47 galaxy clusters. The upper limits derived from their analysis are consistent with the detection from the stacked clusters. However, their sample excludes the Perseus cluster which is in tension

with the previously reported line flux observed with *XMM-Newton*.

In this work we take a further step to examine the spatial distribution of the 3.5 keV line within the Perseus cluster from its core to outskirts with *Suzaku*. The 3.5 keV line is detected in the observations of the core of the Perseus cluster in both the central 6′ and in the surrounding area within *Suzaku*'s field-of-view by Urban et al. (2015). The authors confirm the finding of Bu14 that the flux of the 3.5 keV line in the core is too strong for a decaying dark matter interpretation that assumes a single spherical dark matter distribution for the cluster (as measured by Simionescu et al. (2011)). Urban et al. (2015) also studied 3 other clusters observed with *Suzaku*, and did not detect any 3.5 keV line flux in them. These non-detections are consistent with the previous results for other clusters and samples (Bu14; Bo14; Boyarsky et al., 2015). We note that Tamura et al. (2015) also studied the same *Suzaku* observations of Perseus, but do not find evidence of excess emission around 3.5 keV; the origin of this discrepancy is unclear and we will discuss it below.

We here present the analysis of additional *Suzaku* data that extend the previous studies to greater radii. This paper is organized as follows: in Section 4.2, we describe the *Suzaku* data reduction and analysis. In Section 4.3, we provide our results in the cluster center and in the outskirts. We discuss systematic errors that are relevant to the *Suzaku* X-ray measurements at large radii in Section 4.2.1. In Sections 4.4 and 4.5 we discuss our results and present our conclusions. Throughout the paper, a standard ΛCDM cosmology with $H_0 = 70$ km s^{-1} Mpc^{-1}, $\Omega_\Lambda = 0.7$, and $\Omega_M = 0.3$ is assumed. In this cosmology, 1′ at the distance of the cluster corresponds to ~ 21.2 kpc. Unless otherwise stated, reported errors correspond to 68% (90%) confidence intervals.

4.2 Data Reduction and Analysis

The Perseus cluster has been observed with *Suzaku* between 2006 and 2015 for a total 2.3 Ms. We process the *Suzaku* data with HEASOFT version 6.13, and the latest calibration database CALDB as of May 2014. The raw event files are filtered using the FTOOL *aepipeline*. The detailed steps of the data processing and filtering are given in Bulbul et al. (2016b). The *Suzaku* observations utilized in this work and net exposure times of each pointing after filtering are given in Table 4.8.

Point sources in the FOV are detected from the *Suzaku* data using CIAO's *wavdetect* tool. The detection is performed using *Suzaku*'s half-power radius of 1′ as the wavelet radius as described in (Urban et al., 2015). The detected point sources are excluded from further analysis. Spectra are extracted from the filtered event files in *XSELECT*. Corresponding detector redistribution function (RMF) and ancillary response function (ARF) files are constructed using the *xisrmfgen* and *xisarfgen* tools. The Night-Earth background spectra are generated using the *xisnxbgen* tool and subtracted from each total spectrum prior to fitting.

We co-add front-illuminated (FI) XIS0 and XIS3 data to simplify spectral fitting using FTOOL *mathpha*. The back-illuminated (BI) XIS1 data are co-added separately. The exposure-weighted and normalized ARFs and RMFs are stacked using the FTOOLS *addarf* and *addrmf*. The NXB subtracted FI and BI observations are modeled simultaneously in the 1.95 to 6 keV energy band. Following the same approach of Bu14, we model

| Region | inner d | outer d | inner d | outer d |
Name	*arcmin*	*arcmin*	*kpc*	*kpc*
Region 1	0	8.3	0	182
Region 1a	0	2	0	44
Region 1b	2	4.5	44	98
Region 1c	4.5	8.3	98	182
Region 2	8.3	25	182	545
Region 3	25	40	545	873
Region 4	40	130	873	2836
Region 2-4	8.3	130	182	2836

Table 4.1: Definitions of the used spectral extraction regions in arcmin and kpc from the cluster center. 'Region 2-4' is the combination of Regions 2 through 4 (the full off-center dataset).

the FI and BI observations with the line-free multi-temperature *apec* models and additional Gaussian models for all the relevant atomic transitions, to allow maximum modeling freedom within physical reason. The free parameters of the model are tied between the FI and BI observations. XSPEC v12.9 is used to perform the spectral fits with the ATOMDB version 2.0.2 (Foster et al., 2012). The galactic column density is frozen at the Leiden/Argentine/Bonn (LAB) Galactic HI Survey (Kalberla et al., 2005) value of 1.36×10^{20} cm^{-2} in our fits. Two wide instrumental Au M edges are modeled with two *gabs* components at 2.3 and 3.08 keV following Tamura et al. (2015).

The contribution of the soft local X-ray background (including local hot bubble and galactic halo) is negligible in our fitting band ($1.95 - 6$ keV), while the contribution of the cosmic X-ray background (CXB) may still be significant. To account for the contribution of CXB we add a power-law component to the model. The normalization of the power-law model is left free, while the index is fixed to 1.41 in our fits. We check for possible systematic effects regarding the CXB in Section 4.2.1.

The atomic lines and their rest-frame energies included in our model are (see also Table 4.2): Al XIII (2.05 keV), Si XIV (2.01 keV, 2.37 keV, and 2.51 keV), Si XIII (2.18 keV, 2.29 keV, and 2.34 keV), S XV (2.46 keV, 2.88 keV, 3.03 keV), S XVI (2.62 keV), Ar XVII (triplet at 3.12 keV, 3.62 keV, 3.68 keV), Cl XVI (2.79 keV), Cl XVII (2.96 keV), Cl XVII (3.51 keV) K XVIII (triplet 3.47 keV, 3.49 kev and 3.51 keV), K XIX (3.71 keV), Ca XIX (complex at 3.86 keV, 3.90 keV, 4.58 keV), Ar XVIII (3.31 keV, 3.93 keV), Ca XX (4.10 keV), Cr XXIII (5.69 keV). After the first iteration the χ^2 improvement for the inclusion of each of these lines is determined, and lines that do not improve the fit by more than a $\Delta\chi^2$ of 2 are removed from the model (on a region-by-region basis).

It is crucial to determine the fluxes of S XV at 2.46 keV and S XVI at 2.62 keV accurately for temperature estimation, as this line ratio is a very sensitive temperature diagnostic, especially valuable for detecting the presence of cool gas. However, the band where S XV and S XVI are located, is crowded with strong Si XIV lines. We therefore tie the fluxes of Si XIV (2.01 keV: 2.37 keV: 2.51 keV) to each other with flux ratios of (21:3.5:1). We also tie S XV (2.46 keV : 2.88 keV) lines with a flux ratio of (9:1). These ratios are based on the theoretical predictions for the typical temperatures we measure.
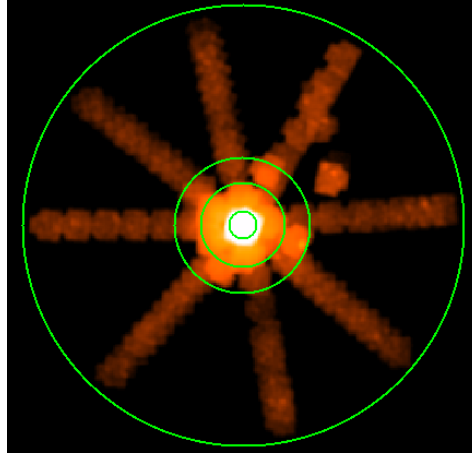
Figure 4.1: Countmap of all pointings used in the present analysis, with radial extraction regions shown at 8.3′, 25′, 40′ and 130′.

Ion	E	Ion	E
	keV		keV
Al XIII	2.05	Cl XVII	3.51
Si XIV	2.01, 2.37, 2.51	K XVIII	3.47, 3.49, 3.51
Si XIII	2.18, 2.29, 2.34	K XIX	3.71
S XV	2.46, 2.88, 3.03	Ca XIX	3.86, 3.90, 4.58
S XVI	2.62, 3.28	Ar XVIII	3.31, 3.93
Ar XVII	3.12, 3.62, 3.68	Ca XX	4.10
Cl XVI	2.79	Cr XXIII	5.69
Cl XVII	2.96		

Table 4.2: List of atomic lines and their rest-frame energies included in the model.

The observed fluxes of some of the strong atomic lines in our fitting band are given in Table 4.4.

To model the fluxes of the K XVIII, Cl XVII, and Ar XVII lines nearest to the 3.5 keV energy in question, we use temperature estimates indicated by other lines. The line ratios of S XV ($1s^12p^1 \rightarrow 1s^2$) at 2.46 keV to S XVI ($2p^1 \rightarrow 1s^1$) at 2.62 keV and Ca XIX ($1s^1$ $2p^1 \rightarrow 1s^2$) at 3.9 keV to Ca XX ($2p^1 \rightarrow 1s^1$) at 4.11 keV are excellent temperature probes – especially sensitive to the presence of cool gas (see Bulbul et al. (2014b) for discussion). The fluxes of lines from Cl XVII and Ar XVII at 3.51 keV and 3.62 keV are restricted by the other lines of the same ions detected at 2.96 keV and 3.12 keV respectively.

The emissivities of K XVIII, K XIX, Cl XVII, and Ar XVII lines are higher at the lower temperature ranges for each model, which are determined from the S XV to S XVI line ratios. We use factors of 0.1 and 3 over the *highest values within the allowed temperature ranges* for these fluxes as lower and upper bounds for the normalizations of the Gaussian lines as described in Bu14. The factor 3 gives a conservative allowance for variation of the relative elemental abundances between the S and K, Cl, and Ar ions.

4.2.1 Systematics

In addition to the atomic model uncertainties (which we account for by using conservatively wide intervals for the allowed fluxes of the atomic lines), the main source of systematic uncertainty regarding the models is the CXB power-law component. In order to estimate the effect of this uncertainty on the other model parameters we perform the following simulations using XSPEC's `fakeit` command. Starting from the best-fit model, a new power-law normalization is randomly drawn uniformly from the 1σ range of the originally measured normalization. This is repeated 1000 times, and a simulated spectrum is generated each time (with the input model only differing in power-law normalization). The simulated spectra are refit and from the resulting population the 68% intervals of the distribution for each free parameter are recorded. These are then added in quadrature to the statistical uncertainty from the best-fit model to the real data. The total (statistical and systematic) errors on the best-fit parameters are given in Table 4.4.

Region	Region detected in			
emitted from	0-2	2-4.5	4.5-8.3	>8.3
0-2	0.60	0.33	0.03	0.00
2-4.5	0.09	0.68	0.19	0.01
4.5-8.3	0.00	0.08	0.80	0.08
>8.3	0.00	0.01	0.15	0.78

Table 4.3: Percentage redistribution between the inner annuli due to the effects of PSF smearing, as described in Section 4.2.1. Numbers represent the fraction of photons that are emitted from one annulus, and detected in another.

Due to *Suzaku*'s relatively large PSF, some X-ray photons that originate from one particular region on the sky may be scattered elsewhere on the detector. Since the region

sizes we used in this work are similar or relatively large compared to the PSF size of the XIS mirrors, the effect is expected to be small. The effect of PSF spreading on the flux of the ∼3.5 keV line depends on its origin, and we therefore examine two scenarios. Firstly we consider the case where the flux of the line is distributed according to the broadband X-ray surface brightness as described by the higher resolution imaging of the *XMM Newton* PN observation of the Perseus cluster core (observation ID 0305780101). We use ray-tracing simulations of 2×10^6 photons performed through *xissim* (Serlemitsos et al., 2007) with our best-fit model and the PN surface brightness map as input, to determine the scattered photons per sub-region. Table 4.3 reports the results in terms of the fraction of photons that are emitted in one region and detected in the other. These results are consistent with the photon fractions reported in (Bautz et al., 2009) and (Bulbul et al., 2016b). The second scenario that we examine using the same methodology, is when the ∼3.5 keV line originates from dark matter decay and therefore follows a NFW profile. In this case, the redistribution fraction change only slightly from the ones in Table 4.3, at most by a few percent-points. The dependence on the details of the NFW assumed is even smaller. The net effect of the PSF spreading on the measured fluxes in each regions depends more strongly on the input (or true) distribution than do the redistribution fractions. It is as follows. For the regions 1a through 1c respectively, in the case that the line follows the broadband surface brighness, the measured flux in the line would be underestimated by ∼31%, overestimated by ∼8% and overestimated by ∼22%. In the case that the line flux follows the NFW distribution, the measurement would be underestimated by ∼8%, overestimated by ∼3% and overestimated by ∼2%. In Section 4.5 we will discuss the implications of this on our results, but since the origin of the line at this point is unclear, we will refrain from applying a correction for either scenario in what follows unless explicitly noted.

Model	Reg 1	Reg 2	Reg 3	Reg 4	Reg 2-4
Parameter	$(0'-8.3')$	$(8.3'-25')$	$(25'-40')$	$(40'-130')$	$(8.3'-130')$
kT_1 (keV)	3.09 ± 0.04	6.52 ± 0.11	6.10 ± 0.29	5.91 ± 0.50	4.64 ± 0.07
N_1 (10^{-2} cm^{-5})	$5.54^{+3.23}_{-1.33}$	3.69 ± 0.033	0.57 ± 0.016	0.09 ± 0.005	0.60 ± 0.007
kT_2 (keV)	5.78 ± 0.03	-	-	-	-
N_2 (cm^{-5})	0.54 ± 0.04	-	-	-	-
Power-Law Norm (10^{-4})	7.71 ± 0.65	4.62 ± 1.28	0.00 ± 0.40	0.88 ± 0.10	5.13 ± 0.17
Flux of the S XV	$2.71 \pm 0.05 \times 10^2$	5.60 ± 4.12	2.06 ± 1.85	0.72 ± 0.64	1.34 ± 0.85
Flux of the S XVI	$7.64 \pm 0.07 \times 10^2$	23.17 ± 3.45	3.14 ± 1.62	1.21 ± 0.45	5.10 ± 0.70
Flux of the Cl XVII	$0.22 \pm 0.04 \times 10^2$	-	-	-	-
Flux of the Ar XVIII	$2.07 \pm 0.04 \times 10^2$	7.35 ± 2.16	-	0.61 ± 0.27	2.11 ± 0.59
Flux of the Ca XIX	$1.77^{+0.34}_{-0.17} \times 10^2$	3.96 ± 4.56	1.14 ± 0.98	-	1.07 ± 0.55
Flux of the Ca XX	$1.43 \pm 0.03 \times 10^2$	4.7 ± 1.69	-	-	0.93 ± 0.39
χ^2 (dof)	2504.4 (2170)	2919.0 (3061)	3276.1 (3063)	3880.3 (3062)	3259.0 (3060)

Table 4.4: The best-fit parameters of the model. The fluxes of the S XV, S XVI,Cl XVII, Ar XVIII Ca XIX, and Ca XX lines are in the units of 10^{-6} pht cm^{-2} s^{-1}. Fields with a '-' indicate the absence of this component from the model. The χ^2 reported does not include a ∼3.5 keV model component.

Model Parameter	Reg 1a ($0'$–$2'$)	Reg 1b ($2'$–$4.5'$)	Reg 1c ($4.5'$–$8.3'$)
kT_1 (keV)	3.35 ± 0.11	4.85 ± 0.04	6.41 ± 0.22
N_1 (10^{-2} cm^{-5})	0.11 ± 0.03	0.12 ± 0.06	0.22 ± 0.01
kT_2 (keV)	5.72 ± 0.29	6.02 ± 0.24	-
N_2 (cm^{-5})	0.16 ± 0.04	0.20 ± 0.03	-
Power-Law Norm (10^{-4})	4.16 ± 0.51	1.77 ± 0.63	5.11 ± 0.16
Flux of the S XV	1.74 ± 0.07	1.44 ± 0.16	0.65 ± 0.16
Flux of the S XVI	4.39 ± 0.07	4.20 ± 0.07	1.99 ± 0.09
Flux of the Cl XVII	0.28 ± 0.06	-	-
Flux of the Ar XVIII	1.31 ± 0.13	1.19 ± 0.07	0.39 ± 0.11
Flux of the Ca XIX	1.14 ± 0.12	1.03 ± 0.04	0.39 ± 0.05
Flux of the Ca XX	0.71 ± 0.04	0.78 ± 0.05	0.48 ± 0.04
χ^2 (dof)	2317.3 (2168)	2450.8 (2168)	2401.7 (2168)

Table 4.5: Same as Table 4.4, but for the subregions of the core. The best-fit parameters of the model. The fluxes of the S XV, S XVI, Cl XVII, Ar XVIII Ca XIX, and Ca XX lines are in the units of 10^{-4} pht cm^{-2} s^{-1}. Fields with a '-' indicate the absence of this component from the model.

4.3   Results

4.3.1   Perseus Center

We initially extract source and background spectra from a circular region surrounding the cluster's center with a radius of $8.3'$ (we refer to this region as *Region 1*). The total filtered on-axis FI/BI exposure times are 1.0/0.67 Ms. There are 1.4×10^7 source counts in the background-subtracted FI spectrum and 1×10^7 in the BI spectrum

We model the 1.95 to 6 keV band with the continuum and lines as described in the previous section (Section 4.2). The best-fit values of the model are given in Table 4.4. The plasma temperature measured from the continuum (3.09 ± 0.04 keV) is in agreement with the plasma temperature estimated from the S XV to S XVI line flux ratio (3.13 keV) at a 1σ level. We stress again that the S line ratio is very sensitive to cool gas. The peak emissivity of the S XV line is at kT≈ 1 keV; thus, if any significant cool gas phase were present, the line ratio temperature would be biased toward it. This plasma temperature is also in good agreement with the temperatures measured from the *XMM-Newton* and *Chandra* observations of the Perseus cluster (Bulbul et al., 2014a,b).

Estimating the fluxes of detected lines is crucial for determining the flux around the 3.5 keV line. For a sanity check, we compare the intensities of the three lines from ions (i.e., Si XIV, Ar XVII, Cl XVII) detected significantly in the fitting band with the estimates based on the observed S XV / S XVI line ratio. Si XIV line at 2 keV is detected significantly with a flux of $(1.24 \pm 0.01) \times 10^{-3}$ pht cm^{-2} s^{-1}. The predicted Si XIV flux from a
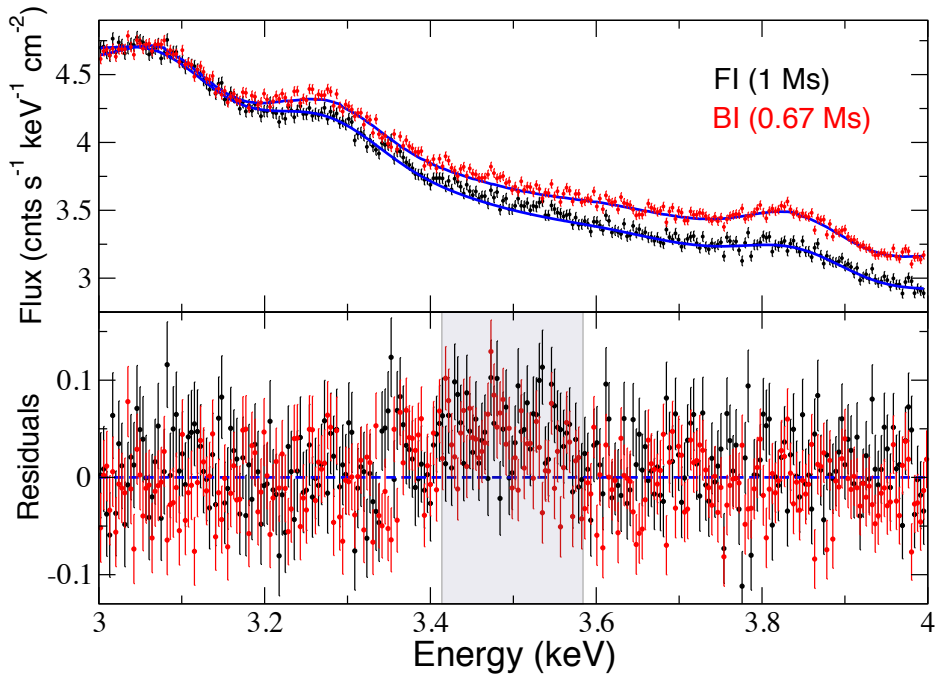
Figure 4.2: Observed *Suzaku* FI and BI Spectrum of the Perseus cluster core (Region 1). The residuals around 3.5 keV (redshifted) are visible clearly (shaded area in the bottom panel). The model shown in the figure includes contributions from the nearby K XVIII, Cl XVII, and Ar XVII lines. The 3.5 keV rest-frame energy corresponds to 3.49 keV in this plot.

~ 3.1 keV plasma is 1.38×10^{-3} pht cm^{-2} s^{-1} using AtomDB, indicating that S and Si have relative abundances of 0.9 ± 0.01 with respect to the Asplund et al. (2009) solar abundances. The measured Ar XVII at 3.12 keV is $2.07 \pm 0.41 \times 10^{-4}$ pht cm^{-2} s^{-1}, while the flux estimated using AtomDB is 1.30×10^{-4} pht cm^{-2} s^{-1}. The implied abundance ratio of Ar to S is $1.6^{+0.31}_{-0.32}$ with respect to the solar abundance. Unlike in the stacked *XMM-Newton* observations of a large sample of clusters and the *XMM-Newton* and *Chandra* observations of the Perseus cluster (from Bo14 and Bu14), we detect a very faint Cl Ly-α line at 2.96 keV in the *Suzaku* spectrum of the Perseus core. The measured $(2.20 \pm 0.4) \times 10^{-5}$ pht cm^{-2} s^{-1}) and estimated (1.93×10^{-5} pht cm^{-2} s^{-1}) Cl Ly-α fluxes indicate that the abundance ratio of Cl to S is $\sim 1.1^{+0.25}_{-0.18}$ with respect to the solar abundance. The best-fit flux of the K XIX line at 3.70 keV is $6.0 \pm 4.0 \times 10^{-6}$ pht cm^{-2} s^{-1}. The predicted flux of the line (3.4×10^{-6} pht cm^{-2} s^{-1}) shows that the abundance ratio of K to S is 1.8 ± 1.2 with respect to solar.

Parameter	Reg 1	Reg 1a	Reg 1b	Reg 1c	Reg 2	Reg 3	Reg 4	Reg 2-4
kT based on S (keV)	3.13 ± 0.03	2.97 ± 0.06	3.18 ± 0.17	3.25 ± 0.36	$3.74^{+1.23}_{-1.69}$	$2.37^{+0.90}_{-2.37}$	$2.47^{+0.90}_{-1.56}$	$3.60^{+1.00}_{-1.34}$
kT based on Ca (keV)	4.02 ± 0.29	3.65 ± 0.16	3.92 ± 0.11	4.85 ± 0.36	$4.77^{+2.32}_{-4.77}$	–	–	$4.14^{+1.11}_{-1.36}$
Flux of Cl XVII at 2.96 keV	1932.9	1085.6	1068.9	510.8	62.2	6.79	2.70	13.5
Flux of Cl XVII at 3.51 keV	295.3	164.8	163.6	78.4	9.69	1.00	0.40	2.10
Flux of K XVIII at 3.47 keV	227.8	138.3	122.6	56.4	5.32	1.13	0.43	1.25
Flux of K XVIII at 3.49 keV	112.4	68.2	60.5	27.9	2.65	0.57	0.22	0.62
Flux of K XVIII at 3.51 keV	471.1	280.1	255.3	118.5	11.8	2.13	0.82	2.73
Flux of Ar DR XVII at 3.62 keV	56.9	38.1	29.8	13.1	0.97	0.50	0.17	0.24

Table 4.6: Estimated fluxes of the Cl XVII, K XVIII, Ar DR XVII lines are in the units of 10^{-8} pht cm^{-2} s^{-1} from AtomDB. The fluxes (and not the temperature) in this table are dependent on the assumed solar abundance (Asplund et al., 2009), and are employed in the fits by setting the upper and lower allowed limits for the fitting procedure to 3 times and 0.1 times this flux, respectively. Temperature ranges implied by uncertainty of the measured lines are shown for illustrative purposes.

To estimate the flux of the 3.5 keV line, we model the possibly contaminating K XVIII (3.47 keV: 3.49 keV: 3.51 keV), and Ar XVII (3.12 keV: 3.62 keV: 3.68 keV) lines with the ratios of (1: 0.5: 2.3) and (1: 1/23: 1/9). The line ratios are estimated for the temperature indicated by the observed S XVI/XV line ratio. We also include the Cl Ly-β line at 3.51 keV with a flux tied to $0.15 \times$ that of the the flux of the Cl Ly-α line at 2.96 keV in our fits. The measured best-fit K XVIII at 3.51 keV is 1.05×10^{-6} pht cm^{-2} s^{-1}, also in agreement with the AtomDB predictions. We note that the total flux of the K XVIII triplet between 3.47–3.51 keV is estimated at 8.11×10^{-6} pht cm^{-2} s^{-1} from AtomDB (Table 4.6), but that we allowed the K XVIII flux to be up to 2.5×10^{-5} pht cm^{-2} s^{-1} in our fits. Additionally, we provide the flux estimates of the detected lines based on Anders & Grevesse (1989) solar abundance for comparison in Appendix 4.6 as Table 4.9. In summary, the abundance ratios of detected lines implied by our measurements and AtomDB range between 1–1.7 for the strongly detected lines (including K XIX) in our fitting band, well within the assumed interval of a factor $0.1-3$ regardless of assumed solar abundance sets.

Examining the 3–4 keV band in the simultaneous fits of the FI and BI observations, we find excess emission around 3.5 keV (rest energy). The residuals around 3.5 keV

(which corresponds to a redshifted energy of 3.49 keV) are shown in Figure 4.2. If we add a redshifted Gaussian line with energy as a free parameter, the best-fit energy of the line becomes $3.54 \pm 0.01(0.02)$ keV with a flux of $2.79^{+0.35}_{-0.35} \left(^{+0.59}_{-0.57}\right) \times 10^{-5}$ pht cm^{-2} s^{-1}. The fit improves by $\Delta\chi^2$ of 62.6 for 2 degrees-of-freedom (d.o.f.), corresponding to a $\sim 7.6\sigma$ detection.

To investigate the radial behavior of the signal in the core, we divided the core into three spectral extraction regions: circular regions with radii of $0-2'$, $2'-4.5'$, and $4.5'-8.3'$. The best-fit model parameters of the *line-free apec* model is given in Table 4.6. Following the same fitting procedure described above, we find that the best-fit energy and flux of the line in the innermost $0-2'$ region are 3.51 ± 0.02 (0.03) keV and $9.28^{+2.62}_{-2.67} \left(^{+4.41}_{-4.33}\right) \times 10^{-6}$ pht cm^{-2} s^{-1}. The change in the $\Delta\chi^2$ is 12.1 for the extra 2 d.o.f. In the intermediate $2'-4.5'$ region, the line energy is detected at 3.55 ± 0.02 (0.03) keV with a flux of $1.67^{+0.29}_{-0.30} \left(^{+0.52}_{-0.48}\right) \times 10^{-5}$ pht cm^{-2} s^{-1} ($\Delta\chi^2$=23.3 with additional two d.o.f.). The line is also detected in the last $4.5'-8.3'$ region at an energy of 3.58 ± 0.02 (0.03) keV with a flux of $1.61^{+0.32}_{-0.34} \left(^{+0.51}_{-0.49}\right) \times 10^{-5}$ pht cm^{-2} s^{-1} ($\Delta\chi^2$=16.5 for additional 2 d.o.f.). The radial profile of this signal has also been studied by Urban et al. (2015) in two spectral regions. Our results are in broad agreement once the sizes and shapes of the spectral extraction regions are taken into account, as we will discuss in Sections 4.4.

We then fit these spectra with a Gaussian model with the line energy fixed at 3.54 keV, which is the best-fit value detected in the 0–$8.3'$ region. We find that the flux of the line becomes 6.54 ± 2.62 (4.3) $\times 10^{-6}$ pht cm^{-2} s^{-1} in the innermost 0–$2'$ region, with a change in the $\Delta\chi^2$=6.23 for an additional 1 d.o.f. The flux remains the same ($1.67^{+0.31}_{-0.28} \left(^{+0.49}_{-0.47}\right) \times 10^{-5}$ pht cm^{-2} s^{-1}) within the intermediate $2'-4.5'$, while the change in the χ^2 becomes 25.9 for an additional 1 d.o.f. In the last region the line is detected with a flux of $1.27^{+0.29}_{-0.34} \left(^{+0.41}_{-0.47}\right) \times 10^{-5}$ pht cm^{-2} s^{-1} with a $\Delta\chi^2$ of 10.8 for additional 1 d.o.f. The $\sim$3.5 keV line is detected with a confidence of $> 3\sigma$ in all three regions within the core of the Perseus cluster. Table 4.7 summarizes the above results.

4.3.2 Perseus Outskirts

A total of 100 *Suzaku* observations of the Perseus cluster with the nominal pointing further than $14'$ from the cluster center were retrieved from the archives, for a total cleaned FI/BI exposure of 2.72/1.36 Ms and background-subtracted source counts of 6.3×10^5 and 4.3×10^5. We divide this data into three annular spectral extraction regions. The first annulus (called 'Region 2') starts at $8.3'$, where the central analysis of Section 4.3.1 ends, and extends to $25'$. 'Region 3' is an annular extraction region with inner radius $25'$, and outer radius $40'$. While the outermost annulus does not have an outer radius imposed, the outermost pointing is centered on $117'$ from the Perseus cluster core, so that all data used in this study comes from within $130'$. This is 'Region 4' in Table 4.1. The same table contains the sizes of all regions in angular and physical scales. A visual representation is given in Figure 4.1. As will become apparent in later sections, it is also useful to create a single stacked dataset of all these off-center observations in order to obtain better statistics. This is referred to as 'Region 2-4' in Table 4.1.

To further obtain maximum photon statistics, in the results reported here for the off-center data, no point sources were removed. A parallel analysis of a version of the dataset

Region		Restframe E	Flux	$\Delta\chi^2$	χ^2 (dof)
		keV	10^{-5} ph s^{-1} cm^{-2}		
Region 1	(0′–8.3′)	$3.54 \pm 0.01(0.02)$	$2.79^{+0.35}_{-0.35}$ $(^{+0.59}_{-0.57})$	62.6	2441.7 (2168)
Region 1a	(0′–2′)	$3.51 \pm 0.02\ (0.03)$	$0.93^{+0.26}_{-0.27}$ $(^{+0.44}_{-0.43})$	12.1	2317.3 (2168)
		3.54	$0.65 \pm 0.26\ (0.43)$	6.23	
Region 1b	(2′–4.5′)	$3.5 \pm 0.02\ (0.03)$	$1.67^{+0.29}_{-0.30}$ $(^{+0.52}_{-0.48})$	23.3	2450.8 (2168)
		3.54	$1.67^{+0.31}_{-0.28}$ $(^{+0.49}_{-0.47})$	25.9	
Region 1c	(4.5′–8.3′)	$3.58 \pm 0.02\ (0.03)$	$1.61^{+0.32}_{-0.34}$ $(^{+0.51}_{-0.49})$	16.5	2401.7 (2168)
		3.54	$1.27^{+0.29}_{-0.34}$ $(^{+0.41}_{-0.47})$	10.8	

Table 4.7: Best-fit values for detected excess emission around 3.5 keV (rest frame) for the core regions. Also included is the best-fit flux in the case that the energy is fixed to the best fit from Region 1 (ie, 1 additional degree-of-freedom instead of 2). Total χ^2 values are shown before the $\sim$3.5 keV line is added to the model.

with the point sources removed as detected by Urban et al. (2015), did not reveal large qualitative differences. Since we have not detected the 3.5 keV line in the outskirts, we only show the higher-statistics dataset that did not mask the point sources.

The spectral modeling of the off-center is performed as described in Section 4.2, unless noted otherwise. The energy band used for fitting the off-center observations is reduced to 1.95 – 5.7 to avoid a strong negative residual in the XIS 1 spectra. This is likely associated with an imperfect background subtraction of the instrumental Mn-Kα line (see also Sekiya et al. (2015)). In addition to the tied line ratios mentioned in Section 4.2, the off-center analysis also tied the flux of the S XV line at 3.03 to S XV at 2.46 with the theoretical ratio (1:40).

As in the analysis of the central region, we utilize the observed line ratios of S and Ca where available to determine the maximum contribution of the Ar and K lines near 3.5 keV. The measured line ratios in most regions imply a second thermal component at somewhat lower temperature, but none of the broadband fits prefer a model with two plasma continuum components. As we noted in the previous section, this is not entirely unexpected for a multi-temperature environment as the broad-band fit is mostly sensitive to high temperatures and the power-law normalization of the CXB component, while the emissivity of the S lines peaks at low temperatures and thereby causes the S line ratios to be sensitive to the low temperature components. Therefore we modify the previously obtained models by setting the maximum allowed range for the line normalizations for the Ar, K and Cl lines around 3.5 keV to 3$\times$ the maximum shown in Table 4.6 indicated by the S and Ca ratios, and refitting.

We obtained acceptable fits to the data of all off-center regions with a reduced-χ^2 of around 1, except for Region 4 (the outer region), where $\bar{\chi}^2 \sim 1.25$. This is most likely due to large radial extent of this region of the cluster that is stacked, making the single model fit insufficient. The results of the fits of the off-center regions are shown in table 4.4.

Plasma temperatures and normalizations are generally consistent with the measurements performed by Urban et al. (2014). However, the relatively low best-fit temperature for Region 2-4 is mainly caused by a preference for a relatively high normalization of the powerlaw. Fixing the powerlaw normalization to a lower value more in line with the outer regions, brings the temperature of the continuum component up again to above 6 keV. However, the fit with the fixed powerlaw normalization provides a worse fit by a $\Delta\chi^2$ of about 15. The fit otherwise shows no qualitative differences, and therefore we continue to employ the better fitting model (with fitted powerlaw normalization). As mentioned above, the best-fit continuum temperature is not used for the estimates of line strengths, rather the line ratios of well-measured S- and Ca- lines are.

With these final models in hand, we look for the presence of excess emission by adding a redshifted Guassian line component to the model at different restframe energies around ∼3.5 keV while leaving the normalization free. The plasma temperature and the normalizations of all other model components are left free in these fits. There is not a single region of the Perseus cluster outskirts for which we see significant positive line-like residuals anywhere in the vicinity of 3.5 keV (restframe). Note that none of the Ar, Cl or K lines near 3.5 keV are detected in these datasets either (i.e., contributions from these lines were allowed in the earlier fitting process described in Section 4.2, but were not required by the fits).

Not having found significant line-like residuals around 3.5 keV, we compute the flux limit for such a line for each off-center spectrum in the following way. Starting with the best-fit model we add one redshifted Gaussian at rest-frame 3.54 keV (the nominal detected value in Region 1), and vary its normalization until the new $\Delta\chi^2$ is higher by 4.0, which corresponds to a 2σ limit for a single added degree of freedom. The normalizations of all model components are left free, as is the plasma temperature. The obtained flux limits will be discussed in Section 4.4.1.

4.4 Discussion

4.4.1 Line Flux and Dark Matter Profiles

We compare our results to the behaviour expected from dark matter decay in this Section. For a first look, Figure 4.3 shows the radial dependence of the surface brightness of the ∼3.5 keV signal. The results from this work and those obtained by Bo14 are shown in red and blue respectively. Downward pointing arrows indicate the 2σ upper limits from the analysis of the outskirts. Expected dark matter decay signal strength for different NFW dark matter distributions (see below) is depicted by the set of black curves. It is important to note that the normalization of the expected decay signal depends on the dark matter particle lifetime and is therefore completely degenerate with the absolute mass scale of the NFW profiles. The figure shows arbitrary individual normalizations chosen to facilitate visual comparison in this case.

Additionally, Figure 4.3 shows the detected surface brightness of the Fe XXV K-α line at 6.7 keV from all our *Suzaku* regions with the open purple squares as an indicative visual example of possible emission line-like behaviour. This behaviour is typically described by a double-β profile, which is shown as the purple dashed line with parameters from Churazov et al. (2003) albeit with arbitrary overall normalization in order to roughly line

up with the Fe measurements. The measurements of the Fe lines and the double-β profile are compatible with each other while showing quite a contrast with both the ~3.5 keV measurements and the DM decay-like profiles.

It is important to note that the radial behaviour as shown in this figure does not accurately reflect the effects of the varying pointings nor of the varying field-of-view shapes and sizes that are averaged in each datapoint, which will be handled in detail in the following.

Are our non-detections in the Perseus outskirts inconsistent with the dark matter decay origin of the 3.5 keV line? In order to determine this, we compare the measurements to the predictions in the most direct way, by computing the effective dark matter mass in the field of view for each dataset. For a given field of view, this quantity depends only on the dark matter profile assumed, and is directly related to the expected signal by the particle lifetime. It is computed as follows. For the off-center *Suzaku* data, where the different observations have been separated into concentric annuli, we divide the available pixels for a particular observation and extraction region into 25 spatial bins. Then we compute the dark matter column density at the center of each of those bins, given an NFW model, before converting to mass inside the effective field-of-view using the effective sky area. The exposure weighted average mass is then obtained for each region. For the on-axis observations, the extraction regions are of a more convenient shape, allowing us to simply compute the enclosed mass within a certain projected radius for a given NFW profile.

We compare the results of this work with the results obtained in Bo14, Bu14 and Urban et al. (2015). The effective dark matter mass for these observations is obtained in a similar fashion as described above. Figure 4.4 shows the flux (detections and upper limits) of the ~3.5 keV line as a function of dark matter mass in the field of view for a bracket of literature mass profiles. The red boxes marked *Suzaku* are the detections and the upper limits from this work (upper limits defined as $\Delta\chi^2$ of 4.0, or 2σ for 1 degrees of freedom). Lines of constant dark matter particle lifetime are shown as diagonal black lines. Each box represents a different spectral extraction region, for which the DM mass in that particular field of view has been computed by the method described above. This is done for three literature profiles for the Perseus cluster (e.g., Simionescu et al., 2012a; Sánchez-Conde et al., 2011; Storm et al., 2013). Storm et al. (2013) makes use of the measurement of M_{500} of Chen et al. (2007), determines NFW parameters through scaling relations and finally corrects for the gas fraction to get to the dark matter distribution. Sánchez-Conde et al. (2011) employs the measurement of M_{200} from Reiprich & Boehringer (2002) and the scaling relation from Duffy et al. (2008). Lastly, Simionescu et al. (2012a) derives an NFW profile for the total mass distribution directly by fitting to piecewise annular X-ray data. The latter two do not quote dark matter only profiles, so we take the baryon fraction into account using the functional form $f_{gas} \sim r^{0.43}$ (Mantz et al., 2014) calibrated to the reported gas fraction of Perseus by Simionescu et al. (2012a). Included in the bracket of computed enclosed dark matter mass are the statistical 1σ uncertainties reported in those works, although the scatter between the different profiles is larger than the statistical errors on each. In all computations of the enclosed dark matter mass, the different background cosmologies and differences in the definition of the NFW used in those studies have been take into account.

Here we take the effects of PSF smearing described in Section 4.2.1 into account in the following way. As was noted, this effect is only relevant for the smaller regions 1a
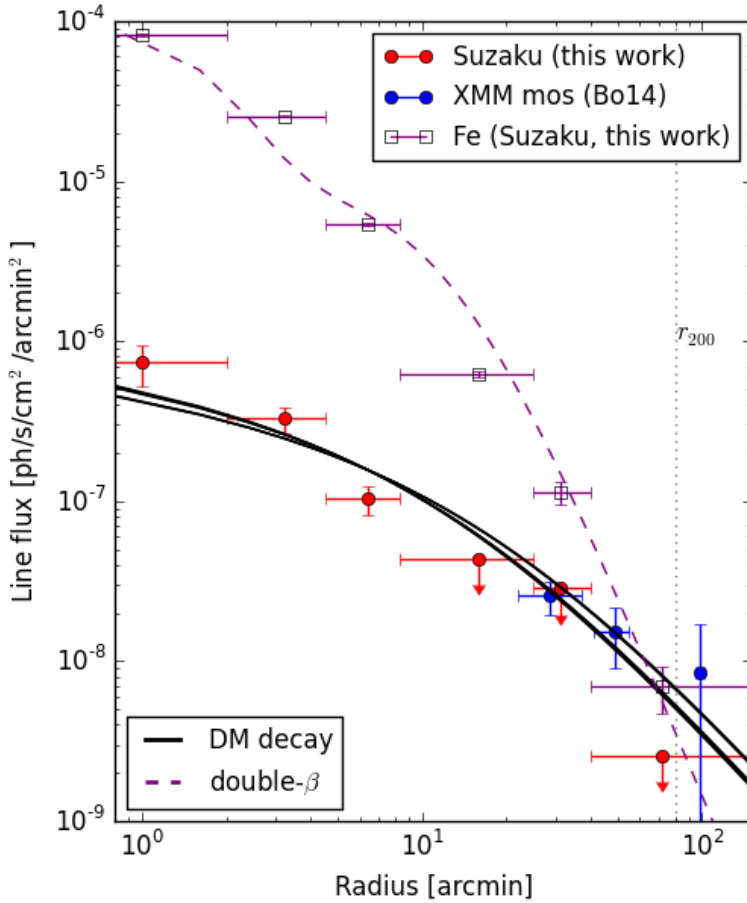
Figure 4.3: Radial profile of the measured ∼3.5 keV surface brightness (1σ error bars) and upper 2σ limits obtained from our Suzaku measurements (red), compared to the measurements of Bo14 using *XMM-Newton* (blue). Black curves indicate the expected surface brightness profiles of a dark matter decay signal based on several NFW literature profiles for the dark matter distribution (see text). The normalization of these predictions is degenerate with the particle lifetime, and the shown curves have an arbitrary normalization assigned for visual purposes in this figure. Horizontal error bars show the bracket of radial extraction regions per bin, while the central value is the dark matter column density-weighted average radius for that radial bin. For comparison, the purple empty squares indicate measurements of the Fe xxv K-α emission at 6.7 keV in our data and the purple dashed curve shows a surface brightness profile based on the double-β profile measured by Churazov et al. (2003) but with arbitrary normalization. Note that none of the lines shown in this figure are fitted.
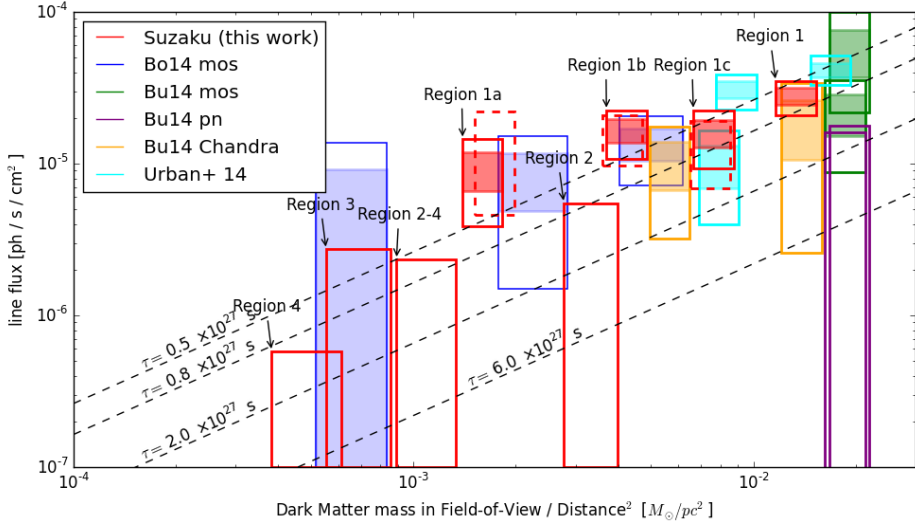
Figure 4.4: The 3.5 keV flux as a function of the dark matter mass in the field of view. Measured by *Suzaku* in the red boxes (this work), by *XMM-Newton* MOS from Bo14 in blue and from Bu14 in green, by *XMM-Newton* PN in purple (Bu14), by *Chandra* in orange (Bu14). Also shown in cyan are the *Suzaku* measurements of Urban et al. (2015) with from left to right their 'confining', 'core' and full extraction regions (see text). Filled boxes indicate 1σ flux measurements, open boxes the 2σ interval. Boxes without a filled part and touching the x-axis indicate upper limits (2σ for this work, reported 90% for Bu14 pn), ie., Bu14 pn, and Regions '2', '3', '4' and '2-4'. The dashed red boxes indicate 2σ intervals of the *Suzaku* core subregions that have been corrected for PSF scattering using an alternative scenario for its estimation (see Sections 4.2.1 and 4.5). The width of the boxes is given by the bracket of different literature NFW profiles (see text). Lines of constant dark matter particle lifetime are the black lines with decay rates given in the annotation. NB: this study does not constrain the value of τ as this requires and absolute mass scale to be established; the values shown are for indicative purposes. The study by Boyarsky et al. (2015) compares different objects to this end, and uses a broader mass bracket for the Perseus cluster due to the inclusion of additional different probes of the cluster mass, extending the brackets out to longer lifetimes of order $\tau \sim 6 \times 10^{27}$ (see Section 4.4.1 for discussion).

through 1c, and it is dependent on the origin of the $\sim$3.5 keV line. In Figure 4.4, we compare the measured flux to the expected flux for a dark matter decay scenario, and we therefore apply the estimated effects of this scenario to the boxes for Regions 1a through 1c (we repeat for convenience; -8%, +3%, +2% respectively). For completeness we also show the corrections for the scenario when the $\sim$3.5 keV line follows the broadband X-ray surface brightness (as described in Section 4.2.1, -31%, +8%, +22%) as the dashed open red boxes. In both cases, this systematic effect was also added in quadrature to the error estimate to account for the uncertainty on this effect itself. Qualitatively, our conclusion is independent of the approach to PSF smearing used.

Not all data in Figure 4.4 is statistically independent. Regarding the current work (red boxes), 'Region 2-4' is a compound of 'Region 2', 'Region 3' and 'Region 4'. Regions 1a–c are subdivisions of 'Region 1'. Bu14 reported 2 measurements for each of the mos (green boxes) and pn detectors (purple boxes), the difference being the excision of the central $1'$ of the Perseus cluster (the data with the core excluded is the datapoint with the lower effective dark matter mass). Their *Chandra* measurements (yellow boxes) refer to the ACIS-S and ACIS-I chips of which the latter has the larger field-of-view and therefore higher effective dark matter mass. The 3 measurements shown of Urban et al. (2015) (cyan boxes), from right to left (higher to lower effective dark matter mass), refers to their full extraction region (full *Suzaku* field-of-view on-center), the core of the Perseus cluster (inner $6'$) and the 'confining' region (full field-of-view excluding the $6'$ core). In addition, the Urban et al. (2015) study is based on the same archival data as our 'Region 1' (and its sub-divided annuli). The Bo14 and Bu14 mos data from *XMM-Newton* are in fact from different independent pointings.

Our results as shown in Figure 4.4 indicate that the measurements and upper limits obtained with *Suzaku* in this work are internally mostly consistent with a decaying dark matter interpretation and with previous measurements. However, the non-detection in the outer-most region ('Region 4') is somewhat at odds with the fluxes of the measurements of the inner $2'$ ('Region 1a') and the annulus between $2'$ and $4.5'$ ('Region 1b'). Here we note that 'Region 4' has the worst fit quality of all off-center datasets at a reduced-χ^2 of $\sim$1.25 and the upper limit may be affected by this. In addition, the limit from Region 2 is marginally inconsistent with the detection in 'Region 1b'.

The very core of the Perseus cluster exhibiting relatively high $\sim$3.5 keV flux as reported in previous works is confirmed in our *Suzaku* data, but the inconsistency is less than 3σ even in the most extreme case. In addition, this enhanced flux is confined to a region smaller than $\sim$100 kpc (or $\sim$4.5$'$), a large fraction of which is occupied by the brightest cluster galaxy NGC 1275, and which is well inside the cool-core. This may influence both the spectral modeling and the dark matter distribution. Lastly, relaxing our conservative bounds (defined as $\Delta\chi^2$ of 4.0 for a fixed line energy) on the non-detections will alleviate the above inconsistencies.

The NFW profiles implemented in our calculations are taken from the literature as reported, all of which are based on X-ray measurements. Boyarsky et al. (2015) uses additional literature profiles obtained by different methods for the comparison between different objects, whereas this work is concerned with the internal behaviour of the signal within the Perseus cluster only. Extending the mass bracket to include all of the profiles used in Boyarsky et al. (2015) (not shown), $\tau = 6 \times 10^{27}$ s becomes consistent with almost all measurements. We stress again that absolute mass calibration is degenerate with dark

matter particle lifetime τ and that this work therefore does not constrain the latter.

4.4.2 Discussion of Perseus' Morphological and Dynamical State

The use of an NFW profile for the dark matter distribution of the Perseus cluster is justi-fied, as the cluster is reported to be a relatively relaxed cluster with a regular morphology and a moderately strong cool core (Simionescu et al., 2012a,b). These studies find that even if the assumptions of spherical symmetry and hydrostatic equilibrium are relaxed to account for some evidence of gas clumping (Simionescu et al., 2012a), their results remain consistent. In addition, the in- or exclusion of data from additional instruments, nor a change to a generalized NFW profile influence those results. Simionescu et al. (2012b) do report evidence of a past minor merger, indicated by a spiral-pattern of en-hanced surface brightness across the extent of the Perseus cluster in *Suzaku* data due to gas sloshing. The infall trajectory has been determined as east-west, although the inclina-tion is ill-constrained other than excluding edge-on. The initial NFW profile determined by Simionescu et al. (2012a) was based on observations of the North-West-arm of the *Suzaku* survey of the Perseus cluster. This arm does not exhibit any evidence of this mi-nor merger, so it is safe to conclude that for the current work it is not required to allow for any additional uncertainty in the mass profile of the Perseus cluster to account for dynamical disturbance, or irregular morphology.

4.4.3 Literature Comparison

The data of the Perseus core from the *Suzaku* archives employed in this work was also used by Urban et al. (2015) and Tamura et al. (2015). These works contain contradictory results, with Tamura et al. (2015) not reporting any excess flux around ∼3.5 keV. Our results agree with the work of Urban et al. (2015) regarding the Perseus cluster. Although our extraction regions and the spectral modeling are different, the ∼3.5 keV line sur-face brightness is consistent once the different spectral extraction regions are taken into account (as can be seen in Figure 4.4).

The work by Tamura et al. (2015) is unable to detect the putative feature at ∼3.5 keV in the same data as employed in the present work and by Urban et al. (2015) even though we employ the same calibration modifications (see Section 4.2) as Tamura et al. (2015). The authors claim that the ∼3.5 keV line detection could be an artifact of the degeneracy between the atomic lines and the continuum during fitting. They illustrate their claim with an example (in their section 4.2 and figure 14), where they fit the data between 3 – 4.2 keV with a model consisting of the plasma continuum and nine additional emission lines. Removing one of the lines from this model reveals a positive line-like residual, by design. There are a number of issues with this particular approach. Firstly, their fitting band is too narrow to determine the continuum level accurately, and in addition, they cover their entire energy range with extra gaussian lines, practically guaranteeing complete degeneracy between line fluxes and continuum level given the large resolution of XIS detectors. Secondly, the lines that are added are given fluxes that are unphysically high, namely 0.2 times the 3.1 keV Ar line, whereas our Table 6 shows that that these lines are expected to be about 10 times lower (0.03 – 0.04 times the 3.1 keV Ar flux) than that. These fluxes were not allowed to vary and forced to be overestimated in their

fit. This forces their continuum level to be underestimated, again guaranteeing that the removal of one gaussian model component reveals a line-like residual. A possible way to test this would be to compare the plasma temperature estimates, however, the plasma temperatures are not provided in the relevant section.

Additionally, the line modeling in Tamura et al. (2015) is less exhaustive than in our work (their 9 atomic lines compared to our 29). The limited number of lines used in their analysis leads to a large reduced chi-square value of 1.72 (compared to our 1.1). Indeed, most of the line emission does not get modeled properly and leads to residuals that are larger than the putative feature we detected in the fitting band. We reiterate that the putative feature is only a 1% flux feature over the continuum and that the continuum should be modeled at that level or better to be able to detect the line. We agree that the quality of the spectral modeling is essential to our work, and that at CCD resolution one has to be very careful of the interplay between atomic lines and the continuum. Our modeling procedure is as thorough as it is, taking the widest possible energy range to help determine the continuum level, providing physically motivated modeling of the atomic lines, and cross-checking the best fit line fluxes with atomic data.

4.5   Conclusion

We have studied all available data from the *Suzaku* telescope of the Perseus cluster out to almost $1.5r_{200}$ with the aim to investigate the radial behavior of the still unidentified line feature around 3.5 keV that was first reported in Bu14 and Bo14. We have studied the possibility that the detected 3.5 keV feature in the center of the Perseus cluster is due to atomic emission from highly-ionized nearby Ar XVII, Cl Ly-β, and K XVIII lines in the spectral neighborhood. We detect, for the first time, Cl Ly-α line at 2.96 keV in clusters of galaxies, whose flux is used to calculate the flux contribution of Cl Ly-β line at 3.5 keV. Using measurements of various detected strong emission lines in other energy bands of the spectrum to estimate the plasma temperature and allowing for a conservatively large range of elemental abundances, we find that the 3.5 keV flux is in excess of what is allowed for atomic line emission. We report a detection of this line feature from the central observations of the Perseus cluster with a measured flux in agreement with the previously reported detection (Urban et al., 2015).

The *Suzaku* observations of the cluster's outskirts do not exhibit an excess of flux around 3.5 keV, nor in radially separated annular regions. The upper limits provided by the co-added outskirts observations are consistent with the dark matter decay interpretation for the origin of the signal from the Perseus cluster. Of course, our results are also consistent with some unknown astrophysical line originating predominantly in the dense gas of the Perseus core.

Considering the current body of work, it is not presently possible to prove conclusively the origin of the 3.5 keV line as sourced by any one process. The measurements in this study indicate that cluster outskirts or other low-density environments are promising targets in terms of constraining power for future observational work provided the exposure reaches deep enough. The most likely immediate-future gain is through employing next-generation micro-calorimeters on board the planned *Micro-X* (Figueroa-Feliciano et al., 2015) mission, or on board *Hitomi* (Kitayama et al., 2014) if the satellite or any data

thereof can be salvaged. These instruments have the energy resolution required to improve the spectral modeling, in particular with regards to the measurements of the various line emission. Alternative methodologies relying on different observables to distinguish dark matter decay from astrophysical or instrumental effects also offer promising possibilities. Zandanel et al. (2015) for example suggests that the upcoming eROSITA survey (Merloni et al., 2012) will be able to distinguish dark matter decay by its behavior in an all-sky angular correlation analysis. Micro-calorimeters may also be able to detect the velocity shift and velocity broadening of X-ray spectral lines, which behave differently for dark matter decay or plasma emission due to the difference in dynamics between dark matter and gas, as described by Speckhard et al. (2016).

4.6   Appendix - Details of the Spectral Fits of Perseus with *Suzaku*

This appendix shows the additional details and figures of the fits for all of the *Suzaku* regions used in this work. Table 4.5 shows the best-fit parameters of the subregions 1a through 1c, while Figure 4.5 indicates graphically the best-fit gaussian line components for the best fit of Region 1.

Figures 4.6 and 4.7 show the spectra and residuals for all outskirt regions described in the text, being Regions 2, 3, 4, and 2-4.
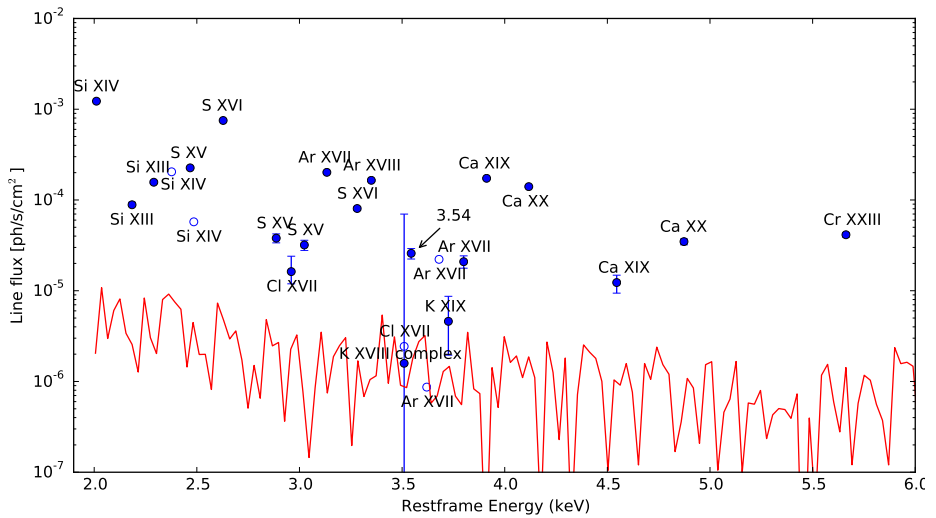
Figure 4.5: The gaussian line components of the best-fit model for Region 1, in units of ph s^{-1} cm^{-2}. Open circles indicate that the line flux was tied to another line in the fit. The red line indicates the residual level as the absolute value of the residuals in bins of 30 eV. Error bars are 1σ obtained with the `error` command in XSPEC. Note that the two lines at $\sim$3.51 keV are the Cl XVII line which is tied to the line of the same ion at 2.96 keV, and the K XVIII complex whose maximum allowed flux is actually much lower than the formal error bar indicates (the maximum allowed flux is roughly 2.4 pht cm^{-2} s^{-1} as indicated by Tables 4.6 and 4.9 and in Section 4.2).
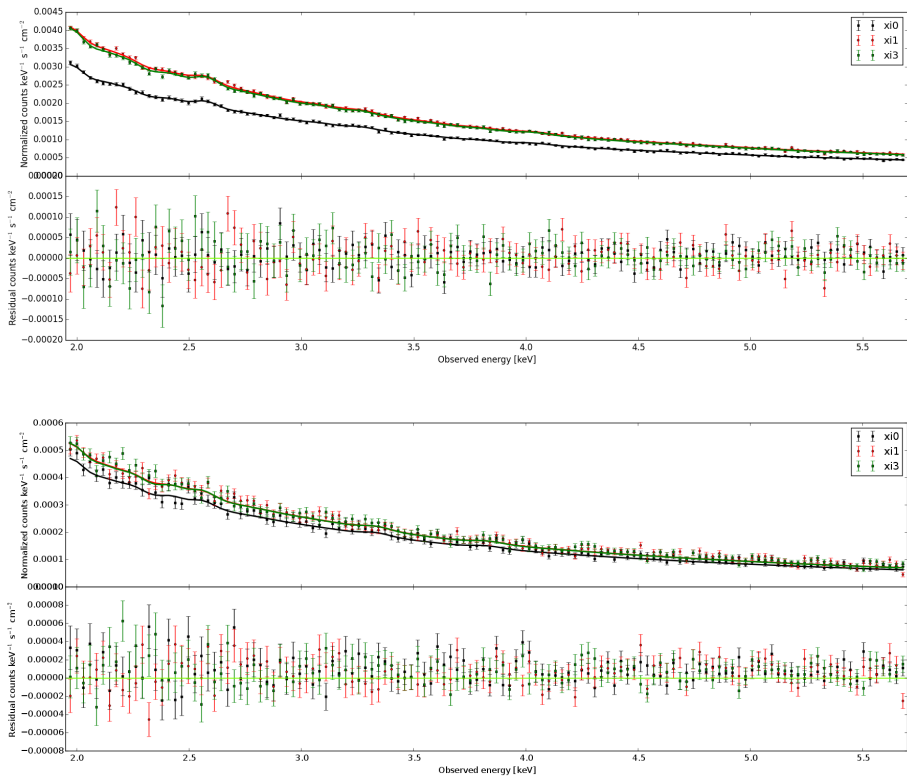
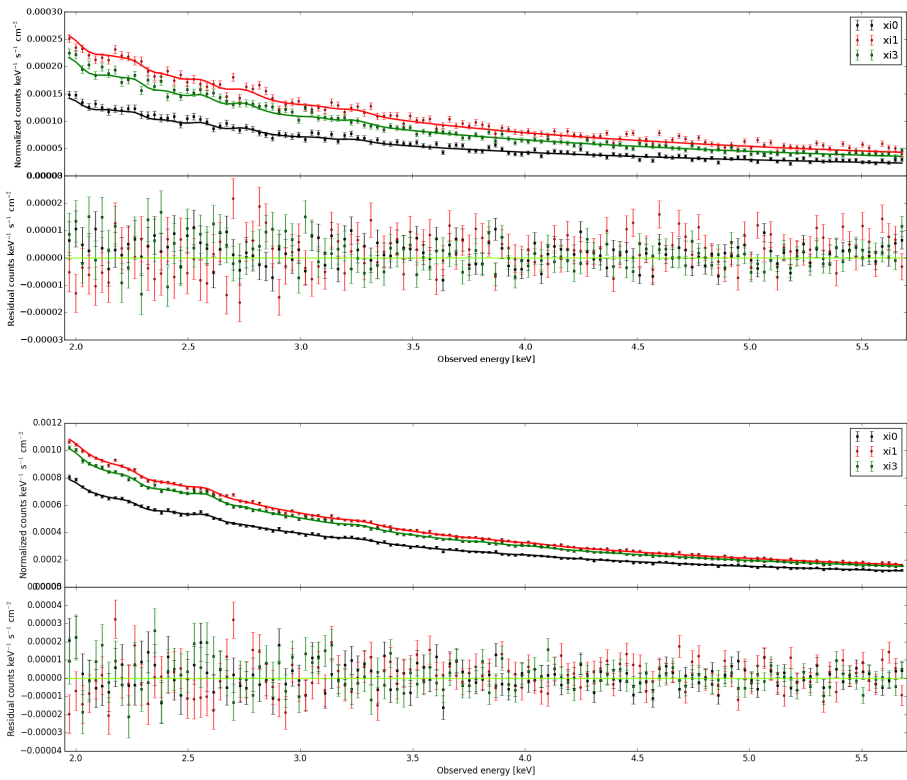**Figure 4.6:** Regions 2 and 3. Showing the data and model fits to those regions, with the residuals in the bottom panel.

Figure 4.7: Regions 4 and 2-4. Showing the data and model fits to those regions, with the residuals in the bottom panel.

ObsID	FI Exp (ks)	BI Exp (ks)	d arcmin	ObsID	FI Exp (ks)	BI Exp (ks)	d arcmin	ObsID	FI Exp (ks)	BI Exp (ks)	d arcmin
101012020	79.9	39.9	0	804057010	24.1	12.0	32.80	806129010	12.9	6.4	75.36
102011010	70.2	35.1	0	806136010	13.1	6.5	32.81	804067010	43.9	22.0	81.63
102012010	107.0	53.5	0	805104010	13.9	6.9	32.88	806118010	27.1	13.6	81.79
103004010	68.2	34.1	0	806124010	19.1	9.5	33.11	806106010	24.7	12.4	82.67
103004020	92.6	46.3	0	801049040	15.0	7.5	33.12	805100010	18.9	9.5	82.82
104018010	33.9	17.0	0	801049010	50.3	25.2	35.94	805107010	15.2	7.6	83.11
104019010	67.2	33.6	0	806113010	19.1	9.5	40.25	804060010	43.2	21.7	83.15
105009010	59.2	29.6	0	806101010	19.5	9.7	40.86	806142010	31.6	15.8	83.23
105009020	66.0	33.0	0	806137010	21.0	10.5	41.23	806130010	27.5	13.7	83.55
106005010	68.2	34.1	0	806125010	11.1	5.6	41.72	808087010	34.8	17.4	87.97
106005020	68.5	41.1	0	804065010	24.5	12.2	48.03	806119010	32.5	16.3	90.56
107005010	66.4	33.2	0	806114010	16.3	8.2	48.21	805111010	13.1	6.5	91.08
107005020	60.5	35.6	0	805098010	13.5	6.7	49.02	806107010	30.4	15.2	91.42
108005010	62.5	38.1	0	806102010	14.4	7.2	49.05	805115010	19.5	9.7	91.53
108005020	68.2	34.1	0	804058010	22.8	11.5	49.58	806143010	19.6	9.8	91.60
804063010	26.9	13.5	14.48	806138010	19.7	9.9	49.59	806131010	27.9	13.9	92.00
806111010	21.6	10.8	14.70	805105010	21.8	10.9	49.61	804068010	60.2	30.1	98.38
805096010	16.3	8.1	15.54	806126010	15.0	7.5	49.93	806120010	17.1	8.6	98.57
806099010	23.1	11.6	15.58	806115010	23.8	11.9	56.99	805101010	29.5	14.7	99.48
807022010	46.0	23.0	15.78	806103010	20.5	10.3	57.79	806108010	20.6	10.3	99.49
807020010	46.0	23.0	16.01	806139010	17.5	8.8	58.08	804061010	56.8	28.4	99.92
804056010	14.2	7.1	16.01	806127010	20.4	10.2	58.39	805108010	24.9	12.4	99.95
805103010	12.9	6.4	16.07	701007020	71.4	35.7	59.21	806144010	20.6	10.3	100.05
806135010	18.6	9.3	16.16	701007010	6.8	3.4	64.34	806132010	13.9	7.0	100.37
807019010	27.4	13.7	16.22	804066010	42.9	21.5	64.87	806121010	14.1	7.1	107.34
806123010	19.7	9.8	16.44	806116010	21.7	10.8	65.11	805112010	26.2	13.1	107.82
805046010	35.2	17.6	16.62	806104010	26.4	13.2	65.96	806109010	13.7	6.9	108.17
805045010	53.5	26.8	17.91	805099010	18.6	9.3	65.97	805116010	24.9	12.8	108.29
805047010	33.4	16.7	18.76	806140010	12.6	6.3	66.32	806145010	25.5	12.7	108.32
807023010	27.1	13.6	19.10	804059010	36.6	18.3	66.40	806133010	16.2	8.1	108.99
807021010	35.8	17.9	19.13	805106010	19.9	9.9	66.53	804069010	60.8	30.4	115.20
805048010	29.1	14.5	19.13	806128010	20.4	10.2	66.90	806122010	20.7	10.3	115.46
801049030	61.0	30.5	27.74	806117010	20.4	10.2	73.79	806110010	20.7	10.4	116.21
801049020	53.7	26.9	31.21	805110010	18.0	9.0	74.38	805102010	25.8	12.9	116.24
806112010	21.7	10.8	31.37	806105010	17.3	8.6	74.60	804062010	54.5	27.4	116.70
804064010	19.1	9.6	31.44	806141010	22.2	11.1	74.79	805109010	30.7	15.3	116.74
806100010	18.0	9.0	32.26	805114010	13.7	6.9	74.82	806146010	14.6	7.3	117.04
805097010	21.2	10.5	32.47	808085010	37.4	18.7	74.85	806134010	22.0	11.0	117.10

Table 4.8: *Suzaku* observations of the Perseus cluster utilized in this study. d indicates the distance from the cluster center in arcminutes

Parameter	Reg 1	Reg 1a	Reg 1b	Reg 1c	Reg 2	Reg 3	Reg 4	Reg 2-4
kT based on S (keV)	3.13	2.97	3.18	3.25	3.74	2.37	2.47	3.60
kT based on Ca (keV)	4.02	3.65	3.92	4.85	4.77	–	–	4.14
Flux of Cl XVII at 2.96 keV	1571.18	882.46	868.90	415.20	50.52	5.52	2.19	11.00
Flux of Cl XVII at 3.51 keV	240.05	133.96	133.00	63.73	7.88	0.81	0.32	1.71
Flux of K XVIII at 3.47 keV	227.78	138.35	122.66	56.43	5.32	1.13	0.43	1.25
Flux of K XVIII at 3.49 keV	112.44	68.27	60.59	27.90	2.65	0.57	0.22	0.62
Flux of K XVIII at 3.51 keV	471.09	280.16	255.33	118.56	11.78	2.13	0.82	2.73
Flux of Ar DR XVII at 3.62 keV	66.87	44.72	35.00	15.46	1.14	0.58	0.20	0.29

Table 4.9: Same as Table 4.6 but for Anders & Grevesse (1989) solar abundances: sstimated fluxes of the Cl XVII, K XVIII, Ar DR XVII lines are in the units of 10^{-8} pht cm^{-2} s^{-1} from AtomDB. The fluxes (and not the temperature) in this table are dependent on the assumed solar abundance, and are employed in the fits by setting the upper and lower allowed limits for the fitting procedure to 3 times and 0.1 times this flux, respectively.

5 | CORRELATION METHOD FOR WEAK LINE SEARCHES

5.1 Introduction

Spectral modeling of X-ray observations is a well-established field with well-established techniques and tools. Current X-ray detectors have energy resolutions of order 100 eV, however, which can cause fitting degeneracies between various features, such as between various emission lines, or between the continuum and emission lines. This paper introduces a proof-of-concept to distinguish spectral components by their scaling characteristics between objects and environments.

A particular example, and the nominal science case on which we focus the development, is the possibility that the Dark Matter may decay with a monochromatic X-ray emission line as a result. This kind of Dark Matter has been well described, and covers a wide range of particles. For example Essig et al. (2013) describes a number of these along with current bounds, and more can be found in e.g. Abazajian et al. (2001); El Aisati et al. (2014); Frandsen et al. (2014); Iakubovskyi (2014).

Currently, a candidate signal for decaying Dark Matter is being scrutinized thoroughly. It was discovered in spectra of galaxies and clusters of galaxies (Boyarsky et al., 2014a; Bulbul et al., 2014a), and subsequently studied in many other objects (e.g., Boyarsky et al., 2015; Jeltema & Profumo, 2015; Urban et al., 2015; Malyshev et al., 2014; Ruchayskiy et al., 2015; Jeltema & Profumo, 2016; Bulbul et al., 2016a; Franse et al., 2016, and references therein), although the final verdict remains due. The main approach to establishing whether this interpretation is correct, is to compare the strength of this signal between objects, and seeing that the signal scales as the total Dark Matter mass inside the field-of-view of the telescope over the distance to the object squared. However, the signal strength has to be measured from spectral fits. In single objects, the low statistical significance means that the flux has a large uncertainty and may be susceptible to spectral model degeneracies. The statistics may be increased by stacking a number of objects together and fitting to the resulting spectrum (Bulbul et al., 2014a). This has a number of advantages, among which that instrumental effects smear out among the spectrum (as long as the stacked sample has a large enough spread in redshifts). However, the spectrum will be a superposition of varying environments, so that it becomes more difficult to relate

model parameters to each other by simple physical relationships. In addition, a detection in a stack precludes the possibility of comparing signal strength between the members of the stack, although comparing the signal strength between different stacks is still possible.

Here we present a method to combine the statistical power of a stacked spectrum with the ability to constrain the origin of a signal based on the scaling between the single objects. Even though it would be impossible to measure the signal strength from each object individually, we combine the limited number of X-ray events and the knowledge of the mass and redshift of each object into a single estimator that reflects not only the strength of a Dark Matter decay signal, but also whether or not its origin is actually Dark Matter decay.

Scaling up this method to use as much archival data as possible, and introducing more advanced simulations and minimization approaches along with the required computing power, it is fully expected that this method can provide competitive limits on the Dark Matter decay. With the loss of the *Hitomi* mission, our approach may be ideally suited to testing the Dark Matter interpretation of the 3.5 keV signal in the future.

As a bonus, the method does not require background subtraction and can be made insensitive to detector and mass calibration systematic effects under certain circumstances. This method is also easily generalized and applied to any object or type of signal.

In Section 5.2 we will lay the mathematical groundwork for performing the correlation, while Section 5.3 details how to use this formalism to perform a search for a Dark Matter decay signal. We describe the data used and the practical implementation of the method in Section 5.4 and discuss the error estimation in Section 5.5. Section 5.6 contains the central results of our work, where a set of simulated signals is added to the real dataset, and we report the success rate of recovering the simulated signals using our method. Our conclusions are summarized in Section 5.7, and in Section 5.8 we discuss the performance of our method and possible improvements. The appendices contain derivations of various equations presented throughout the main text, the results of a few null tests, and a note on the practical difference between a correlation and a weighted average and instructions on how to incorporate weighting in the correlation.

5.2   Formalism

The formalism is adapted from Refregier et al. (1997), where the correlation w can be expressed as

$$w = \frac{\langle NI \rangle}{\langle N \rangle \langle I \rangle} - 1. \tag{5.1}$$

Here, quantities N and I are being correlated over some field that is divided into cells, and the averages indicated by $\langle ... \rangle$ are performed over these cells. In this work we are interested in possible Dark Matter signals, and therefore correlate the detected X-rays (represented as I) with a catalog of galaxy groups that serve as a proxy for Dark Matter mass overdensities. These are represented by N, but N can contain any (combination of) physical characteristics of the galaxy groups. We call this the correlator throughout this work. Of course, N can represent any other kind of object if so desired. The basic

expressions for these are simply

$$\langle NI \rangle = \frac{1}{N_C} \sum_{i=1}^{N_C} I_i N_i \tag{5.2}$$

$$\langle I \rangle = \frac{1}{N_C} \sum_{i=1}^{N_C} I_i \tag{5.3}$$

$$\langle N \rangle = \frac{1}{N_C} \sum_{i=1}^{N_C} N_i. \tag{5.4}$$

with N_C the number of cells in the field. If the two quantities are uncorrelated, their averages become independent so that $\langle NI \rangle = \langle N \rangle \langle I \rangle$ and $w = 0$. For a correlation, w becomes larger than 0, and smaller than 0 when an anti-correlation exists. Below, we will extend this formalism in various ways, modifying the above expressions

As noted, the correlator N can be chosen to represent any kind of physical property or object. In this work we are interested in galaxy groups as tracers of the Dark Matter density field, and will use various (combinations of) galaxy group properties as the correlator.

The central methodology in this work is to perform the correlation in bins of spectral energy and therefore in redshift-space. Essentially, it is possible to distinguish the various components of the raw X-ray data by their spectral behaviour relative to the redshifts of the physical objects that are being correlated with.

Since our interest is in the X-rays emitted by the galaxy groups, we work in the rest-frames of each of those groups. When computing $\langle NI \rangle$, whenever a cell i contains a galaxy group k, the entire X-ray spectrum of that cell I_i is blueshifted back to the group's redshift z_k, represented as $\zeta(I_i, z_k)$ or ζ_{ik} for short. It is possible for a cell to contain multiple groups at different redshifts. In that case, this blueshifting is performed once for each group. The expression becomes

$$\langle NI \rangle = \frac{1}{N_C} \sum_{i=1}^{N_C} \sum_{k=1}^{N_g(i)} \zeta(I_i, z_k) N_k. \tag{5.5}$$

with $N_g(i)$ the number of groups in cell i.

The X-rays coming from the galaxy groups will indeed be redshifted (which is what the ζ_{ik} corrects for), but all backgrounds and foregrounds that are present in I_i will also be shifted by ζ_{ik}. This shift is random with respect to the fore-/backgrounds, a fact that can be used to separate the galaxy group emission from those backgrounds. In order to do that correctly, $\langle I \rangle$ should in a sense describe the average expected result of performing these shifts on the backgrounds. In other words, $\langle I \rangle$ is the average X-ray spectrum of the entire field, averaged in turn over all the shifts performed while calculating $\langle NI \rangle$.

In addition, the correlator N_k used in $\langle NI \rangle$ is effectively giving random weights to the backgrounds in each cell that contains a group. Analogously to the the blueshifting described above, therefore, the computation of $\langle I \rangle$ must also include the distribution of the values of the correlator N_k in the group catalog. Specifically, during the calculation of $\langle NI \rangle$, the redshifts and correlator values come in pairs (that is to say, the redshift of

one group always goes along with the correlator value of the same group), so all in all, to calculate $\langle I \rangle$, the distribution of (z_k, N_k) must be taken into account. This gives

$$\langle I \rangle = \frac{1}{N_C} \sum_{i=1}^{N_C} \frac{1}{\sum_l^{N_g} N_l} \sum_{k=1}^{N_g} \zeta(I_i, z_k) N_k \tag{5.6}$$

where N_g is the total number of groups in the catalog, the factor $\sum_l^{N_g} N_l$ accounts for the proper normalization.

Note that without the blueshifting, it would not be required to write $\langle I \rangle$ explicitly in terms of (sums involving) N_k, as the sum over the groups k would be independent of the sum over the cells i, and the expression would be mathematically equivalent to Equation 5.3. Due to the inclusion of ζ_{ik}, the two sums mix and we get Equation 5.6.

5.2.1   (De)composition of the Correlation

If the true X-ray emission is know in terms of its components, we can predict what the correlation should be for various choices of the correlator. We will actually use $w\langle I \rangle$ as this turns out to be the most useful choice. Below we give a few examples of this, with derivations given in Appendix 5.A.1. With the expressions below in hand, we shall see that it is possible to invert the process and obtain an estimate of the true X-ray emission per component.

If the true emission is given by an intrinsic luminosity that is the same for each group (L_{grp}), the observed flux for each cell would be $I_i = L_{grp}/(4\pi D_{lum,i}^2)$. Using as correlator then $1/(4\pi D_{lum}^2)$, the correlation will result in

$$w\langle I \rangle = L_{grp} \frac{\sum_k 1/D_k^4}{\sum_k 1/D_k^2} \left(1 - \frac{1}{N_C} \right) \tag{5.7}$$

where the sums run over all groups, and for convenience we write $4\pi D_{lum,k}^2 = D_k^2$. Given the catalog and the known distances, it is possible to solve for L_{grp}.

A more general case would be when the true emission is given by an arbitrary number of components, each of which scales with a different power β of the group mass M like so

$$I_i = \sum_\beta L_\beta M_i^\beta / D_i^2. \tag{5.8}$$

If the correlator used is then M^γ/D^2 (for an arbitrary γ), the resulting correlation is

$$w_\gamma \langle I_\gamma \rangle = \sum_\beta L_\beta \frac{\sum M^{\beta+\gamma}/D^4}{\sum M^\gamma/D^2} \left(1 - \frac{1}{N_C} \right)$$

$$\equiv \sum_\beta L_\beta A_{\beta\gamma} \tag{5.9}$$

where the sums run over all objects k in the catalog and the k subscripts on all powers of M and D have been omitted for readability.

In this case, the masses and distances of the groups are known, the correlation $w_\gamma \langle I_\gamma \rangle$ is measured, but there are an arbitrary number of unknown L_β's (if at least the β's are

known, otherwise there are twice as many unknowns). It is still possible to solve for these unknowns if the correlation is repeated for at least as many different values of γ as there are unknowns. In that case, Equation 5.9 becomes a system of equations that can be solved analytically if all the components can indeed be accurately described by Equation 5.7 and the correlations is noise-free.

Of course, this is not the most general case imaginable, but the principle holds for any model as long as it scales with known (for some value of known) properties of the objects in the catalog. This principle also holds in the presence of foregrounds and backgrounds, as these correlate out and do not contribute to $w\langle I \rangle$ on average.

This is the central principle that we will use throughout this paper to search for a Dark Matter decay signal. Of course the true emission of the galaxy groups may not be perfectly described like in Equation 5.7 with a minimal set of components, nor will the measurement of the correlation be noise free, so Section 5.3 will detail how to put the principle into practice.

5.3 Methodology

In this section we will describe how to use the formalism from Section 5.2 to search for Dark Matter decay-like signals in practice.

After choosing a suitable field, and having obtained the X-ray data and galaxy group catalog appropriate for that field, a correlation can be computed given some correlator. The choice of correlator should be related to the signal that is being looked for. In the case of Dark Matter decay, the expected behaviour is M^γ/D^2 with $\gamma = 1$, so that is a good starting point.

In principle we could then compute some more correlations, for varying values of γ for example. Then we could assume some model for the intrinsic correlated emission (like Equation 5.7), and continue to solve the system of equations 5.9 using this set of correlations (having different correlators each), and a choice of β's. Regarding the search for Dark Matter decay, then at least one of those β's should be 1, and the objective is to find a significant line-like contribution of the $\beta = 1$ component. This approach will be discussed in Section 5.8.1, but turns out to be not very efficient to solve directly.

As we shall see in Section 5.6, even quite weak signals (in terms of signal-to-noise) can sometimes be seen by eye in the correlation spectrum (the value of w as a function of restframe energy). Therefore we shall use a quite naive estimator which will prove to work remarkably well (also in Section 5.6) and takes advantage of the fact that we are looking for a spectral line feature (although a generalized methodology will be described later).

This simple estimator to test for the presence and strength of a decay line is to take for a particular energy bin the difference between that bin's w value, minus the average of the neighboring bins, by way of continuum subtraction. We will refer to this estimator as Δw. In fact, to make use of Equation 5.9, we should actually use $\Delta(w_\gamma \langle I_\gamma \rangle)$, which we will write as Δ_γ for short.

Some arbitrariness is present in the choice on the width of the energy bin. Considering the spectral resolution of the instrument, also the choice of which bins to use for the 'signal region' and which bins to use for the continuum estimate is somewhat arbitrary. If

we call the energy bin under consideration the 'central bin'; the central bin together with potential extra bins that are considered to contain signal the 'signal bins'; the bins that are used to estimate the continuum 'side bins'; and potentially some bins between the signal bins and the side bins that may be ignored as 'skipped bins'; then the estimator can be written as

$$\Delta_\gamma = \Delta(w_\gamma \langle I_\gamma \rangle)$$

$$= \sum_b^{\text{signal bins}} w_\gamma \langle I_\gamma \rangle (E_b) - \frac{N_{\text{signal bins}}}{N_{\text{side bins}}} \sum_s^{\text{side bins}} w_\gamma \langle I_\gamma \rangle (E_s) \qquad (5.10)$$

We will indicate the choice of which bins are used schematically for example like so

$$sskxXxkss$$

representing the bins in energy space, with X the central bin, x the remaining signal bins, k skipped bins and s the side bins used for continuum subtraction. In words, we will say this scheme uses 1 extra signal bin, 1 skipped bin and 2 side bins (since the scheme is symmetric around the central bin, we refer only to one side).

A significant non-zero and positive value for Δ_γ is an indicator for a line-like emission feature. Below, we will describe how to use this estimator Δ_γ to search for Dark Matter decay-like signals. Four different approaches will be described, in order of increasing complexity. The efficacy of each will be tested in Section 5.6.

- It is already possible to use $\Delta_{\gamma=1}$ to obtain $L_{\beta=1}$ if one assumes that the excess is caused by a Dark Matter decay-like signal, and solves Equation 5.9 like so; $L_1 = \Delta_1/A_{11}$. However, this carries no intrinsic information about the origin of the excess.

- One way to test whether a Dark Matter decay may be the cause of non-zero and positive Δ_γ could be to take the set of computed correlations $\{\Delta_\gamma\}$ (for a set of varying γ's), and solve the resulting system of equations for $L_{\beta=1}$, assuming a single Dark Matter decay component.

$$\Delta_1 = L_1 A_{11}$$
$$\Delta_2 = L_1 A_{12} \qquad (5.11)$$
$$\vdots$$
$$\Delta_n = L_1 A_{1n}$$

Because real data contains noise, and because it is not *a priori* known whether a single $\beta = 1$ component is the correct interpretation, this system of equations probably does not have an perfect analytical solution. Instead, one should solve this system using some fitting or optimization procedure. This difference between solving the system of equations using the the set of γ's, and only using $\gamma = 1$, is that one may judge whether the Dark Matter decay is a consistent interpretation (ie., that assuming a single $\beta = 1$ component is correct) by requiring that the residuals from the fitting are small.

- Instead of just requiring small residuals from a given assumption (single $\beta = 1$ component), it is more convincing to let the optimization procedure find the best-fit β for the obtained $\{\Delta_\gamma\}$. So, still only a single component is assumed, but the model now is two-parameter (β and L_β) and the system of equations to be solved is

$$
\begin{aligned}
\Delta_1 &= L_\beta A_{\beta 1} \\
\Delta_2 &= L_\beta A_{\beta 2} \\
&\vdots \\
\Delta_n &= L_\beta A_{\beta n}
\end{aligned}
\tag{5.12}
$$

- Lastly, it is of course possible to include more than a single component to describe $\{\Delta_\gamma\}$. The value of β for each component can be picked *a priori*, or be taken as a free parameter. The number of different correlators used to solve this system should be at least equal to the number of free parameters.

Having decided upon which of the above approaches to employ, one obtains the 'decomposition' of the correlation (best-fit solution to Equation 5.9), one for each energy bin. An example of such a 'spectrum' is given in Figure 5.1, for a simulated signal (see Section 5.6). Such a figure can then be used to determine whether a Dark Matter decay signal is present in the data. The requirements for that are; 1) a significant positive value for the $L_{\beta=1}$ component, 2) a best-fit β close to 1 (if β was a free parameter), 3) a high goodness-of-fit and 4) a line-like shape in the 'decomposition spectrum' (with regards to the instrument resolution).

5.4 Data and Implementation

To test and explore this method, we utilize the publicly available data and catalogs of the COSMOS survey (Scoville et al., 2007). This field of roughly two square degrees has been covered in most wavelength regimes, among with deep *XMM-Newton* exposures, and multiple catalogs of Dark Matter tracers are available. The COSMOS field is relatively empty of very bright objects in any wavelength and galactic foregrounds are low and reasonably homogeneous.

The main Dark Matter tracer population that we use is the X-ray selected galaxy group catalog by George et al. (2011). It contains 183 groups between redshifts of 0 and 1, which have been detected by a spatial wavelet analysis on the X-ray mosaic and confirmed by optical galaxy overdensities. This we refer to as the G11-sample. Another catalog is also available, which is the optically selected group catalog by Knobel et al. (2012). It enables us to check for systematics and in the case of a possible line candidate test the robustness of that detection. This catalog uses spectroscopic redshift measurements and a friend-of-friends algorithm to detect galaxy groups. It contains around 1500 groups of which almost 200 have 5 or more spectroscopic members. We shall refer to this catalog as the '20k' sample, since it is based on the zCOSMOS spectroscopic survey (Lilly et al., 2007) of nearly 20,000 redshifts. The zCOSMOS field is slightly smaller than the full COSMOS field.
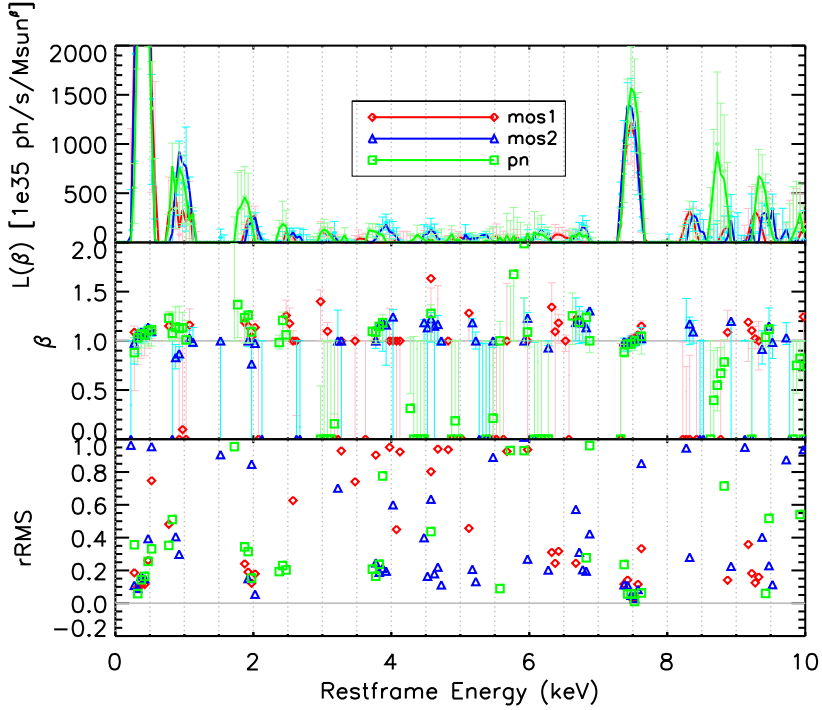
Figure 5.1: *How to determine if there's a Dark Matter decay line in the data?* Example plot of simulated data showing the last step in the methodology (see text, Sections 5.2 and 5.3). All four requirements are met: 1) a significant positive measured value for L_β (top panel) reflecting the intrinsic luminosity of the correlated excess emission; 2) a best-fit value of β consistent with 1 (middle panel), reflecting that the correlated excess emission scales with mass to the power $\beta = 1$, as is required of Dark Matter decay; 3) a sufficiently low relative RMS deviation (bottom panel) for this combination of best-fit values of L_β and β; 4) a line-like profile in the top panel, since Dark Matter decay is a monochromatic signal. Therefore it can be concluded that a Dark Matter decay signal is present at 7.5 keV in this simulated data. This 'decomposition spectrum' is for the real COSMOS data (Section 5.4) and a simulated injected signal (Section 5.6). The simulated signal is indeed at 7.5 keV and is a very strong signal in order to demonstrate the method. Note that the 'significant' peak below 0.5 keV is an artifact of the estimator Δ_γ due to edge effects (the edge of the spectrum). Different colors and symbols indicate data from the three different cameras (mos1, mos2 and pn instruments represented in red and by diamonds, in blue and by triangles, and in green and by squares respectively). The error bars in the top and middle panels indicate 68% bootstrap intervals (Section 5.5).

We use all available *XMM-Newton* data of the COSMOS field (Hasinger et al., 2006) that is available in the science archives. The standard `SAS` pipelines were used to reduce the data and filter the data for flares using the `espfilt` procedure. Additional flare filtering was performed based on in-FoV and out-FoV high energy count rates (De Luca & Molendi, 2004), with observations having a ratio over 1.3 being excluded. The whole COSMOS field was then divided into a square grid with 75" spacing, resulting in 5256 cells. This cell size was chosen to be somewhat larger than the *XMM-Newton* PSF. Using the `SAS` procedures `rmfgen` and `arfgen` the effective area curves for each exposure of each cell were generated. The different exposures of each cell were then combined by weighting by the cleaned exposure time, effective area and usable solid angle (not all pixels are usable). The data from the three instruments (MOS1, MOS2 and PN) and the correlation products were kept separate throughout this work unless otherwise noted. The main computational time sink in the entire method is the generation of `rmf` and `arf` files for each exposure of each cell. This is the reason for using a flexible and multi-functional square grid.

Obs ID	Expsure (ks)			Obs ID	Expsure (ks)		
	MOS1	MOS2	PN		MOS1	MOS2	PN
0203360101	28.9	29.0	24.3	0302350701	17.8	18.2	14.7
0203360201	15.1	15.1	10.6	0302350801	18.9	18.6	15.1
0203360301	30.1	30.3	24.2	0302350901	7.5	8.1	3.4
0203360401	27.2	26.9	20.2	0302351001	36.1	37.7	28.2
0203360501	26.0	26.3	19.9	0302351101	15.1	15.5	11.5
0203360601	23.1	22.1	18.4	0302351201	15.0	14.8	12.1
0203360701	32.1	33.0	27.0	0302351301	18.6	18.5	15.3
0203360801			14.1	0302351401	16.2	17.2	8.7
0203360901	20.7	21.4	16.2	0302351501	14.1	13.9	9.5
0203361001	14.0	13.6	10.6	0302351601	28.9	29.4	21.9
0203361101	19.6	20.5	7.9	0302351701	19.0	18.3	14.3
0203361201	25.3	25.0	21.6	0302351801	17.3	17.4	14.1
0203361301	25.1	25.0	21.6	0302351901	11.4	10.5	7.5
0203361401	30.5	29.8	26.1	0302352001	4.8	4.8	3.5
0203361501	23.2	23.4	13.3	0302352201	7.6	7.8	3.9
0203361701	30.0	29.8	25.1	0302352301	4.4	5.4	3.0
0203361801	26.4	26.4	22.9	0302352401	18.8	18.4	15.0
0203361901	22.9	23.2	19.5	0302352501	22.5	22.5	19.1
0203362001	8.1	7.5	4.6	0302353001	2.7	2.7	2.1
0203362101	59.0	58.2	51.2	0302353101	17.5	17.8	13.6
0203362201	28.3	29.2	13.4	0302353201	11.3	11.0	7.6
0302350101	12.9	14.0	11.5	0302353301	12.2	12.4	8.7
0302350201	13.6	14.4	8.9	0302353401	8.8	9.5	5.1
0302350401	7.3	7.7		0501170101	32.1	31.5	26.5
0302350501	18.4	18.6	15.1	0501170201	29.8	30.2	22.0
0302350601	17.0	16.4					
				Total	99.3	99.9	75.5

Table 5.1: Cleaned exposure times of the used XMM-COSMOS observations. Entries without exposure listed were discarded for having a Fin-Fout ratio too high (see text).

During development, it was found that the outer regions of the full COSMOS field are not usable for the correlation. As metioned, the 20k-sample of galaxy groups was only based on the zCOSMOS field. However, the G11-sample suffers from the reduced sensitivity at the outsides of the COSMOS field, caused by the vignetting effect of *XMM-Newton*. Even in the mosaic of all *XMM-Newton* exposures, the outermost regions of the COSMOS field are only covered by the edges of the detector, which have lower effective area. Including the full COSMOS field when correlating using the G11 sample caused residual systematic effects for that reason. Throughout the rest of this work, we shall consider only the zCOSMOS field, whose boundaries coincide well with the region of lower sensitivity of the COSMOS X-ray mosaic.

For solving the system of equations described in Section 5.3, we employ the `IDL` minimization routine `TNMIN` with a relative least-squares implementation. This procedure is general enough to be able to solve the multi-component decompositions and allows limiting the L_β parameters to only positive values.

5.5   Error Estimation

Although it is possible to simply propagate in the usual way the Poisson noise through the entire calculations of $\langle NI \rangle$, $\langle I \rangle$, and w or $w\langle I \rangle$, it is likely that upon scaling up this method the Poissonian noise becomes subdominant to for example chance alignments of sources and features in the astrophysical or instrumental background. More importantly maybe, is that the the w_γ (and Δ_γ) and their errors will be correlated between different values for γ. Also the energy bins within a correlation spectrum will be correlated up to a point due to the blueshifting procedure (and due to the instrumental spectral resolution).

For the purposes then of the (estimators) of the decomposition, the propagated Poissonian noise is insufficient. The most efficient way to emulate all possible sources of uncertainty at the same time is to perform a bootstrapping resampling of the dataset. We split the zCOSMOS field into 9 evenly sized subfields. For each bootstrap iteration then, a new realization of the zCOSMOS field is obtained by drawing randomly with replacement 9 subfields from the original 9. The entire algorithm is then applied to this new 'survey'.

However, by resampling the field, the group catalog for each realisation will also be different. The values of w and $w\langle I \rangle$ depend on the group catalog, so that the spread in values of w from the bootstrap does not represent an uncertainty in the 'true' value of w since there is no one true value for w among the bootstrap realizations. The decomposition in terms of L_β does not depend on the group catalog in principle, as L_β is an intrinsic properties of the physical process. However, a resampling of the field can seriously affect the significance of any correlated signal, if the resampled catalog contains many fewer, less massive and/or higher redshift groups for example. Therefore, during bootstrapping we only accept resamplings of the field if the resulting group catalog is within 0.02 dex (about 5%) of the original group catalog in terms of $\sum_k M_k/D_k^2$, which serves as a proxy for the expected total received signal photons.

This constrained bootstrap provides an uncertainty interval for the decomposition, and is now also suited for obtaining uncertainties on w and $w\langle I \rangle$. The requirement threshold on the similarity of bootstrapped group catalogs is somewhat arbitrary. Larger (more lenient) thresholds will broaden the uncertainty interval (overestimating the error), while

stricter requirements risk limiting the bootstrap process so it is no longer representative of the actual errors, leading to underestimation of the errors. The threshold of 0.02 dex mentioned above has been established by trial-and-error, it having been observed that after applying an initial lenient threshold, only the lower end of the uncertainty interval was affected, as would be expected. Stronger thresholds would however also start to reduce the size of the uncertainty interval at the high end. In addition, at 0.02 dex, only 20% of the resamplings comply with the threshold. Stronger thresholding would therefore likely inhibit the proper working of the bootstrap. In Section 5.6 we compare the the bootstrap interval to the scatter in simulated signal recovery, and find that the bootstrap interval is larger than the scatter. This may indicate that the bootstrap errors are still overestimating the errors due to other effects. In order to improve error estimation a suite of full end-to-end simulations would be required, possibly supported by cosmological hydrodynamic simulations and mock catalogs.

5.6 Recovery of Injected Decay Signals

To actually test the ability of this method to detect Dark Matter decay-like emission signals without the need to rely on spectral modeling, we inject into the real COSMOS dataset several simulated Dark Matter decay signals. For this purpose, we utilize the `fakeit` procedure, which creates a simulated event list given such information as the telescope response and exposure, and input parameters for the simulated signal. In this particular case, we seek to relate the simulated Dark Matter decay to actual Dark Matter particle models, to place the performance into context. We compare to the sterile neutrino model as discussed in e.g. Dodelson & Widrow (1994); Abazajian et al. (2001); Boyarsky et al. (2009c), which for a given particle mass m_{DM} and mixing angle $sin^2(2\theta)$ generates a flux of

$$F_{DM} = 3.9 \cdot 10^{-7} \frac{ph}{cm^2 s} \left[\frac{\sin^2(2\theta)}{10^{-8}} \right] \left[\frac{m_{DM}}{5keV} \right]^4$$
$$\times \left[\frac{D_L(z = 0.1)}{D_L(z)} \right]^2 \left[\frac{M}{10^{13} M_\odot} \right] \tag{5.13}$$

for an object at redshift z with mass M.

We then inject a simulated redshifted gaussian line into the data at each cell that contains an object from the catalog, at $E = m_{DM}/2(z + 1)$ with a normalization as given by the above equation and according to the mass and luminosity distance of the object. The generated event list is concatenated to the original cell's event list, and the correlation can be computed again.

We simulated a number of decay signals at various values for m_{DM} and $sin^2(2\theta)$, for the G11 sample of galaxy groups. Because the injected signal is known and we can compare the pre-injection and post-injection correlation, we prove in Figure 5.2 that Equation 5.9 is correct. Here, we plot the input luminosity per unit mass against the luminosity derived from the difference between pre- and post-injection $w(\gamma = 1)$ and equation 5.9. The correspondence is one-to-one up to the poissonian noise from the simulation.

For a few of these we show w as a function of restframe energy in Figure 5.3. Clearly, the only difference between these cases is the addition of a line at a particular energy. The
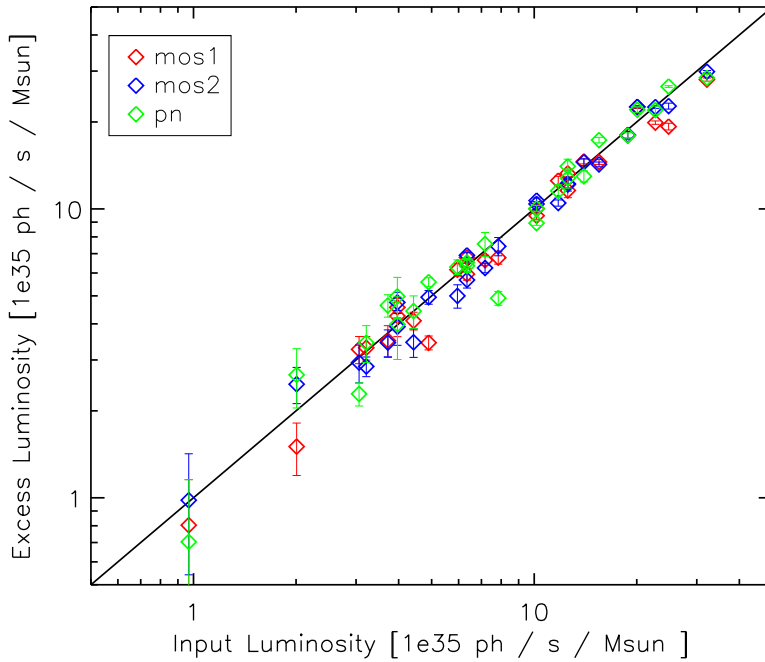
Figure 5.2: Practical proof of the validity of Equation 5.9 and therefore the formalism presented in this work. The input intrinsic Dark Matter decay luminosity (in 10^{35} ph s^{-1} $M_\odot^{-1}$) to the simulation compared to the *change* in correlation pre- and post-injection as expressed through Equation 5.9. Note that this is not a realistic measurement (see Section 5.6 for that), but rather the response of the correlation w to the injection of a fake signal. Excellent agreement confirms in practice the behaviour of the formalism as described in Section 5.2, while the scatter is due to the randomized nature of the `fakeit` simulation's photon distributions. Colors indicate the 3 different detectors, while the error bars in this case indicate the Poisson noise on the added signal.
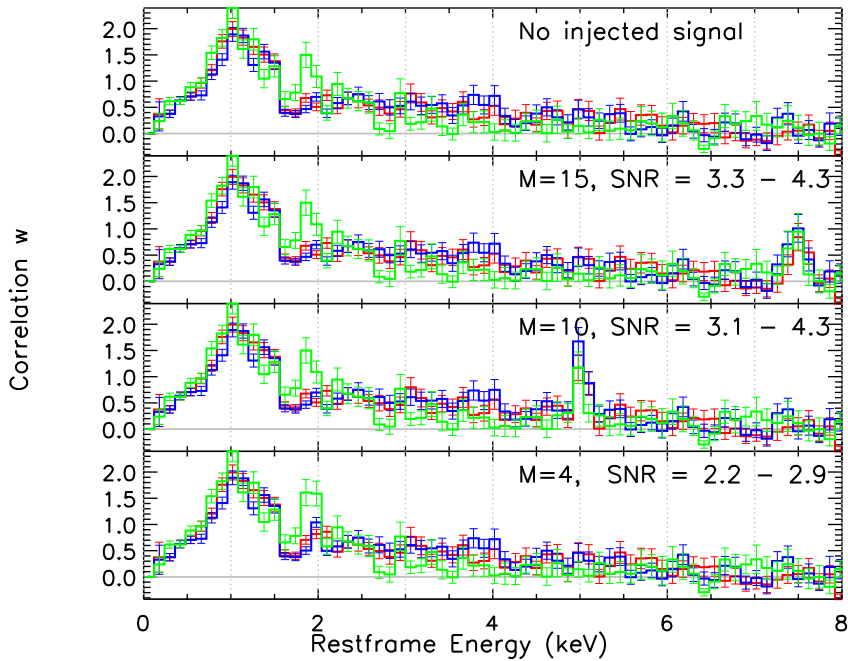
Figure 5.3: Example of the effect of a few simulated signals. Correlation as a function of energy for the nominal zCOSMOS field, using the G11 sample, correlating with M/D^2_{lum} using energy bins of 120 eV, in the top panel. Other panels are the same, but with a simulated line added for a particle with the indicated mass (in keV, so the signal is at an energy half that mass). The SNR indicated is the total amount of raw simulated photons divided by the square root of the raw total amount of photons at the energy of injection. The range on the SNR indicated is spanned by the different cameras. Red, blue and green lines refer to MOS1, MOS2, and PN cameras respectively. Error bars are Poissonian propagated errors for indicative purposes only (see Section 5.5).
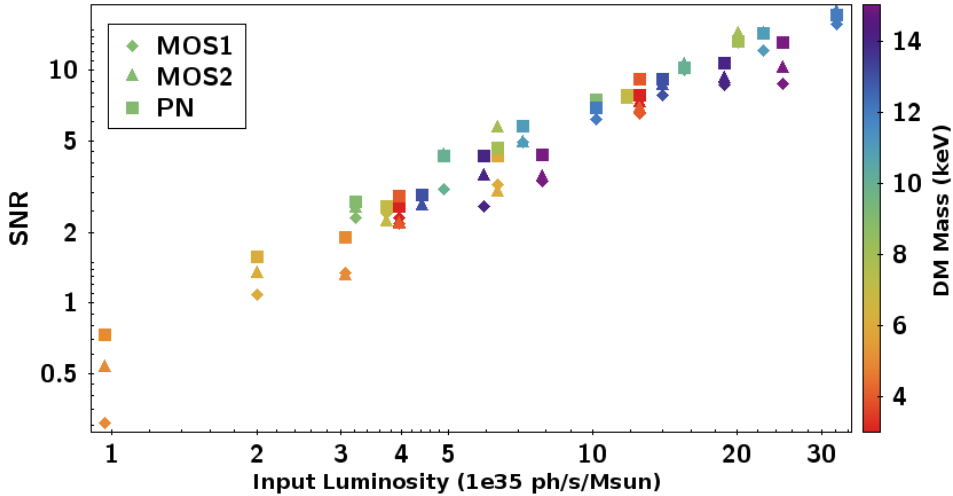
Figure 5.4: The set of simulated signals used in Section 5.6, by input luminosity versus the signal-to-noise ratio in terms in total injected signal photons to the square root of the total photons. The three cameras are shown separately as the SNR differs between them. Points are coloured by the Dark Matter particle mass used for that simulation, which is related to the injection restframe energy. Most of the scatter is due to different background counts between cameras and between restframe energies.

figure also indicates the signal-to-noise ratio of the injected signal, expressed as the total amount of simulated line photons over the square root of the total amount of photons in this energy bin as determined from a traditional stacking of the cells that contain groups (taking the proper blueshifting to restframe into account). It can be seen that even low SNR injected signals can be picked out by eye in some cases from the correlation.

The SNR for all injected signals is shown in Figure 5.4, separately for each instrument, and as a function of the input luminosity. Our sample has three injected signals below an SNR of 2, four signals between an SNR of 2 and 3, and SNR of 3 and higher starts at input luminosities of about $5 \cdot 10^{35}$ ph/s/$M_\odot$. We draw attention to the fact that such weak (low SNR) signals would be challenging to detect in traditional stacking analyses. For reference, the simulated signal contains on average 1 photon per group at an SNR of around 6 (there are 180 groups in the G11 sample up to a redshift of 1.0).

Below we will show the efficiency at which the injected simulated signals are recovered using a variety of estimators as described in Section 5.3. For the remainder of this section, all results shown are for the following choices for the computation of the correlation and the estimator. We limit the field to that of the zCOSMOS sample, and use the full G11 X-ray selected catalog of galaxy groups except for those that fall outside the zCOSMOS field. In the computation of the correlation we only use events detected at an energy greater than 200 eV and less than 10 keV, and use energy bins (in restframe) of 50 eV. The correlator used is M^γ/D^2 with $\{\gamma\} = \{0, 0.25, 0.75, 1.0, 1.25, 1.75, 2.25\}$, ie., we obtain a set of 7 correlations for different values of γ. The estimator Δ_γ is computed as

per Section 5.3, using 2 extra signal bins, 2 skipped bins and 3 side bins.

The best results are obtained using the approach where the set of Δ_γ are fit to a single component with a free β. The results are shown in Figure 5.5. The majority of all injected signals is recovered between 80 and 100% of the injected signal. High input luminosities are more likely to be correctly recovered. Essential is the fact that almost all best-fit β's are found within 10% of the correct value of 1. It is confirmed that the correct value for β is equally well recovered for simulated injected signals that scale as M^2 (not shown).

The efficiency of the other three estimators mentioned in Section 5.3 is shown for reference in Figure 5.6. The most naive estimator, to simply use $\Delta_{\gamma=1}$ and solve Equation 5.9 with a single $\beta = 1$ component, returns a distribution that is centered on a ratio of measured-to-input of 1, with quite a broad spread. Fitting to the set of correlators, like in Figure 5.5, but with β fixed to 1 gives a distribution similar to Figure 5.5 but with more outliers. Fitting the set of correlators to multiple components (5 in this case) does not work well at all. This will be discussed further in Section 5.8.

As mentioned in Section 5.5, bootstrap errors are employed to estimate uncertainties on the best-fit values of L_β (and β). These errors were already shown in the left panel of Figure 5.5 on the individual simulated signals, for 100 bootstrap realizations. We check the validity of this approach by comparing the distribution of recovery ratios of the injected signals to the distribution of recovery ratios in the bootstrap realizations with the same injected signals. To be clear, the bootstrap only resamples the field, it does not simulate additional realizations on the injected signal. As can be seen in Figure 5.7, the bootstrap distribution for best-fit β resembles closely that of the nominal injected signals in Figure 5.5. As was described before, the bootstrap resampling also changes the group catalog so that some realizations may contain much less significant signal than others. A less significant signal will be more difficult to recover, so that the bootstrap intervals would overestimate the uncertainty at the low-recovery end. Therefore, as mentioned, the bootstraps are performed in such a way that only realizations of the group catalog are used that are close in expected signal significance to the nominal group catalog. For a too lenient filtering, then, the error bars are overestimated. However a too strict filtering would defeat the purpose of the bootstrap method in the first place. We determined from trial-and-error that a requirement of similarity of 0.02 dex in terms of the ratio of the value of $\sum_k M_k / D_k^2$ is justified, but not stronger. As can be seen in Figure 5.7, the distribution of the bootstrap realizations is however broader and peaks at slightly lower ratios than the nominal distribution in Figure 5.5. Although the number of simulated signals is not very large, this may indicate that the bootstrap errors overestimate the true uncertainty interval, despite the filtering of the bootstrap realizations. The source of this is currently unknown, but we will continue to use the bootstrap estimation of the errors as a conservative measure.

The choice of which bins to use for the calculation of Δ_γ (Equation 5.10) is of course of impact on the results presented above. The choice presented was taken for providing a distribution that peaked close to 1 (based on trial-and-error). Taking fewer signal bins or fewer skipped bins typically reduces the recovery ratio, but therefore also reduced the probability of over-estimation. Performing the correlation with smaller bins allows more freedom to refine this choice, but also increases computation times.
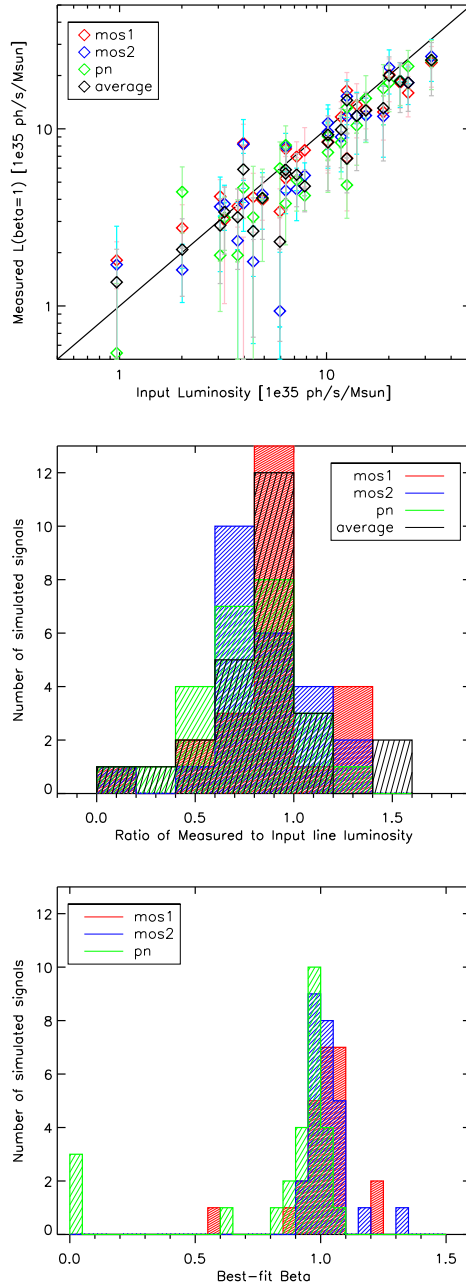
Figure 5.5: Recovery of injected decay signals using Δ_γ with M^γ/D^2 and $\{\gamma\} = \{0, 0.25, 0.75, 1.0, 1.25, 1.75, 2.25\}$ to fit a single component with L_β and β free parameters. In all panels, colors indicate the different detectors, and black is the weighted average of the detectors per injection. *Top:* for each individual injected signal the input luminosity and recovered L_β. Error bars indicate the distribution of 100 bootstrap realizations. *Middle:* histogram of the 26 injected signals in terms of the ratio of recovered to input signal. *Bottom:* histogram of the 26 injected signals in terms of the best-fit β.
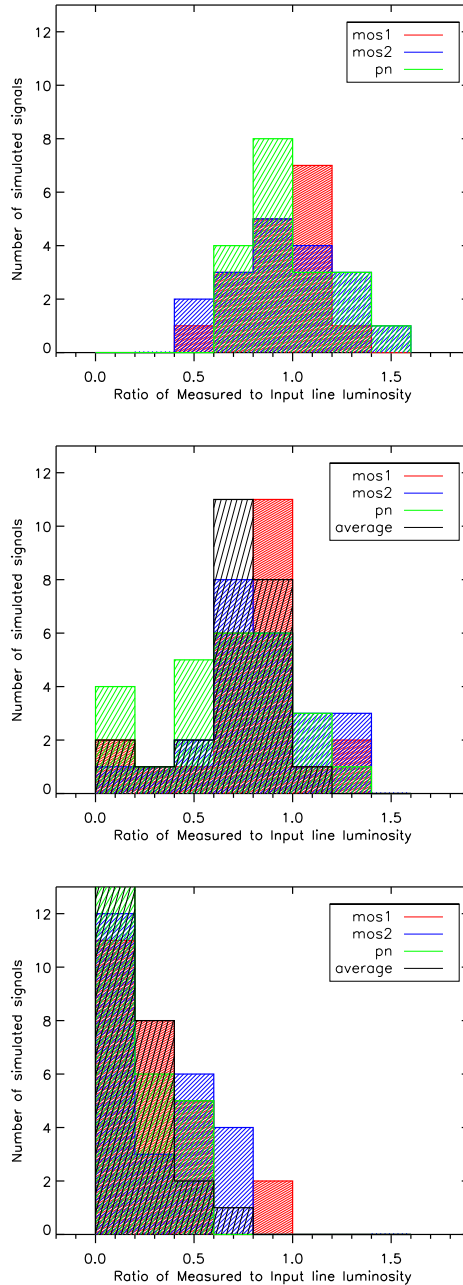
Figure 5.6: Recovery of injected decay signals using three different methods from Section 5.3. Shown as histograms of the 26 injected signals in terms of the ratio of recovered to input signal. In all panels, colors indicate the different detectors, and black is the weighted average of the detectors per injection. *Top:* directly solving Equation 5.9 for a single $\gamma = 1$ and a single $\beta = 1$ components. *Middle:* fitting Δ_γ with M^γ / D^2 and $\{\gamma\} = \{0, 0.25, 0.75, 1.0, 1.25, 1.75, 2.25\}$ to a single component with fixed $\beta = 1$. *Bottom:* fitting Δ_γ with M^γ / D^2 and $\{\gamma\} = \{0, 0.25, 0.75, 1.0, 1.25, 1.75, 2.25\}$ to five different components with $\{\beta\} = \{0.1, 0.5, 1.0, 1.5, 2.0\}$.
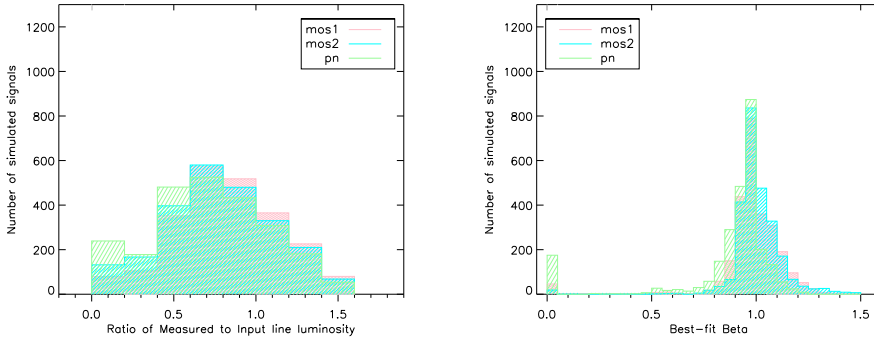
Figure 5.7: Same as Figure 5.5, but for all 100 bootstrap realizations of the 26 injected signals.

5.7   Conclusion and Summary

We have presented a new method to search for Dark Matter decay signals that does not rely on spectral modeling and does not require dedicated background subtraction. Both of these properties have been shown to be exhibited by our proof-of-concept implementation of the method on the COSMOS data using injected simulated Dark Matter decay signals.

The method relies on a spatial correlation and a correlation in redshift- and energy-space at the same time to automatically remove any and all backgrounds and foregrounds. The other main advantage is that by computing the correlation using different properties as the correlator, the behaviour of any correlated emission can be studied as a function of those properties. It is also possible to decompose the correlated emission into different components that behave differently. This method requires large datasets, but makes it possible to combine the advantages of a traditional stacking analysis with those of a population study (Sections 5.2 and 5.3).

We have performed a number of simulations of fake decay signals that have been injected into the real data, and subsequently attempted to recover this signal using our method. Our most effective estimator recovers the majority of the simulated signals to within 20 to 30% of the input luminosity, depending on the signal strength, and confirms its Dark Matter-like behavior (Section 5.6). It does so reliably for signals with a signal-to-noise ratio (raw photon count-based) as low as 3, without the need for any background subtraction or spectral modeling.

We expect that with more advanced fitting methods and considerable computing resources additional advantages of this method can be unlocked, such as independence of calibration uncertainties of both the instrument and the group properties (Section 5.8).

The sensitivity of the COSMOS dataset as a training set is not sufficient to reach the current state-of-the-art reported Dark Matter decay sensitivity, but the method is particularly well equipped to be scaled up and take advantage of all available archival data. As our simulations show that even very weak signals in terms of photon-count-based SNR have a good probability to be detected by our method, it is fully expected that it is possible to reach or surpass those sensitivities, while at the same time providing a robust tool for determining a potential signal's physical origin (Section 5.8).

5.8 Discussion

5.8.1 Decomposition Reliability

The estimator Δ_γ introduced in Section 5.3 requires a certain minimum of spectral information to detect line-like excesses. However, for weaker signals in regimes crowded with other emission lines (or other non-monotonic features) this approach may not work very well. In such a case it would be necessary to either take into account modeling of the full spectrum, or disregard any spectral information altogether. The latter being the main objective of the concept in this work. In this case, then, the Δ_γ estimator is skipped and the full set of $w_\gamma \langle I_\gamma \rangle$ is decomposed into a number of components as per Equation 5.9. Although in the current implementation presented in this work, the performance is sub-par, this approach offers dramatic advantages in the form of calibration independence once the reliability has been increased.

The results presented in Section 5.6 focused on decomposing the estimator Δ_γ into a single component with one or two free parameters. In the bottom panel of Figure 5.6, some results of a decomposition of $\{\Delta_\gamma\}$ into 5 components with a single free parameters each show that this approach did not work well in this case. Foregoing the estimator and employing the decomposition of the entire correlated signal delivers better results however. For the same set of correlators, the same fake injected signals and the same components (ie., components with the same β's), the results for the L_β component are shown in Figure 5.8. This is an improvement compared to the same decomposition but only relying on the estimator Δ_γ, but compares badly to the single-component estimators.

The main problem for the multi-component minimization procedure is likely that the coefficients $A_{\beta\gamma}$ from Equation 5.9 behave monotonically with both β and γ, which may incur some degeneracies if the number of components is too large. Additionally, it may not be clear what the ideal choice of β's should be for the decomposition. Although the $\beta = 1$ choice is clearly physically motivated, the usual astrophysical signals in a narrow energy bin may not necessarily scale as any power of the group mass, but rather as some more complicated function. The set of 5 values used above was chosen solely in order to provide enough opportunity for any signal that is not Dark Matter decay to 'choose' components with $\beta \neq 1$.

Possibilities for improvement then might be found along the following lines. Firstly, the decomposition may be performed with an intermediate number of components, such as a single $\beta = 1$ component and one or two components with a free (within some limits) β. Secondly, the correlators nor the components chosen neccesarily all have to be different powers of the same property. It should be possible to combine, for example, mass and temperature correlators, as long as the additive components of the decomposition are physically independent processes. Thirdly, the minimization procedure would likely profit, especially for more decompositions with more than 1 component, of a more advanced implementation, such as a Markov-chain Monte-Carlo method to more fully explore any degeneracies.
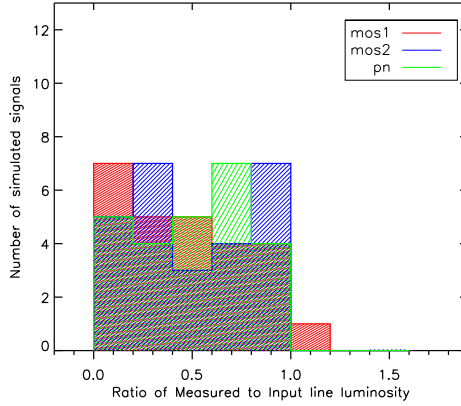
Figure 5.8: Recovery of injected decay signals using the full correlated signal $w_\gamma \langle I_\gamma \rangle$ with M^γ / D^2 and $\{\gamma\} = \{0, 0.25, 0.75, 1.0, 1.25, 1.75, 2.25\}$ to fit 5 components with $\{\beta\} = \{0.1, 0.5, 1.0, 1.5, 2.0\}$. The recovery rate leaves something to be desired, but is already better than those of the bottom panel of Figure 5.6. Possible improvements to this approach are discussed in Section 5.8.1.

5.8.2   Independence of Calibration Uncertainties

As alluded to earlier, the decomposition of the full correlated signal $w_\gamma \langle I_\gamma \rangle$ can be used to obtain an estimator that is independent of telescope and mass calibration. To be explicit, if the instrumental (mis-)calibration can be described as,

$$I = mI' + a$$

with I the measured X-rays flux, I' the true instrinsic X-ray flux, m a multiplicative calibration factor and a an additive calibration component; and if the mass calibration suffers only from a multiplicative bias so that $M = bM'$ with M the measured (reported) mass, M' the true mass and b the multiplicative bias; then the following estimator is insensitive to all of a, m and b:

$$Q_{\beta\gamma} \equiv \frac{L_\beta A_{\beta\gamma}}{w_\gamma \langle I_\gamma \rangle} \tag{5.14}$$

$$= \frac{L'_\beta A'_{\beta\gamma}}{w'_\gamma \langle I_\gamma \rangle'} = Q'_{\beta\gamma}$$

where all primed quantities represent the true values of the measured un-primed quantities. The derivation can be found in Appendix 5.A.2. The estimator $Q_{\beta\gamma}$ rather intuitively represents the fraction of the total correlated emission (the denominator) sourced by the component with exponent β. It also has the convenient property that

$$Q_\gamma \equiv \sum_{\{\beta\}} Q_{\beta\gamma} = 1 \tag{5.15}$$

by definition if the decomposition is perfect and noise-free.

The estimator effectively sacrifices any knowledge about the intrinsic value of any L_β (which is why Q still depends on γ) to get rid of the dependence on the calibration. The obvious advantage of this is that multiple instruments can be combined in order to increase sensitivity without introducing additional systematics related to calibration. We expect that it is also possible using this formalism to combine not just different instruments but also different fields and surveys without losing the benefits described above. As long as the type of object being correlated with is the same across surveys (ie, described by the same physics and thus by the same decomposition), the L_β measured from the decomposition should be the same for each survey performed with the same telescope (assuming the telescope calibration does not change between surveys, and that the mass calibration b is also the same for each survey). In that case, the L_β's from different surveys but the same instrument can be combined by some weighted average, or one may perform the fitting procedure to all surveys simultaneously, keeping the values of L_β tied between surveys (the coefficients $A_{\beta\gamma}$ will change between surveys). To obtain $Q_{\beta\gamma}$, a single survey has to be chosen as an arbitrary reference point. After all, the L_β are the same for each survey, but $A_{\beta\gamma}$, w_γ and $\langle I_\gamma \rangle$ are not. As long as the same survey is chosen as the reference point for each instrument, the Q's of the individual instruments can now also be combined to obtain a final single value for $Q_{\beta\gamma}$.

In principle, $Q_{\beta\gamma}$ can also be constructed for the estimator Δ_γ, without the loss of calibration independence. For single-component estimators however, the actual value of $Q_{\beta\gamma}$ does not provide a lot of insight, except that any deviation from the value of 1 is equal to the residual in the fitting process. The advantage would be found though in the ability to reduce the error bars by being able to combine results from different instruments without having to worry about calibration issues.

Since the full decomposition (without using the estimator Δ_γ) requires more advanced minimization or fitting implementations to deliver reliable results (see Section 5.8.1), and because in simulating the injected Dark Matter decay signals the available telescope response files are assumed to be correct, practical proof of the usefulness of this estimator Q will have to be postponed until future work that is able to employ a full suite of end-to-end simulations of the data.

5.8.3   Flexibility and Robustness

One advantage of this method is that when a candidate signal is found, it is possible to perform many tests by merely changing the parameters of the correlation and decomposition. A real signal should be present in all circumstances albeit with different significance. Jack-kniving is the first obvious possibility; the dataset can be split by redshift, by various properties of the objects in the catalog like mass or size, or by sky location. The process of bootstrapping already covers some of these variations in a way. Secondly, the object catalog can be changed. This may help root out possible selection bias. For example, if the X-ray coverage is not of uniform depth, the objects in an X-ray-selected catalog could be correlated with the exposure depth (see Section 5.4). Thirdly, even though the instrumental backgrounds cancel out very well on average (see Section 5.B), chance alignments of spectral and spatial inhomogeneities with catalog objects may occur. It is possible to check for robustness here by simply masking known instrumental lines in the raw data (observed frame). Because of the correlation being performed in redshift-space (object

restframe), any real signal will persist even though the significance will be lower over some energy range.

5.8.4   Sensitivity

With regards to the sensitivity to Dark Matter decay signals, this dataset is limited mostly by the total number of (expected) signal photons, as can be seen from the simulations in Section 5.6. Increasing the expected number of photons can be achieved in three ways; increased exposure depth, a larger number of objects in the group catalog, or a larger field. With increased photon statistics, it also becomes increasingly important to reduce the amount of noise in the correlation caused by chance alignments. Because the formalism depends on backgrounds (and other effects not related to the group catalog) canceling out on average, and because the field under consideration (or any field) is finite, some chance alignments between objects and some spatial or spectral inhomogeneities in the backgrounds are expected, inducing fluctuations in the correlation (see Section 5.B). Both higher object counts and larger fields (more cells) will improve the fidelity of correlation in this respect and thus reduce the (bootstrap) error bars. Note that the objects should have an appreciable range in redshifts for the correlation in redshift-space to work properly.

   The simulated signals in this work are stronger than what is already currently ruled out from previous studies. The 3.5 keV signal (Boyarsky et al., 2014a; Bulbul et al., 2014a), for example, would have an L_β of the order 0.1 ph s^{-1} $M_\odot{}^{-1}$, an order of magnitude weaker than the weakest signal we've simulated here.

5.A   Derivations

5.A.1   Correlation (De)composition

In this Appendix, Equation 5.9 is derived. We will write N_k for the correlator (which can represent any combination of properties of the galaxy group k). For readability, we will assume the X-rays consists of a single monochromatic Dark Matter decay component, and a homogeneous backgrounds component. We will generalize this later. The detected X-ray flux in a cell i at observed energy E' that contains a galaxy group at redshift z_i is then

$$I_i(E') = \delta\left[E'(1 + z_i) - E_0\right] LM_i/D_i^2 + I_{bg,i}(E') \tag{5.16}$$

with L the intrinsic luminosity per unit mass of the component, E_0 the restframe energy of this monochromatic component, M_i the group's mass and D_i^2 short for $4\pi D_{lum,i}^2$ representing the luminosity distance to the group. The δ-function makes sure the monochromatic component only contributes to $I_i(E')$ if $E' = E_0/(1 + z_i)$.

   We then put this into the equations for the correlation, where we will sometimes write a sum over N_{cwg} meaning all cells that contain a group, and we will use the shorthand

$\sum_k N_k$ to mean the sum over all groups in the catalog.

$$\frac{\langle NI(E)\rangle}{\langle N\rangle} = \frac{1}{N_C}\frac{N_C}{\sum_k N_k}\sum_i^{N_{\text{cwg}}}\sum_k^{N_g(i)}[I_i(E' = E/(1+z_k))N_k] \tag{5.17}$$

$$= \frac{1}{\sum_k N_k}\sum_i^{N_{\text{cwg}}}\sum_k^{N_g(i)}\left(\delta\big[(1+z_i)E/(1+z_k) - E_0\big]LM_kN_k/D_k^2\right.$$

$$\left. + I_{bg,i}\big(E/(1+z_k)\big)N_k\right) \tag{5.18}$$

Note that $\sum_i^{N_{\text{cwg}}}\sum_k^{N_g(i)}$ is just the same as the sum over all groups, so that $z_i = z_k$ in this summation;

$$\frac{\langle NI(E_0)\rangle}{\langle N\rangle} = \frac{L}{\sum_k N_k}\sum_k^{N_g}N_kM_k/D_k^2 + \frac{1}{\sum_k N_k}\sum_i^{N_{\text{cwg}}}\sum_k^{N_g(i)}I_{bg,i}\big(E_0/(1+z_k)\big)N_k \tag{5.19}$$

Repeat for $\langle I\rangle$

$$\langle I(E)\rangle = \frac{1}{N_C\sum_k N_k}\sum_i^{N_C}\sum_k^{N_g}\left[I_i\big(E' = E/(1+z_k)\big)N_k\right] \tag{5.20}$$

$$= \frac{1}{N_C\sum_k N_k}\sum_i^{N_{\text{cwg}}}\sum_k^{N_g}\left(\delta\big[(1+z_i)E/(1+z_k) - E_0\big]LM_iN_k/D_i^2\right)$$

$$+ \frac{1}{N_C\sum_k N_k}\sum_i^{N_C}\sum_k^{N_g}I_{bg,i}\big(E/(1+z_k)\big)N_k \tag{5.21}$$

Notice that the first double-summation runs over all cells *with a group* and all groups in the catalog, instead of *all* cells and all groups. Therefore, in this first double-sum, z_i and z_k are not always the same. At $E = E_0$, the δ-function however does enforce $z_i = z_k$, so that

$$\langle I(E_0)\rangle = \frac{L}{N_C\sum_k N_k}\sum_k^{N_g}N_kM_k/D_k^2 + \frac{1}{N_C\sum_k N_k}\sum_i^{N_C}\sum_k^{N_g}I_{bg,i}\big(E_0/(1+z_k)\big)N_k \tag{5.22}$$

Now we note that the parts from both $\langle NI\rangle/\langle N\rangle$ and $\langle I\rangle$ that contain I_{bg} and are on average equal if the background and the groups are uncorrelated (so that one might replace every $I_{bg,i}$ with I_{bg}). This leads to

$$w\langle I\rangle(E_0) = L\frac{\sum_k N_kM_k/D_k^2}{\sum_k N_k}\left(1 - \frac{1}{N_C}\right) \tag{5.23}$$

Since the number of cells is typically very large (more than 3000 in this work), the contribution of the correlated components to $\langle I\rangle$ is typically very small, ie. $(1 - 1/N_C) \simeq 1$.

This can be generalized by replacing the scaling M_k/D_k^2 with any other desired scaling (which we will represent with S_k).

If the component is constant in energy instead of monochromatic, the result would instead be

$$w\langle I\rangle = L\left(\frac{\sum_k N_k M_k/D_k^2}{\sum_k N_k} - \frac{\sum_k M_k/D_k^2}{N_C}\right) \tag{5.24}$$

and independent of energy. Again due to the factor $1/N_C$, in practice the change between monochromatic and constant in energy is about 1% at most for the dataset used in this work.

For completeness, we must note that for a single monochromatic component at E_0 the relevant part of $\langle NI(E_j)\rangle$ for any other $E_j \neq E_0$ will be zero, but the part of $\langle I(E_j)\rangle$ containing $L\delta((1+z_i)E_j/(1+z_k) - E_0)$ will not, as there may be pairs of (z_i, z_k) that solve $(1+z_i)E_j/(1+z_k) = E_0$. This reduces the correlation at every $E_j \neq E_0$, but only marginally due to the factor $1/N_C$.

Any arbitrary physical scenario can be expressed as the sum of many δ components at different energies E_s with their scalings S_s:

$$I_i = \sum_s L_s S_{s,i} + I_{bg,i} \tag{5.25}$$

The contributions to $\langle NI\rangle$ and $\langle I\rangle$ can then also simply be summed so that finally the generalized expression is

$$w\langle I\rangle = \sum_s L_s \frac{\sum_k N_k S_{s,k}}{\sum_k N_k}\left(1 - \frac{1}{N_C}\right), \tag{5.26}$$

neglecting as before the smearing of each δ-function as part of $\langle I\rangle$. This approximation may not work well if one is interested in components whose intrinsic luminosity (in terms of $L_s \sum_k N_k S_{s,k}/\sum_k N_k$) is of the order N_C smaller than the dominant component, setting a fundamental sensitivity limit for a given number of cells (ie, size of the field).

5.A.2 Calibration Independence

Here we will prove that $Q_{\beta\gamma}$ (Equation 5.14) is indeed independent of telescope and mass calibrations. The derivation is very similar to that of the previous Section. In this case however, we will suppress the explicit writing of energy dependence for now for readability.

Let I'_X be the true intrinsic X-ray emission from catalog objects in particular cell, I'_r any physical X-rays not sourced by and therefore not correlated with catalog objects, m the multiplicative calibration of the instrument and a the additive calibration of the instrument and the instrumental background. Let M' be an object's true mass, and b the multiplicative bias on that mass, so that $M = bM'$. Let L'_β be the true intrinsic luminosity per unit (mass$^\beta$/distance^2) for the X-ray emission component process that scales as (mass$^\beta$). Then the measured flux I_i in cell i will be

$$I_i = m(I'_X + I'_r) + a \tag{5.27}$$

$$= m\left(I'_r + \sum_{\{\beta\}} L'_\beta M'^\beta_i/D_i^2\right) + a \tag{5.28}$$

where the sum over the set of components $\{\beta\}$ runs over all physical processes at work (which we do not need to specify here).

Writing N_{cwg} for the number of cells that contain a group, $N_g(i)$ for the numbers of groups in cell i, then the measured quantities relate to the true quantities in the following way;

$$\langle N \rangle (\gamma) = \frac{1}{N_C} \sum_{k}^{N_g} b^\gamma M_k'^\gamma \tag{5.29}$$

$$= b^\gamma \langle N \rangle' (\gamma) \tag{5.30}$$

$$\langle NI \rangle (\gamma) = \frac{1}{N_C} \sum_{i}^{N_{\text{cwg}}} \sum_{k}^{N_g(i)} \left(mI_{r,i}' + a + \sum_{\{\beta\}} mL_\beta' M_i'^\beta / D_i^2 \right) \left(b^\gamma M_k'^\gamma \right) \tag{5.31}$$

$$= \frac{mb^\gamma}{N_C} \sum_{i}^{N_{\text{cwg}}} \sum_{k}^{N_g(i)} \left(\sum_{\{\beta\}} L_\beta' M_i'^\beta M_k'^\gamma / D_i^2 + I_{r,i}' M_k'^\gamma \right)$$

$$+ \frac{1}{N_C} \sum_{i}^{N_{\text{cwg}}} \sum_{k}^{N_g(i)} ab^\gamma M_k'^\gamma \tag{5.32}$$

$$= mb^\gamma \langle NI \rangle' (\gamma) + \frac{1}{N_C} \sum_{i}^{N_{\text{cwg}}} \sum_{k}^{N_g(i)} ab^\gamma M_k'^\gamma \tag{5.33}$$

$$\langle I \rangle (\gamma) = \frac{1}{N_C} \left(\sum_{l}^{N_g} b^\gamma M_l'^\gamma \right)^{-1} \left(\sum_{i}^{N_{\text{cwg}}} \sum_{k}^{N_g} m \sum_{\{\beta\}} L_\beta' M_i'^\beta b^\gamma M_k'^\gamma \right.$$

$$\left. + \sum_{i}^{N_C} \sum_{k}^{N_g} (I_{r,i}' m + a) b^\gamma M_k'^\gamma \right) \tag{5.34}$$

$$= m \langle I \rangle' (\gamma) + \frac{1}{N_C} \left(\sum_{l}^{N_g} M_l'^\gamma \right)^{-1} \sum_{i}^{N_C} \sum_{k}^{N_g} a M_k'^\gamma \tag{5.35}$$

The uncorrelated emission I_r is still part of $\langle I \rangle$ and $\langle NI \rangle$, both in the primed and unprimed quantities, but cancels out in w and $w\langle I \rangle$. Notice that in Equation 5.33 we can simplify

$$\frac{1}{N_C} \sum_{i}^{N_{\text{cwg}}} \sum_{k}^{N_g(i)} ab^\gamma M_k'^\gamma = \frac{1}{N_C} \sum_{k}^{N_g} ab^\gamma M_k'^\gamma , \tag{5.36}$$

and in Equation 5.35

$$\frac{1}{N_C} \left(\sum_{l}^{N_g} M_l'^\gamma \right)^{-1} \sum_{i}^{N_C} \sum_{k}^{N_g} a M_k'^\gamma = \left(\sum_{l}^{N_g} M_l'^\gamma \right)^{-1} \sum_{k}^{N_g} a M_k'^\gamma , \tag{5.37}$$

so that those parts cancel out below;

$$w(\gamma)\langle I\rangle(\gamma) = \frac{\langle NI\rangle(\gamma)}{\langle N\rangle(\gamma)} - \langle I\rangle(\gamma) \tag{5.38}$$

$$= m\left(\frac{\langle NI\rangle'(\gamma)}{\langle N\rangle'(\gamma)} - \langle I\rangle'(\gamma)\right) = mw'(\gamma)\langle I\rangle'(\gamma) \tag{5.39}$$

The decomposition of the different correlating components as described in Section 5.2 is now affected as follows. Recall that in Equation 5.9

$$A_{\beta\gamma} = \frac{\sum_k M_k^{\beta+\gamma}/D_k^2}{\sum_k M_k^{\gamma}}\left(1 - \frac{1}{N_C}\right) \tag{5.40}$$

so that $A_{\beta\gamma} = b^\beta A'_{\beta\gamma}$. All of the above means that the solutions to Equation 5.9 will be

$$L_\beta = \frac{m}{b^\beta}L'_\beta \tag{5.41}$$

We can then construct the following quantity that reflects which fraction of the correlated emission is explained by the component with exponent β

$$Q_{\beta\gamma} \equiv \frac{L_\beta A_{\beta\gamma}}{w(\gamma)\langle I\rangle(\gamma)} \tag{5.42}$$

$$= \frac{L'_\beta A'_{\beta\gamma}}{w'(\gamma)\langle I\rangle'(\gamma)}. \tag{5.43}$$

This quantity is completely independent of detector calibration and of multiplicative mass bias, as shown.

The energy dependence of m and a were not explicitly taken into account above for readability. Comparing with the previous section, it will be clear that this does not change the independence of $Q_{\beta\gamma}$. The energy dependence of a functions exactly like $I_{bg,i}$ in the previous section, which canceled out completely since it is an uncorrelated additive component. Regarding $m = m(E') = m(E/(1 + z_k)) \equiv m_k$, one may see that if this factor is introduced in the equations of the previous section, it becomes part of the summation like so

$$\frac{1}{\sum_k N_k}\sum_k^{N_g} m_k N_k M_k/D_k^2 \tag{5.44}$$

it is clear that the calibration of the instrument at some energy in the observed frame, $m(E')$, is uncorrelated with any properties of the group k. On average then, the preceding expression can be written as

$$\frac{1}{\sum_k N_k}\sum_k^{N_g} m_k N_k M_k/D_k^2 = \left(\frac{\sum_k m_k}{N_g}\right)\frac{\sum_k N_k M_k/D_k^2}{\sum_k N_k} \tag{5.45}$$

so that $\sum_k m_k/N_g$ can be associated with the factor m in Equations 5.33, 5.35, 5.39 and 5.41. All of which is to say that the intuitively expected

$$\frac{\langle NI\rangle}{\langle N\rangle\langle I\rangle} = \frac{\langle NmI'\rangle}{\langle N\rangle\langle mI'\rangle} = \frac{\langle m\rangle\langle NI'\rangle}{\langle N\rangle\langle m\rangle\langle I'\rangle}. \tag{5.46}$$

is confirmed to hold also when performing the correlation in redshift space.

5.B   Null Tests

One of the main features of this method is the fact that it automatically finds the correlated emission, and does not require separate background subtraction or modeling. This is possible because of the large field and object catalog, and because of the correlation in redshift space. To show that this feature works as claimed, we perform the following null test.

We first create a instrumental background-only facsimile version of the COSMOS field. This is achieved by using the available *XMM-Newton* closed-filter calibration observations. These observations are performed, as indicated by the name, while the filter wheel is in the closed position, blocking any physical emission, leaving only the instrumental backgrounds. To create a mosaic that resembles the actual instrumental background in the COSMOS observations, the closed filter dataset is cut into parts with roughly similar numbers of event counts as the real COSMOS exposures. Each part is then made a piece of the mosaic by using the `skycast` procedure to give all events sky coordinates.

The resulting mosaic is then used instead of the real data to compute the correlation as described above. The same catalogs are used, but in addition the correlation is performed on a number of randomized versions of the catalogs. So for each iteration, all objects in the catalog are assigned to a random cell. This means that all catalog properties remain the same, such as the redshift distribution.

We show the result of 40 of such randomized catalogs of the G11-sample, using as correlator M/D_{lum}^2, in Figure 5.9. The average of all the random catalogs is shown in red, and is very close to 0 for all energies, as is expected. The variation is shown in the red error bars, being the 68% intervals. This variation indicates the potential impact of chance alignments of objects in the catalog and spatial and spectral features in the instrumental backgrounds.

An additional on-the-spot null test can be included with every correlation. If the observed X-rays used for the correlation include events up to high energies, so that the telescope's effective area at these energies is essentially negligible, then the high-energy tail of the correlation spectrum should not include any correlated signal (up to some random fluctuations).

5.C   Weighted Correlations

Although in a sense the performing of a correlation could be described as a weighted average, strictly speaking the equations for $\langle NI \rangle$ and $\langle I \rangle$ (Equations 5.5 and 5.6) would be different if they both employed weighting by some cell's property in the form of

$$X = \frac{\sum_i x_i w_i}{\sum_i w_i}. \tag{5.47}$$

The difference with correlating is that weighting is used when there are certain properties of the cell that are not related to the correlating property of the groups *nor* to the correlating property of the cell, but which for some reason should increase or decrease how important this single cell is to the total.
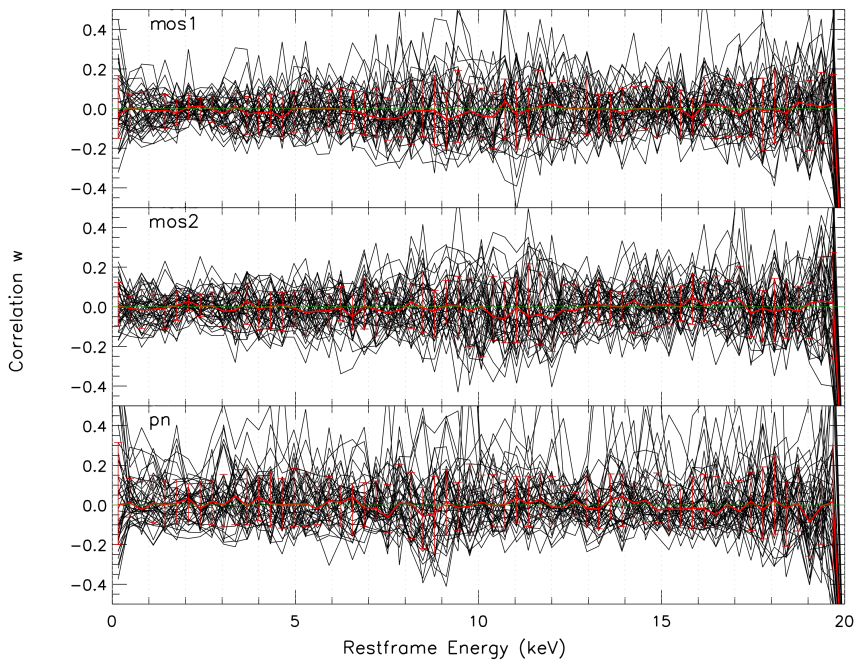
Figure 5.9: Results of the correlation for 40 randomized versions of the G11-sample. Median and 68% interval shown in red. Correlator used is M/D_{lum}^2, with energy bins of 320 eV.

We will here show for completeness how a weighting can be incorporated in the formalism, although one should beware that including a weight with residual relations between the quantities being correlated will induce systematic offsets.

Let us first rewrite $\langle I \rangle$

$$\langle I \rangle = \frac{1}{N_C} \sum_{i=1}^{N_C} \frac{1}{\sum_{l=1}^{N_g} N_l} \sum_{k=1}^{N_g} \zeta_{ik} N_k \tag{5.48}$$

$$= \frac{N_g}{\sum_{l=1}^{N_g} N_l} \frac{\displaystyle\sum_{i=1}^{N_C} \sum_{k=1}^{N_g} \zeta_{ik} N_k}{\displaystyle\sum_{i=1}^{N_C} \sum_{k=1}^{N_g} 1} \tag{5.49}$$

For $\langle NI \rangle$, we first observe that

$$\sum_{i=1}^{N_C} \frac{1}{N_C(i,\theta)} \sum_{j=1}^{N_C(i,\theta)} \sum_{k=1}^{N_g(j)} 1 = N_g \tag{5.50}$$

so that

$$\frac{\frac{1}{N_C} \displaystyle\sum_{i=1}^{N_C} \frac{1}{N_C(i,\theta)} \sum_{j=1}^{N_C(i,\theta)} \sum_{k=1}^{N_g(j)} \gamma(I_i, z_k) N_k}{\frac{1}{N_C} \displaystyle\sum_{i=1}^{N_C} \frac{1}{N_C(i,\theta)} \sum_{j=1}^{N_C(i,\theta)} \sum_{k=1}^{N_g(j)} 1} = \langle NI \rangle \frac{N_C}{N_g} \tag{5.51}$$

and we can write

$$\langle NI \rangle = \frac{N_g}{N_C} \frac{\displaystyle\sum_{i=1}^{N_C} \frac{1}{N_C(i,\theta)} \sum_{j=1}^{N_C(i,\theta)} \sum_{k=1}^{N_g(j)} \gamma(I_i, z_k) N_k}{\displaystyle\sum_{i=1}^{N_C} \frac{1}{N_C(i,\theta)} \sum_{j=1}^{N_C(i,\theta)} \sum_{k=1}^{N_g(j)} 1} \tag{5.52}$$

Now when adding the weights a_i the equations become

$$\langle NI \rangle = \frac{N_g}{N_C} \frac{\displaystyle\sum_{i=1}^{N_C} \frac{1}{N_C(i,\theta)} \sum_{j=1}^{N_C(i,\theta)} \sum_{k=1}^{N_g(j)} \gamma(I_i, z_k) N_k a_i}{\displaystyle\sum_{i=1}^{N_C} \frac{1}{N_C(i,\theta)} \sum_{j=1}^{N_C(i,\theta)} \sum_{k=1}^{N_g(j)} a_i} \tag{5.53}$$

$$\langle I \rangle = \frac{N_g}{\sum_{l=1}^{N_g} N_l} \frac{\displaystyle\sum_{i=1}^{N_C} \sum_{k=1}^{N_g} \zeta_{ik} N_k a_i}{\displaystyle\sum_{i=1}^{N_C} \sum_{k=1}^{N_g} a_i} \tag{5.54}$$

Initial tests of a weighting by each cell's product of exposure time, effective area and usable solid angle yielded systematic positive and increasing offsets at the high energy tail of the correlation spectrum (where it should be zero), for both the G11 sample and the 20k sample. We speculate this may be caused by telescope calibration uncertainty. Further application and study of any weights during the correlation was not pursued.

6 | APPENDICES

6.1 Comment on "A novel scenario for the possible X-ray line feature at ∼3.5 keV: Charge exchange with base sulfur ions"

Recently, Gu et al. (2015) suggested that the unidentified ∼3.5 keV line could have originated from via charge exchange between bare sulfur and neutral hydrogen interacting with a relative velocity of ∼ 200 km/s. New calculations of this interaction (Mullen et al., 2016) suggest that the dominant cross sections are to the $9p$ and $10p$ excited states of S XVI, leading to transitions at 3.45 keV and 3.46 keV, respectively. Although at lower energies, we agree that if present these transitions could affect the fits to the cluster spectra, as noted by Gu et al. (2015). However, Gu et al. (2015) also argues that these S XVI transitions are a "unique feature for probing CX in hot astrophysical plasmas," at least at CCD resolution. Although possibly true in the X-ray band, CX at the level implied by Gu et al. (2015) should also create detectable hydrogen Hα emission, although of course CX is not the only mechanism that could generate this line. The relationship between Hα and X-rays in clusters has been studied extensively; for example, Fabian et al. (2003) found that the Hα filaments in the Perseus cluster, which extend about 2 arcminutes in radius from the core, are associated with soft X-rays with a temperature of ∼ 0.9 keV.

To calculate the possible Hα flux, we will assume a typical cluster sulfur abundance of 1/3rd solar, or [S/H] = 6.72. Between 2-4 keV, the fractional population of fully stripped S^{16+} varies between ∼ 0.42 − 0.84; for concreteness, we use the value at 3 keV, 0.72, which also corresponds to the 200 km/s velocity where Mullen et al. (2016) find the

S^{16+} cross section peaks in the key $9p$ and $10p$ states. Inherent in the assumption that CX is occurring is that somehow the cluster contains a hot plasma mixing with a cool neutral plasma, possibly due to a cool infalling filament that is slowly "leaking" neutral hydrogen. In this case, the ionized hydrogen and neutral hydrogen can also interact, either via excitation or CX. To completely calculate the resulting Hα emission would require a complete level population calculation; we use a simpler approximation to this from McLaughlin (1999),

$$\sigma(H\alpha) = \sigma(1s \rightarrow 3s) + 0.118\sigma(1s \rightarrow 3p) + \sigma(1s \rightarrow 3d). \tag{6.1}$$

For the excitation and charge exchange cross sections, we use values from Table V of Winter (2009) at 3 keV, finding a total $\sigma(H\alpha) = 2.6 \times 10^{-18}\,\mathrm{cm}^{-2}$. Mullen et al. (2016) (via private communication) gives $\sigma(S^{16+} + H \rightarrow S^{15+}(9p, 10p) + H^+) \sim 3.3 \times 10^{-15}\,\mathrm{cm}^{-2}$. As the CX lines are at 3.45 keV, not 3.5 keV, they are not a one-for-one replacement for the $\sim$3.5 keV feature, but rather would impact the fits in this region in some complex fashion. It is reasonable to assume that any impact would become significant when the CX line had a similar flux as the $\sim$3.5 keV feature; in this case, we find:

$$F(H\alpha) = \frac{Ab(H)}{Ab(S)} \times \frac{\sigma(H\alpha) \times F_{3.5}}{\sigma(S^{16+} + H \rightarrow S^{15+}(9p, 10p) + H^+)} \tag{6.2}$$

or $F(H\alpha) \approx 150 \times F_{3.5}$. For Perseus, Bu14 found a range of values for $F_{3.5}$ depending upon the analysis approach. We use here the *XMM-Newton* MOS values found after excluding the core 1 arcminute radius, $2.1(+1.1, -1.0) \times 10^{-5}\,\mathrm{ph\,cm^{-2}s^{-1}}$ (90% errors). This implies that any potential cool plasma interaction would create Hα = $3.2(+1.8, -1.7) \times 10^{-3}\,\mathrm{ph\,cm^{-2}s^{-1}}$. Conselice et al. (2001) mapped all of the Hα filaments in Perseus, finding a total flux of $3.2 \times 10^{-13}\,\mathrm{erg\,cm^{-2}s^{-1}}$, or 0.11 photons $\mathrm{cm^{-2}s^{-1}}$. However, the majority of this emission was found within 1 arcminute (21 kpc) of the core. Excluding these points, however, reduces the observed flux to 9.5×10^{-3} photons $\mathrm{cm^{-2}s^{-1}}$.

Most of the filamentary Hα emission in Perseus must be created by other mechanisms within the filaments (collisional excitation, recombination, or photoionization), and not CX; otherwise, the bare sulfur CX line at 3.45 keV would be orders of magnitude stronger than it is. Similar conclusions are reached by e.g. Fabian et al. (2011) through different methods. By the same token, in the core of Perseus, CX could create both a 3.45 keV line and trace Hα emission that could not be detected. In other words, the Hα emission in the core of Perseus does not exclude a CX interpretation of the $\sim$3.5 keV line in the core. However, neither does the Hα measurements necessarily indicate that CX has to be responsible for either (part of) the 3.5 keV line or the Hα emitted at a flux as calculated above. Rather, we notice that the filamentary flux drops off much more rapidly from the core (more than an order of magnitude at 1 arcminute radius) than the $\sim$3.5 keV line, which only drops by a factor of 2, and suggest that this may be a distinguishing characteristic to be used in the future. More work is needed, both in the laboratory to test the theoretical CX calculations, and observational to compare the radial distributions of Hα emission in other clusters with the core-excluded $\sim$3.5 keV line, to conclusively identify the impact of CX.
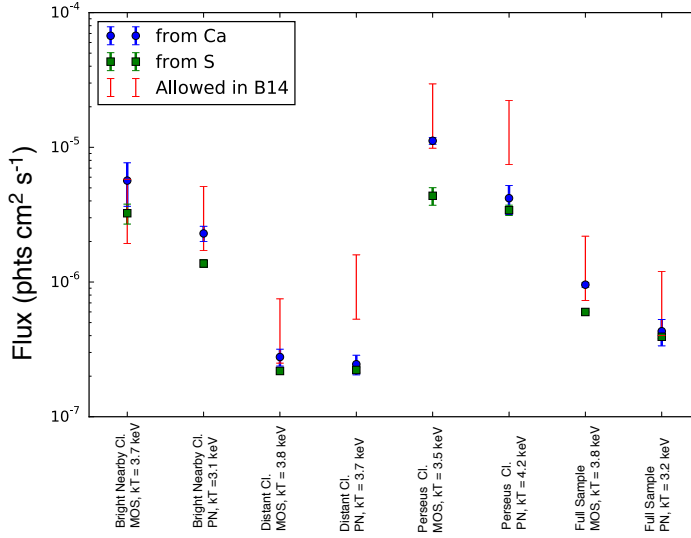
Figure 6.1: The estimated flux in the K XVIII triplet based on single temperature plasmas from the Bu14 samples. Blue - taken from Ca emission. Green - taken from S emission. Red - the calculated (lower end) and maximum allowed (upper end) flux of the triplet in Bu14.

6.2   Comment on "Discovery of a 3.5 keV line in the Galactic Centre and a critical look at the origin of the line across astronomical targets"

Jeltema & Profumo (2015) presented an analysis stating that if using a multi-component plasma and summing the fluxes from those using calcium to estimate the flux, the high temperature component would dominate, leading to a potentially large underestimate of the K XVIII triplet flux.

However, in our analysis we calculated the emissivity of the K XVIII triplet based on fluxes from both Ca and S, one of which peaks at a higher temperature, and one which peaks at a lower temperature. We have allowed for three times the maximum K XVIII flux permitted by either of these emissivity estimates as a safety margin. Crucially, the use of the S XVI emissivity, and not just the Ca, ensures that we have not underestimated the K XVIII triplet flux in the manner suggested by Jeltema & Profumo (2015).

To demonstrate this, we have estimated the flux of the K XVIII lines using another method, the results of which are shown in Figure 6.1. For each object listed in Bu14, the temperatures have been derived from the Ca XIX to Ca XX line ratio. These all lie in the range 3.1 keV to 4.2 keV. In those objects where we had extracted the S XV flux, the temperatures from the S XV to S XVI ratios were also found to lie in this range.

For each object, the emissivity of the K XVIII triplet has been calculated assuming that the plasma is a single temperature component plasma at the calculated temperature,

and that S, Ca and K are in collisional ionization equilibrium and they all have solar photosphere abundance (Anders & Grevesse 1989). By comparing the predicted flux ratios with the observed flux in the Ca and S lines, we produce estimated fluxes for the K XVIII triplet based on the Ca and S observations. Error bars indicate the range of fluxes implied by the 90% uncertainty in the Bu14 line fluxes. The red lines in the same figure show the range between the upper limit for the K XVIII flux calculated in that paper and that value with the factor of 3 safety margin included.

As can be seen, in the case of the MOS observations of the brightest clusters (the sum of Coma, Centaurus and Ophiuchus), the data shows that we have been conservative in our estimates of the maximum K XVIII flux, with estimates from this technique consistently falling at least a factor of two below the allowed values in Bu14.

6.3 Comment on "Where do the 3.5 keV photons come from? A morphological study of the Galactic Center and of Perseus"

Carlson et al. (2015) presents a morphological investigation of the ∼3.5 keV signal in the Galactic Center (GC) and the Perseus cluster, concluding that in a template-based maximum-likelihood approach neither object prefers a dark matter-like contribution.

However, using templates that are derived directly from a few broad energy bands of the data essentially reduces the spectral information that is available. Since the ∼3.5 keV flux in clusters is of order 1% of the continuum at *XMM-Newton*'s spectral resolution, it is essential to determine the continuum emission to better than 1%. This is a non-trivial exercise even in a forward modeling approach as done in Bo14 and Bu14, and is impossible in the template approach. This can be seen from the broad brackets of continuum models in Figures 5 and 6 of Carlson et al. (2015). If a continuum template is incorrect by more than a percent at 3.5 keV (which is almost a certainty), the ∼3.5 keV line contribution to the residual signal would be very subdominant, the residuals will be dominated by astrophysical components and, of course, follow the spatial distribution of the astrophysical templates, biasing the results against dark matter-like behaviour.

It should be noted in addition that the detection of the ∼3.5 keV signal in Bu14, using the same *XMM-Newton* MOS data as Carlson et al. (2015), has a significance of only about 3.4σ for the integrated data of the entire field of view (excluding the $1'$ cluster core). Given such low significance for the whole cluster, it is difficult to see how it would be possible to subdivide the dataset and obtain statistically significant measurements of the spatial behaviour of the line signal, as is for example suggested by the size of the error bars in Figure 6 of Carlson et al. (2015) or by their discussion of the perceived 'clumped nature' of the residuals in Section 3.1. The errors on the actual ∼3.5 keV line contribution in various sub-regions are likely understated.

Lastly, the effect of absorption by the intervening interstellar medium on the GC analysis is strongly underestimated in Carlson et al. (2015). They use the HI data to estimate the absorbing column density, concluding that absorption at 3.5 keV is insignificant (a few percent effect). While these data are adequate over most of the sky, at low Galactic latitudes the true X-ray absorption is often higher. Indeed, using *Chandra* X-ray spectra for

the GC fields, Muno et al. (2004) and Muno et al. (2004) measure the absorption column densities for various diffuse emission regions and for various point sources, respectively. They find median column densities close to 6×10^{22} cm^{-2}, while between 30 and 50% of the analyzed area has $N_H > 10^{23}$ cm^{-2}. This is much higher than the HI-based value; the excess can be due to molecular gas, etc. At 3.5 keV, such values of N_H correspond to attenuation by factor 2–3, not a few percent. These X-ray absorption measurements are directly applicable here, and were used in Bo14. This impacts any upper limits computed for dark matter decay. In addition, the absorption is likely irregularly distributed over the GC area (for example, the giant molecular clouds align with the Galactic plane), making an isotropic dark matter template inadequate.

7 | NEDERLANDSE SAMENVATTING

7.1 Introductie

Het concept Donkere Materie bestaat al sinds de jaren '30, toen Fritz Zwicky de naam voor het eerst bezigde bij wijze van beschrijving voor ontbrekende massa. Uit zijn observaties van het cluster van sterrenstelsels Coma bleek dat de snelheden van de individuele stelsels niet verklaard konden worden met de hoeveelheid zichtbare normale materie. De algemene acceptatie van het fenomeen heeft lang geduurd, maar het werkt van Vera Rubin en anderen heeft in de jaren '80 de argumenten van Zwicky kracht bijgezet door hetzelfde effect aan te tonen in de rotatiecurves van spiraalstelsels. Tegenwoordig is de Donkere Materie een essentieel onderdeel van het standaard model van de kosmologie. Dit model is in staat om de evolutie en de inhoud van het universum succesvol te beschrijven aan de hand van slechts een gering aantal ingrediënten. Naast de bekende materie en de Donkere Materie, bevat het Universum ook Donkere Energie die ervoor zorgt dat het universum (versneld) uitdijt. Over de ware natuur of oorsprong van deze component tast men tot op heden nog in het complete duister. Daarnaast bevat het standaardmodel een beschrijving van de eerste momenten in het bestaan van het heelal, de begincondities. Al deze ingrediënten zijn afgeleid uit het geheel van waarnemingen en vertegenwoordigen niet alleen een goede beschrijving van het heelal, maar ook het enige zelf-consistente model dat op het moment bestaat. Dat alles wil niet zeggen dat het standaard model van de kosmologie niet zijn eigen mysteries heeft. De gewone materie maakt slechts 5% van de inhoud van het Universum uit. De rest komt voor de rekening van de Donkere Energie (70%) en de Donkere Materie (25%). Van geen van beide donkere componenten is bekend wat de ware natuur is. Dit proefschrift gaat over de vraag waar de Donkere Materie uit bestaat.

Er zijn veel verschillende onafhankelijke meetingen te verrichten die allemaal aangeven dat er een grote hoeveelheid massa ontbreekt in het heelal in het algemeen en in verschillende individuele objecten. Niet alleen dat, maar elk van deze experimenten wijst op eenzelfde hoeveelheid Donkere Materie. De bewijzen voor het bestaan van Donkere Materie bevatten tegelijkertijd ook aanwijzingen over de eigenschappen van de Donkere Materie. Een van de meest directe en sterkste argumenten is te vinden in waarnemingen van de kosmische microgolf achtergrond straling (ook wel afgekort tot CMB in het En-

gels). Dit is de straling die is vrijgekomen op het moment dat het heelal doorzichtig werd voor licht, en is dus het oudst mogelijke signaal dat te observeren is. Deze straling komt uit elke richting en is zeer gelijkmatig verspreid over de hemel. Desalniettemin bevat het kleine temperatuur variaties. Uit de statistische verdeling van deze fluctuaties - hoeveel, hoe sterk en hoe groot - valt af te leiden hoe het plasma ten tijde van de uitzending van deze straling zich gedroeg. Dit plasma oscilleerde namelijk onder invloed van zijn eigen zwaartekracht en de interne druk. De eerder genoemde statistieken zijn echter niet consistent als het plasma alleen zijn eigen zwaartekracht voelt. Er is een extra component nodig die wel aantrekkingkracht heeft via de zwaartekracht maar die geen interne druk opwekt, maar materie met zulke eigenschappen is onbekend.

Deze achtergrondstraling is dus sterk bewijs voor het bestaan van materie die zich niet zo gedraagt als alle normale materie die bekend is. Evenzo zijn er andere experimenten die op dezelfde conclusie uitkomen. Daaruit is af te leiden dat de Donkere Materie een aantal kenmerken moet hebben. Het belangrijkste kenmerk is derhalve dat het 'donker' is, dat wil zeggen dat de Donkere Materie geen interacties heeft met gewone materie of met licht en andere straling. Dit is in essentie de *raison d'être* van de term, namelijk dat Donkere Materie een vorm van massa moet zijn die inert is ten opzichte van alle andere materie en die de eigen aanwezigheid slechts verraadt via de zwaartekracht. De Donkere Materie moet ook weinig interactie vertonen met zichzelf. Dat wil zeggen dat het geen interne druk en geen onderlinge botsingen ervaart. Als dat wel het geval zou zijn, zou deze materie, ook al is het 'donker', niet de waarnemingen van onder andere de microgolf achtergrondstraling verklaren. Aangetekend moet worden dat een totale afwezigheid van (zelf-)interacties niet strikt noodzakelijk is, alswel dat deze zo zwak zijn dat zij niet waarneembaar zijn met de huidige technieken. Tenslotte zijn er restricties wat betreft de massa van het Donkere Materie deeltje. Deze mag niet te licht zijn omdat de formatie van de grote structuren in het Universum (zoals sterrenstelsels en clusters van sterrenstelsels) dan niet meer gereproduceerd kan worden omdat de deeltjes dan te grote snelheden hebben.

Het is waarschijnlijk dat de Donkere Materie bestaat uit nieuwe, vooralsnog onbekende, fundamentele deeltjes. Het Standaard Model van de elementaire deeltjes is weliswaar erg succesvol, toch zijn er nog een aantal fenomenen die het niet kan verklaren. Het is namelijk mogelijk om een groot scala van theoretische deeltjes toe te voegen zonder de huidige werking van het standaard model aan te tasten. Zo zijn er ook veel mogelijkheden om een theoretisch deeltje toe te voegen dat de eigenschappen heeft van de Donkere Materie. Een van de meest populaire deeltjes is de zogenaamde WIMP, wat in het Engels staat voor 'zwak-wisselwerkend massief deeltje'. De populariteit komt voort uit de eigenschap van dit soort deeltje dat als de sterkte van de interactie van dit deeltje zich bevindt op de schaal van de Zwakke Kerngracht, dat dan de juiste hoeveelheid Donkere Materie wordt gevormd in het vroege heelal zolang het deeltje maar ongeveer een massa heeft van tussen de 1 en 1000 protonen. Een dergelijk deeltje zou echter snel uit elkaar vallen, waardoor het niet meer de rol van kosmologische Donkere Materie zou kunnen vervullen. Daarom worden deze deeltjes stabiel gehouden door een nieuwe symmetrie(lading). Het is echter wel mogelijk voor kosmologische Donkere Materie om instabiel te zijn zolang de vervaltijd maar lang genoeg is; veel langer dan de leeftijd van het universum. In dat geval moet de sterkte van de interactie veel zwakker zijn, en dan mag de massa van het deeltje ook lager zijn, tussen ongeveer de massa van een electron en een duizendste daarvan. Dit

soort deeltjes wordt ook wel aangeduid als 'super-WIMP', en is nog steeds zwaar genoeg om te voldoen aan alle Donkere Materie vereisten.

Bij het verval van een super-WIMP komt er een Röntgen foton vrij (omdat de massa van de deeltje van de orde van keV is). Omdat deze deeltjes zo licht zijn (slechts een fractie van de massa van een electron), zouden er gigantische hoeveelheden van nodig zijn om alle Donkere Materie te verklaren. Ondanks dat de vervaltijd van een individueel deeltje veel langer is dan de leeftijd van het heelal, is het te verwachten dat als er extreem veel deeltjes zijn er echter wel vaak genoeg een deeltje vervalt om dit process waar te nemen op een menselijke tijdschaal. Er bestaat geen *a priori* argument dat het meer of minder waarschijnlijk maakt dat een bepaald hypotetisch deeltje de Donkere Materie is. Daarom is het van belang dat veel verschillende mogelijke scenarios worden onderzocht. Dit proefschrift gaat over de zoektocht naar het verval signaal van mogelijke super-WIMP Donkere Materie.

De super-WIMP categorie bevat veel verschillende mogelijke deeltjes. In dit proefschrift wordt vaak melding gemaakt van een specifieke kandidaat, het steriele neutrino. Dit is een uitbreiding van het standaard model met een variant van het normale (actieve) neutrino dat geen enkele interactie heeft met alle andere deeltjes, behalve via zeldzame oscillaties met de actieve neutrinos. Deze deeltjes zijn niet alleen interessant omdat ze Donkere Materie zouden kunnen zijn, maar ze zouden ook helpen om een aantal andere vraagstukken te beantwoorden, namelijk waarom gewone neutrinos massa hebben en oscilleren, en waarom het universum uit materie bestaat en niet uit anti-materie. Het steriele neutrino wordt in dit proefschrift vaak gebruikt als referentie model voor vervallende Donkere Materie, maar al het werk is even zo goed toepasbaar op andere vervallende Donkere Materie.

7.2 Hoofdstuk 2 - Ontdekking van Kandidaat Donkere Materie Signaal op 3.5 keV

Het verwachte signaal van het verval van Donkere Materie is een lijn in het Röntgen spectrum van objecten die veel Donkere Materie bevatten. De sterkte van het signaal hangt af van de vervaltijd van de Donkere Materie, de hoeveelheid Donkere Materie die binnen het gezichtsveld van de telescoop valt en de afstand tot het object. Ondanks dat het signaal van een object dat verder weg staat zwakker is, zijn vergelijkbare signalen te verwachten als het verderweg gelegen object groter is. Daardoor zijn zowel sterrenstelsels als clusters van sterrenstelsels goede doelen om te zoeken naar Donkere Materie. In dit eerste hoofdstuk is gezocht naar een verval signaal in het sterrenstelsel Andromeda (M31) en het Perseus cluster. Dit zijn de objecten waarvan een relatief sterk signaal te verwachten is, gebaseerd op de grootte en hoe ver weg ze staan. De spectra van deze objecten zijn uitvoerig bestudeerd en gemodelleerd. Vooral het Perseus cluster zendt veel Röntgen straling uit die is veroorzaakt door de grote hoeveelheid extreem heet plasma. Al deze reguliere Röntgen emissie is zo goed mogelijk gemodelleerd, maar in beide objecten blijft een spectrale lijn over op 3.5 keV die niet geässocieerd kan worden met een astrofysisch process.

Kan dit signaal het verval van Donkere Materie zijn? Om antwoord te geven op die vraag moet eerst aannemelijk gemaakt worden dat het hier niet gaat om een systematisch

of instrumenteel effect, of om reeds bekende emissie processen. Het gaat waarschijnlijk niet om een instrumenteel artefact vanwege de volgende drie voornaamste redenen. Ten eerste is er geen lijn te bekennen op 3.5 keV in zeer lange observaties van relatief 'lege' stukken hemel. Een instrumenteel effect zou een significant signaal moeten hebben geproduceerd in deze waarnemingen. Ten tweede staat het Perseus cluster verder weg dan M31, waardoor het licht van Perseus roodverschoven is zodat een signaal dat uitgezonden is op, bijvoorbeeld, 3.5 keV gedetecteerd wordt met een lagere energie. In het geval van Perseus is het signaal inderdaad verschoven, en komt na correctie voor deze verschuiving de energie van het signaal op dezelfde waarde als dat voor M31. Een instrumenteel effect zou niet verschuiven. Ongeveer een week voor de openbaarmaking van de studie in dit hoofdstuk is een ander artikel gepubliceerd die in andere data hetzelfde signaal heeft ontdekt (Bulbul et al., 2014). Deze data bestaat uit een 'opstapeling' van observaties van veel verschillende objecten. Deze objecten stonden allemaal op een andere afstand, en de opstapeling wordt uitgevoerd nadat voor de roodverschuiving is gecorrigeerd. Met andere woorden, een signaal dat daadwerklijk uitgezonden wordt door deze objecten blijft zichtbaar in deze opstapeling, terwijl een instrumenteel effect uitgesmeerd zou worden. Tenslotte is dit signaal gedetecteerd met meerdere instrumenten, zowel in de studie beschreven in dit hoofdstuk, als in de studie door Bulbul.

Dat het niet gaat om een regulier astrofysisch signaal is aannemelijk te maken door te kijken naar andere aanwezige spectraal lijnen. In heet plasma worden hele specifieke transities geëxciteerd die zorgen voor het uitzenden van emissielijnen. Elk ion heeft zijn eigen karakteristieke set van emissielijnen op bepaalde energieën. Hoe sterk elk van deze lijnen is, hangt af van de temperatuur van het plasma en de hoeveelheid ionen die aanwezig zijn. Het signaal op 3.5 keV bevindt zich in het spectrum dichtbij mogelijke Argon en Kalium lijnen - te dichtbij voor het instrument om het verschil duidelijk te kunnen waarnemen. Door de sterkte van de 3.5 keV lijn te vergelijken met andere lijnen (idealiter andere lijnen van Argon of Kalium), kan er bepaald worden of het waarschijnlijk is dat de 3.5 keV lijn verklaard kan worden door Argon of Kalium emissie. In het geval van M31 is de 3.5 keV lijn de sterkste lijn in het spectrum. Dit zou zeer onwaarschijnlijk zijn als het om Argon of Kalium gaat, in dat geval zouden er ook andere sterkere lijnen aanwezig moeten zijn. In de opstapeling van clusters in de Bulbul studie gaat een soortgelijk argument op, namelijk dat er van de orde 10 tot 20 keer zoveel Argon of Kalium aanwezig moet zijn dan dat normaal gesproken aannemelijk is, om te verklaren waarom de Argon of Kalium lijn in de buurt van 3.5 keV zo sterk zou zijn als waargenomen.

Als het signaal geen instrumentele oorsprong heeft, noch een reguliere emissielijn is, staat nog niet vast dat het een signaal van vervallende Donkere Materie betreft, bij gebrek aan andere verklaringen. Om iets te kunnen zeggen over de Donkere Materie interpretie, moet de sterkte van de lijn vergeleken worden met wat er verwacht wordt van het verval van Donkere Materie. De verwachtte sterkte schaalt rechtevenredig met de hoeveelheid Donkere Materie in het gezichtsveld van de telescoop, en omgekeerd evenredig met de afstand tot het object in het kwadraat. Het is dan mogelijk om de waarnemingen van de verschillende objecten met elkaar te vergelijken, of om de verdeling van het signaal binnen een object te bestuderen. De Donkere Materie dichtheid binnen een (cluster van) sterrenstelsel(s) neemt namelijk op karakteristieke wijze af richting de buitenkant (veel langzamer dan bijvoorbeeld de sterkte van reguliere emissielijnen). Alhoewel de foutmarges op zowel de gemeten sterkte van de 3.5 keV lijn en de hoeveelheid Donkere

Materie in de objecten vrij groot zijn, zijn de waarnemingen van de lijn in M31 en in Perseus consistent met de interpretatie dat de lijn veroorzaakt wordt door het verval van Donkere Materie.

In het tweede deel van Hoofdstuk 2 wordt een belangrijke test uitgevoerd. Bepaald hebbende dat de 3.5 keV een kandidaat signaal is voor het verval van Donkere Materie, zou men verwachten dat er ook een zeer sterk signaal waar te nemen moet zijn vanuit het centrum van de Melkweg, omdat daar een vrij grote hoeveelheid Donkere Materie is te vinden, en voornamelijk omdat het zeer dichtbij staat vergeleken met alle andere mogelijke bronnen. Het centrum van de Melkweg is echter een zeer complex systeem wat betreft de Röntgen emissie, wat het modelleren van het spectrum zeer uitdagend maakt. In de observaties is weldegelijk een sterke lijn op 3.5 keV waargenomen. In dit specifieke geval is het niet uit te sluiten dat het om een reguliere emissie lijn gaat, alhoewel het ook niet noodzakelijkerwijs om reguliere emissie hoeft te gaan. Het belang van deze observaties is dat als er geen 3.5 keV signaal gevonden was, de interpretatie van de 3.5 keV lijn als het verval van Donkere Materie onmiddelijk gefalsificeerd zou zijn.

7.3 Hoofdstuk 3 - Het 3.5 keV Signaal in het Draco Dwergstelsel

Alle studies naar de oorsprong van het 3.5 keV signaal maken gebruik van archief data. Er is echter weinig data beschikbaar van dwergsterrenstelsel, objecten die erg geschikt zouden zijn om de 3.5 keV lijn te onderzoeken. Deze stelsels zijn kleine satelliet stelsels van de Melkweg, die relatief veel Donkere Materie bevatten en maar weinig heet gas. Daarnaast staan ze relatief dichtbij. Het verwachte signaal is niet heel sterk, maar wel waarneembaar bij genoeg observatie tijd. Het voordeel is dat er geen enkele reguliere astrofysische emissie verwacht wordt. Detectie van een 3.5 keV lijn vanuit een dwergstelsel zou dus een sterk argument kunnen zijn voor de vervallende Donkere Materie interpretatie.

Omdat er niet genoeg archief data beschikbaar is om een lijn van de verwachte sterkte te kunnen detecteren, zijn nieuwe waarnemingen uitgevoerd van het Draco dwergstelsel. Dit hoofdstuk beschrijft deze data en de resultaten van het modelleren van het spectrum. Helaas is er geen definitieve conclusie te trekken over de 3.5 keV lijn. In het spectrum van Draco in het ene instrument is slechts een zwak (niet erg significant) signaal gevonden, en in het andere instrument blijft detectie uit. Het verschil tussen de detectoren valt te verklaren door de verschillende gevoeligheid van de instrumenten. Ook vergeleken met de hoeveelheid Donkere Materie die verwacht wordt aanwezig te zijn in Draco, is deze non-detectie statistisch consistent met de andere 3.5 keV observaties. Samengevat is de hint van een 3.5 keV signaal in Draco niet sterk genoeg om te kunnen stellen dat het signaal er zeker is en dus een argument voor de Donkere Materie interpretatie vormt, noch is het signaal te zwak om te kunnen stellen dat de Donkere Materie interpretatie uitgesloten is.

7.4 Hoofdstuk 4 - Het 3.5 keV Signaal in het Perseus cluster

Het Perseus cluster van sterrenstelsels is in de context van het 3.5 keV signaal al eerder onderzocht met verschillende telescopen in zowel het centrum als de buitenkanten van het cluster. Enkele van deze studies laten tegenstrijdige resultaten zien, en in het algemeen lijkt het Perseus cluster een wat te sterk 3.5 keV signaal te hebben in vergelijking met andere objecten. In dit Hoofdstuk worden de bestaande resultaten van Perseus met elkaar vergeleken, en wordt de data genomen met de *Suzaku* telescoop opnieuw uitgebreid onderzocht om zo de heersende tegenstrijdigheden in de literatuur te beslechten. Daarnaast wordt de voorheen niet-onderzochte data van de minder centrale delen van Perseus onderzocht om het gedrag van de 3.5 keV lijn als functie van afstand tot het centrum te bepalen.

In het centrum van Perseus is een zeer sterke 3.5 keV lijn aanwezig. Het is, net als bij de vorige onderzoeken, onwaarschijnlijk dat deze lijn wordt veroorzaakt door reguliere emissie. De emissie in het centrum is significant genoeg om het onder te verdelen in drie concentrische ringen. Buiten het centrum wordt geen 3.5 keV lijn gedetecteerd, maar het is wel mogelijk om limieten te bepalen met betrekking op de sterkte van de lijn als functie van de afstand tot het centrum. De detecties en de limieten op verschillende afstanden van het centrum van het cluster kunnen worden vergeleken met de verdeling van Donkere Materie in het cluster. Hiervoor worden de resultaten van verschillende onderzoeken uit de literatuur gebruikt naar deze verdeling. Binnen de foutmarges op zowel de sterkte van de lijn als op de verdeling van de Donkere Materie, is de oorsprong van de 3.5 keV lijn in Perseus consistent met het verval van Donkere Materie.

Gebaseerd op dezelfde literatuur resultaten voor de verdeling van de Donkere Materie binnen het cluster, worden de resultaten uit dit Hoofdstuk vergeleken met andere metingen van de 3.5 keV lijn in Perseus. Ook hier zijn de meeste waarnemingen consistent met vervallende Donkere Materie als oorsprong van het 3.5 keV signaal. Van de onderzoeken die tegenstrijdig waren is vastgesteld dat de betreffende analyse niet afdoende was.

Vergeleken met andere objecten is de 3.5 keV lijn in Perseus inderdaad helderder dan verwacht zou worden op basis van de gebruikelijke methode om de totale massa van het Perseus cluster te bepalen. Het is echter mogelijk om de resultaten met betrekking tot Perseus overeenstemming te laten bereiken met andere resultaten, als de massa van Perseus groter is, zoals door sommige andere methodes geïmpliceerd wordt. Het zou ook mogelijk zijn dat slechts een deel van de sterkte van het 3.5 keV in Perseus veroorzaakt wordt door reguliere emissie zodat de 'werkelijke' sterkte lager zou zijn.

Om het vraagstuk van de oorsprong van het 3.5 keV signaal te beslechten, is de hoop voornamelijk gericht op nieuwe instrumenten. Korte raketvluchten met een instrument met superieure spectrale resolutie aan boord zou waarnemingen van de Melkweg kunnen maken, die vanwege de betere resolutie verschil zou moeten kunnen maken tussen een signaal van het verval van Donkere Materie en reguliere emissie van heet plasma. Een ruimte telescoop met vergelijkbare kwaliteit als de huidige instrumenten maar met een veel groter gezichtsveld kan binnen enkele jaren de hele hemel observeren. Door wederom het opstapelen van de vele objecten die in deze dataset aanwezig zullen zijn, kan een hoge statistische kracht bereikt worden.

7.5 Hoofdstuk 5 - Een Nieuwe Methode voor de Zoektocht naar het Verval van Donkere Materie

In dit hoofdstuk wordt een nieuwe methode ontwikkeld om te zoeken naar het verval van Donkere Materie die de nadelen van traditionele methoden vermijdt. Het onderzoek in de voorgaande hoofdstukken naar de 3.5 keV lijn berust voor een groot deel op het modelleren met hoge precisie van de spectra van individuele objecten. De nadelen inherent hieraan zijn in de eerste plaats dat er per object maar een beperkte hoeveelheid data beschikbaar is, en ten tweede dat een zwak signaal bij het modelleren erg gevoelig kan zijn voor het samenspel van onderling ontaardde spectrale componenten. Om vervolgens de oorsprong van het signaal te onderzoeken moet het signaal vergeleken worden tussen verschillende objecten, maar voor ieder object afzonderlijk zijn de foutmarges vaak groot.

Eén gedeeltelijke oplossing is om een opstapeling te maken van meerdere objecten, en het resulterende gecombineerde spectrum te modelleren. Hierdoor kan de hoeveelheid gebruikte data vergroot worden evenals de statistische kracht. Tegelijkertijd wordt het echter moeilijker om het spectrale model te interpreteren, en de individuele objecten kunnen niet meer met elkaar worden vergeleken.

Om zowel de statistische kracht van het combineren van data van verschillende objecten, als het onderscheidend vermogen van het vergelijken van de objecten te behouden in een enkele analyse is een correlatiemethode ontwikkeld. De twee basis ingrediënten zijn ten eerste een vrij groot aaneengesloten veld van Röntgen waarnemingen, opgedeeld in een raster waarbij elke cel een eigen spectrum heeft. Ten tweede een catalogus van de verdeling van Donkere Materie in dit raster, gerepresenteerd door groepen van sterrenstelsels. De correlatie is in essentie en in de meest eenvoudige implementatie dan het verschil tussen de totale Röntgenstraling gemiddeld over het hele veld, en de gemiddelde Röntgenstraling in cellen waar zich groepen sterrenstelsels bevinden. Door tijdens het nemen van deze gemiddelden te corrigeren voor de roodverschuiving van iedere groep sterrenstelsels isoleert deze methode automatisch louter die Röntgenstraling die daadwerkelijk uitgezonden worden door de groepen. Bij wijze van spreke 'herkent' de correlatie welk deel van de Röntgenstraling bij de groepen hoort en welk deel niet doordat het spectrum van de groepen 'beweegt' naar gelang de roodverschuiving van de groepen.

Vervolgens kan de correlatie op verschillende manieren uitgevoerd worden. De catalogus bevat informatie over de massa van iedere groep van sterrenselsels. In plaats van de Röntgenstraling te correleren met slechts de aanwezigheid (of niet) van een groep, kan er gecorreleerd worden met de massa van iedere groep. Of er kan gecorreleerd worden met de massa van iedere groep in het kwadraat, of met de massa tot welke andere macht dan ook. Als bekend is hoe een inherent signaal in werkelijkheid schaalt met de massa van een groep (d.w.z met welke exponent van de massa), kan berekend worden hoe de correlatie moet veranderen als functie van de exponent van de massa waarmee de correlatie wordt uitgevoerd. Door vervolgens de correlatie uit te voeren met verschillende exponenten van de massa, en te bestuderen hoe de correlatie telkens verandert, kan afgeleid worden wat de inherente schaling is van Röntgenstraling. Het signaal van het verval van Donkere Materie schaalt als de massa tot de eerste macht. Als de bovenstaande analyse concludeert dat er op één bepaalde energie een emissie component bestaat die schaalt als de massa tot de eerste macht, mag dat beschouwd worden als een zeer sterke aanwijzing dat het verval

van Donkere Materie is waargenomen.

Om het concept in andere woorden uit te drukken, deze correlatie methode offert kennis van de individuele datapunten op om tot slechts twee getallen te komen die samen uitdrukken of er al dan niet een verval signaal van Donkere Materie in de data is te ontdekken.

De methode wordt in dit Hoofdstuk ontwikkeld en getest op bestaande archiefdata waar gesimuleerde verval signalen aan zijn toegevoegd. De methode is in staat om signalen te detecteren die in een traditionele analyse moeilijk te detecteren zouden zijn, en om tegelijkertijd te bevestigen dat het inderdaad om een verval signaal gaat, iets wat met traditionele methoden niet mogelijk is. Deze dataset is echter niet gevoelig genoeg om tot conclusies te kunnen komen wat betreft de oorsprong van het 3.5 keV signaal. Dit is in de toekomst mogelijk door meer archiefdata (en data van nieuwe waarnemingen) te combineren, iets waar deze methode uitermate geschikt voor is.

BIBLIOGRAPHY

Abazajian, K., Fuller, G. M., & Tucker, W. H. 2001, Astrophys. J., 562, 593

Abazajian, K. N., Markevitch, M., Koushiappas, S. M., & Hickox, R. C. 2007, Phys. Rev. D , 75, 063511

Abbey, T., Carpenter, J., Read, A., et al. 2006, in ESA Special Publication, Vol. 604, The X-ray Universe 2005, ed. A. Wilson, 943

Ackerman, L., Buckley, M. R., Carroll, S. M., & Kamionkowski, M. 2009, Phys. Rev., D79, 023519, [,277(2008)]

Adhikari, R., Agostini, M., Ky, N. A., et al. 2016, ArXiv e-prints, arXiv:1602.04816

Alcock, C., Allsman, R. A., Axelrod, T. S., et al. 1996, ApJ , 461, 84

Alcock, C., et al. 2000, Astrophys. J., 542, 281

Alvarez, P. D., Conlon, J. P., Day, F. V., Marsh, M. C. D., & Rummel, M. 2015, JCAP, 1504, 013

Anders, E., & Grevesse, N. 1989, Geochim. Cosmochim. Acta, 53, 197

Anderson, M. E., Churazov, E., & Bregman, J. N. 2015, MNRAS , 452, 3905

Arnaud, K. A. 1996, in A.S.P. Conference Serie, Vol. 101, Astronomical Data Analysis Software and Systems V, ed. G. H. Jacoby & J. Barnes (San Francisco, ASP), 17

Arnaud, M. 2005, in Proceedings, International School of Physics "Enrico Fermi", 159th Course, "Background Microwave Radiation and Intracluster Cosmology": Varenna, Italy, July 6-16, 2004

Asaka, T., Blanchet, S., & Shaposhnikov, M. 2005, Phys. Lett., B631, 151

Asplund, M., Grevesse, N., Sauval, A. J., & Scott, P. 2009, Ann.Rev.Astron.Astrophys., 47:481-522,2009, 0909.0948

Battaglia, G., et al. 2005, Mon. Not. Roy. Astron. Soc., 364, 433

Battaglia, G., Helmi, A., Morrison, H., et al. 2006, MNRAS , 370, 1055

Baudis, L. 2013, Nuclear Physics B Proceedings Supplements, 235, 405

Bautz, M. W., Miller, E. D., Sanders, J. S., et al. 2009, PASJ, 61, 1117

Bekenstein, J. D. 2004, Phys. Rev., D70, 083509, [Erratum: Phys. Rev.D71,069901(2005)]

Bennett, C. L., Larson, D., Weiland, J. L., et al. 2013, ApJS, 208, 20

Bernal, N., & Palomares-Ruiz, S. 2012, JCAP, 1, 6

Bertone, G., Hooper, D., & Silk, J. 2005, Phys. Rept., 405, 279

Binney, J. J., & Evans, N. W. 2001, MNRAS , 327, L27

Boehringer, H., & Werner, N. 2009, ArXiv e-prints, arXiv:0907.4277

Boyarsky, A., den Herder, J. W., Neronov, A., & Ruchayskiy, O. 2007a, Astropart. Phys.,

28, 303

Boyarsky, A., Franse, J., Iakubovskyi, D., & Ruchayskiy, O. 2014b, ArXiv e-prints, arXiv:1408.4388

—. 2015, Physical Review Letters, 115, 161301

Boyarsky, A., Iakubovskyi, D., & Ruchayskiy, O. 2012, Phys.Dark Univ., 1, 136

—. 2013, Physics of the Dark Universe, Volume, 1,, Issue1,p.136

Boyarsky, A., Iakubovskyi, D., Ruchayskiy, O., & Savchenko, V. 2008a, MNRAS , 387, 1361

Boyarsky, A., Malyshev, D., Neronov, A., & Ruchayskiy, O. 2008b, MNRAS , 387, 1345

Boyarsky, A., Neronov, A., Ruchayskiy, O., & Shaposhnikov, M. 2006a, MNRAS , 370, 213

—. 2006b, Phys. Rev. D , 74, 103506

Boyarsky, A., Neronov, A., Ruchayskiy, O., Shaposhnikov, M., & Tkachev, I. 2006c, Phys. Rev. Lett., 97, 261302

Boyarsky, A., Neronov, A., Ruchayskiy, O., & Tkachev, I. 2010a, Phys.Rev.Lett., 104, 191301

Boyarsky, A., Nevalainen, J., & Ruchayskiy, O. 2007b, A&A, 471, 51

Boyarsky, A., & Ruchayskiy, O. 2008, arXiv:0811.2385

Boyarsky, A., Ruchayskiy, O., & Iakubovskyi, D. 2009a, JCAP, 0903, 005

Boyarsky, A., Ruchayskiy, O., Iakubovskyi, D., & Franse, J. 2014a, Physical Review Letters, 113, 251301

Boyarsky, A., Ruchayskiy, O., Iakubovskyi, D., Maccio', A. V., & Malyshev, D. 2009b, ArXiv e-prints, arXiv:0911.1774

Boyarsky, A., Ruchayskiy, O., Iakubovskyi, D., et al. 2010b, MNRAS , 407, 1188

Boyarsky, A., Ruchayskiy, O., & Markevitch, M. 2008c, ApJ , 673, 752

Boyarsky, A., Ruchayskiy, O., & Shaposhnikov, M. 2009c, Ann. Rev. Nucl. Part. Sci., 59, 191

Brandt, W. N., & Hasinger, G. 2005, Ann. Rev. Astron. Astrophys., 43, 827

Brunner, H., Cappelluti, N., Hasinger, G., et al. 2008, A&A, 479, 283

Bulbul, E., Markevitch, M., Foster, A., et al. 2016a, ArXiv e-prints, arXiv:1605.02034

—. 2014a, ApJ , 789, 13

Bulbul, E., Markevitch, M., Foster, A. R., et al. 2014b, ArXiv e-prints, arXiv:1409.4143

Bulbul, E., Randall, S. W., Bayliss, M., et al. 2016b, ApJ , 818, 131

Burkert, A. 1995, ApJ , 447, L25+

Carlson, E., Jeltema, T., & Profumo, S. 2015, JCAP, 2, 9

Carter, J. A., & Read, A. M. 2007, A&A, 464, 1155

Chemin, L., Carignan, C., & Foster, T. 2009, Astrophys. J., 705, 1395

Chen, Y., Reiprich, T. H., Bohringer, H., Ikebe, Y., & Zhang, Y. Y. 2007, A&A, 466, 805, [Astron. Astrophys.466,805(2007)]

Churazov, E., Forman, W., Jones, C., & Bohringer, H. 2003, Astrophys. J., 590, 225

Cicoli, M., Conlon, J. P., Marsh, M. C. D., & Rummel, M. 2014, Phys. Rev., D90, 023540

Cline, J. M., Farzan, Y., Liu, Z., Moore, G. D., & Xue, W. 2014, Phys. Rev., D89, 121302

Clowe, D., Bradac, M., Gonzalez, A. H., et al. 2006, ApJ , 648, L109

Colless, M., et al. 2001, Mon. Not. Roy. Astron. Soc., 328, 1039

Conrad, J. 2014, 1411.1925

Conselice, C. J., Gallagher, III, J. S., & Wyse, R. F. G. 2001, AJ, 122, 2281

Corbelli, E., Lorenzoni, S., Walterbos, R. A. M., Braun, R., & Thilker, D. A. 2010, A&A, 511, A89

Dar, A. 1995, Astrophys. J., 449, 550, [,21(1995)]

De Luca, A., & Molendi, S. 2004, Astron. Astrophys., 419, 837

Deason, A. J., Belokurov, V., Evans, N. W., & An, J. 2012, MNRAS , 424, L44

Dekel, A., Stoehr, F., Mamon, G. A., Cox, T. J., & Primack, J. R. 2005, Nature, 437, 707

Dodelson, S. 2011, Int. J. Mod. Phys., D20, 2749

Dodelson, S., & Widrow, L. M. 1994, Phys. Rev. Lett., 72, 17

Dolgov, A. D., & Hansen, S. H. 2002, Astropart. Phys., 16, 339

Donato, F., Gentile, G., Salucci, P., et al. 2009, MNRAS , 397, 1169

Duffy, A. R., Schaye, J., Kay, S. T., & Dalla Vecchia, C. 2008, MNRAS , 390, L64, [Erratum: Mon. Not. Roy. Astron. Soc.415,L85(2011)]

El Aisati, C., Hambye, T., & Scarn, T. 2014, JHEP, 08, 133

Ellis, J. 2012, Philosophical Transactions of the Royal Society of London Series A, 370, 818

Essig, R., Kuflik, E., McDermott, S. D., Volansky, T., & Zurek, K. M. 2013, arXiv:1309.4091

Ettori, S., De Grandi, S., & Molendi, S. 2002, A&A, 391, 841

Fabian, A. C., Sanders, J. S., Crawford, C. S., et al. 2003, MNRAS , 344, L48

Fabian, A. C., Sanders, J. S., Williams, R. J. R., et al. 2011, MNRAS , 417, 172

Famaey, B., & McGaugh, S. S. 2012, Living Reviews in Relativity, 15, doi:10.1007/lrr-2012-10

Feng, J. L., & Kumar, J. 2008, Phys. Rev. Lett., 101, 231301

Figueroa-Feliciano, E., Anderson, A. J., Castro, D., et al. 2015, ApJ , 814, 82

Finkbeiner, D. P., & Weiner, N. 2014, ArXiv e-prints, arXiv:1402.6671

Foster, A. R., Ji, L., Smith, R. K., & Brickhouse, N. S. 2012, Astrophys. J., 756, 128

Foster, A. R., Smith, R. K., Ji, L., & Brickhouse, N. S. 2011, in 2010 NASA Laboratory Astrophysics Workshop, C2

Frandsen, M. T., Sannino, F., Shoemaker, I. M., & Svendsen, O. 2014, JCAP, 1405, 033

Franse, J., Bulbul, E., Foster, A., et al. 2016, The Astrophysical Journal, 829, 124

Frenk, C. S., & White, S. D. M. 2012, Annalen Phys., 524, 507

Garzilli, A., Boyarsky, A., & Ruchayskiy, O. 2015, ArXiv e-prints, arXiv:1510.07006

Geehan, J. J., Fardal, M. A., Babul, A., & Guhathakurta, P. 2006, MNRAS , 366, 996

Gentile, G., Famaey, B., Zhao, H., & Salucci, P. 2009, Nature , 461, 627

Gentile, G., Salucci, P., Klein, U., Vergani, D., & Kalberla, P. 2004, MNRAS , 351, 903

George, M. R., Leauthaud, A., Bundy, K., et al. 2011, ApJ , 742, 125

Geringer-Sameth, A., Koushiappas, S. M., & Walker, M. 2015, ApJ , 801, 74

Gizis, J. E., Mould, J. R., & Djorgovski, S. 1993, PASP, 105, 871

Gondoin, P., Aschenbach, B., Erd, C., et al. 2000, in Proc. SPIE, Vol. 4140, X-Ray and Gamma-Ray Instrumentation for Astronomy XI, ed. K. A. Flanagan & O. H. Siegmund,

1–12

Gorbunov, D., Khmelnitsky, A., & Rubakov, V. 2008, JCAP, 0810, 041

Gripaios, B. 2015, 1503.02636

Gu, L., Kaastra, J., Raassen, A. J. J., et al. 2015, A&A, 584, L11

Hasinger, G., Cappelluti, N., Brunner, H., et al. 2006, Astrophys.J.Suppl., arXiv:astro-ph/0612311

Henley, D. B., & Shelton, R. L. 2012, Astrophys.J.Suppl., 202, 14

Higaki, T., Jeong, K. S., & Takahashi, F. 2014, Phys. Lett., B733, 25

Hoekstra, H., & Jain, B. 2008, Ann. Rev. Nucl. Part. Sci., 58, 99

Horiuchi, S., Humphrey, P. J., Oñorbe, J., et al. 2014, Phys. Rev. D , 89, 025017

Hu, W., & White, M. J. 1996, Astrophys. J., 471, 30

Iakubovskyi, D. 2013, PhD thesis, Instituut-Lorentz for Theoretical Physics

Iakubovskyi, D. 2014, Advances in Astronomy and Space Physics, 4, 9

Iakubovskyi, D. 2015, MNRAS , 453, 4097

Iakubovskyi, D., Bulbul, E., Foster, A. R., Savchenko, D., & Sadova, V. 2015, ArXiv e-prints, arXiv:1508.05186

Irby, B. 2008, The ftools webpage, HeaSoft, http://heasarc.gsfc.nasa.gov/docs/software/ftools/ftools_menu.html, `http://heasarc.gsfc.nasa.gov/docs/software/ftools/ftools_menu.html`

Jansen, F., Lumb, D., Altieri, B., et al. 2001, A&A, 365, L1

Jeltema, T., & Profumo, S. 2014, ArXiv e-prints, arXiv:1411.1759

—. 2015, MNRAS , 450, 2143

Jeltema, T. E., & Profumo, S. 2008, ApJ , 686, 1045

Jeltema, T. E., & Profumo, S. 2016, Mon. Not. Roy. Astron. Soc., 458, 3592

Kaastra, J. S., Mewe, R., & Nieuwenhuijzen, H. 1996, in UV and X-ray Spectroscopy of Astrophysical and Laboratory Plasmas, ed. K. Yamashita & T. Watanabe, 411–414

Kaiser, N. 1992, ApJ , 388, 272

Kalberla, P. M. W., Burton, W. B., Hartmann, D., et al. 2005, A&A, 440, 775

Kaneda, H., Makishima, K., Yamauchi, S., et al. 1997, ApJ , 491, 638

Kaplan, D. E., Luty, M. A., & Zurek, K. M. 2009, Phys. Rev., D79, 115016

Kent, S. M. 1986, AJ, 91, 1301

King, L. J., & Mead, J. M. G. 2011, MNRAS , 416, 2539

Kitayama, T., Bautz, M., Markevitch, M., et al. 2014, ArXiv e-prints, arXiv:1412.1176

Klypin, A., Zhao, H., & Somerville, R. S. 2002, ApJ , 573, 597

Knobel, C., et al. 2012, to appear

Komatsu, E., et al. 2011, ApJS, 192, 18

Kowalski, M., et al. 2008, Astrophys. J., 686, 749

Koyama, K., Kataoka, J., Nobukawa, M., et al. 2014, ArXiv e-prints, arXiv:1412.1170

Kuntz, K. D., & Snowden, S. L. 2008, A&A, 478, 575

Kusenko, A., Loewenstein, M., & Yanagida, T. T. 2013, Phys.Rev., D87, 043508

Laine, M., & Shaposhnikov, M. 2008, JCAP, 6, 31

Lee, B. W., & Weinberg, S. 1977, Phys. Rev. Lett., 39, 165

Lehmer, B. D., et al. 2007, Astrophys. J., 657, 681

Lesgourgues, J., & Pastor, S. 2006, Phys. Rept., 429, 307

Lilly, S. J., Le Fèvre, O., Renzini, A., et al. 2007, ApJS, 172, 70

Loewenstein, M., & Kusenko, A. 2010, Astrophys. J., 714, 652

—. 2012, Astrophys.J., 751, 82

Loewenstein, M., Kusenko, A., & Biermann, P. L. 2009, ApJ , 700, 426

Lovell, M. R., Bertone, G., Boyarsky, A., Jenkins, A., & Ruchayskiy, O. 2015, MNRAS , 451, 1573

Lovell, M. R., Frenk, C. S., Eke, V. R., et al. 2013, arXiv:1308.1399

Lovell, M. R., Eke, V., Frenk, C. S., et al. 2012, MNRAS , 420, 2318

Lumb, D. H., Warwick, R. S., Page, M., & De Luca, A. 2002, A&A, 389, 93

Malyshev, D., Neronov, A., & Eckert, D. 2014, Phys. Rev. D , 90, 103506

Mandelbaum, R., Seljak, U., & Hirata, C. M. 2008, JCAP, 0808, 006

Mantz, A. B., Allen, S. W., Morris, R. G., et al. 2014, MNRAS , 440, 2077

Markevitch, M., Gonzalez, A. H., Clowe, D., et al. 2004, Astrophys. J., 606, 819

McLaughlin, D. E. 1999, ApJ , 512, L9

McMillan, P. J. 2011, MNRAS , 414, 2446

Merloni, A., Predehl, P., Becker, W., et al. 2012, ArXiv e-prints, arXiv:1209.3114

Merrifield, M. R. 1992, AJ, 103, 1552

Milgrom, M. 1983, ApJ , 270, 365

Mirabal, N. 2010, MNRAS , 409, L128

Mirabal, N., & Nieto, D. 2010, arXiv:1003.3745

Mitsuda, K., Kelley, R. L., Akamatsu, H., et al. 2014, in Society of Photo-Optical Instrumentation Engineers (SPIE) Conference Series, Vol. 9144, Society of Photo-Optical Instrumentation Engineers (SPIE) Conference Series, 2

Moffat, J. W., & Toth, V. T. 2011, ArXiv e-prints, arXiv:1112.4386

Moniez, M. 2010, Gen. Rel. Grav., 42, 2047

Moore, B., Quinn, T., Governato, F., Stadel, J., & Lake, G. 1999, MNRAS , 310, 1147

Moretti, A., Pagani, C., Cusumano, G., et al. 2009, A&A, 493, 501

Mullen, P. D., Cumbee, R. S., Lyons, D., & Stancil, P. C. 2016, ArXiv e-prints, arXiv:1602.02401

Muno, M. P., Baganoff, F. K., Bautz, M. W., et al. 2004, ApJ , 613, 326

Muno, M. P., Arabadjis, J. S., Baganoff, F. K., et al. 2004, ApJ , 613, 1179

Navarro, J. F., Frenk, C. S., & White, S. D. M. 1997, ApJ , 490, 493

Neronov, A., Boyarsky, A., Iakubovskyi, D., & Ruchayskiy, O. 2014, Phys. Rev., D90, 123532

Nesti, F., & Salucci, P. 2013, JCAP, 7, 16

Nevalainen, J., Markevitch, M., & Lumb, D. 2005, ApJ , 629, 172

Okabe, N., Umetsu, K., Tamura, T., et al. 2014, Publ.Astron.Soc.Jap., 66, 99

Olive, K. A., et al. 2014, Chinese Physics C, 38, 090001

Oort, J. H. 1940, ApJ , 91, 273

Peter, A. H. G. 2012, arXiv:1201.3942

Porquet, D., Grosso, N., Predehl, P., et al. 2008, A&A, 488, 549

Press, W. H., & Schechter, P. 1974, ApJ , 187, 425

Read, A. M., & Ponman, T. J. 2003, A&A, 409, 395

Refregier, A., Helfand, D. J., & McMahon, R. G. 1997, ApJ , 477, 58

Reiprich, T. H., & Boehringer, H. 2002, ApJ , 567, 716

Riemer-Sorensen, S. 2014, ArXiv e-prints, arXiv:1405.7943

Riemer-Sorensen, S., & Hansen, S. H. 2009, A&A, 500, L37

Riemer-Sørensen, S., Hansen, S. H., & Pedersen, K. 2006, ApJ , 644, L33

Riemer-Sørensen, S., Pedersen, K., Hansen, S. H., & Dahle, H. 2007, Phys. Rev. D , 76, 043524

Rubin, V. C., Thonnard, N., & Ford, Jr., W. K. 1980, Astrophys. J., 238, 471

Ruchayskiy, O., Boyarsky, A., Iakubovskyi, D., et al. 2015, arXiv:1512.07217

Sánchez-Conde, M. A., Cannoni, M., Zandanel, F., Gómez, M. E., & Prada, F. 2011, JCAP, 12, 11

Sanders, R. H. 2014, Can.J.Phys., 93:, 1

Sarazin, C. L. 1997, ASP Conf. Ser., 116, 375

Schneider, A. 2015, MNRAS , 451, 3117

—. 2016, JCAP, 4, 059

Scoville, N., Aussel, H., Brusa, M., et al. 2007, ApJS, 172, 1

Seigar, M. S., Barth, A. J., & Bullock, J. S. 2008, MNRAS , 389, 1911

Sekiya, N., Yamasaki, N. Y., & Mitsuda, K. 2015, PASJ, arXiv:1504.02826

Serlemitsos, P. J., Soong, Y., Chan, K.-W., et al. 2007, PASJ, 59, 9

Shaposhnikov, M. 2008, JHEP, 08, 008

Shi, X.-d., & Fuller, G. M. 1999, Phys. Rev. Lett., 82, 2832

Simionescu, A., Allen, S. W., Mantz, A., Werner, N., & Takei, Y. 2012a, in American Institute of Physics Conference Series, Vol. 1427, American Institute of Physics Conference Series, ed. R. Petre, K. Mitsuda, & L. Angelini, 5–12

Simionescu, A., Allen, S. W., Mantz, A., et al. 2011, Science, 331, 1576

Simionescu, A., Werner, N., Urban, O., et al. 2012b, ApJ , 757, 182

Smith, M. C., Ruchti, G. R., Helmi, A., et al. 2007, MNRAS , 379, 755

Sofue, Y., Honma, M., & Omodaka, T. 2009, PASJ, 61, 227

Sonbas, E., Rangelov, B., Kargaltsev, O., et al. 2015, ArXiv e-prints, arXiv:1505.00216

Speckhard, E. G., Ng, K. C. Y., Beacom, J. F., & Laha, R. 2016, Physical Review Letters, 116, 031301

Springel, V., et al. 2005, Nature, 435, 629

Storm, E., Jeltema, T. E., Profumo, S., & Rudnick, L. 2013, Astrophys. J., 768, 106

Strüder, L., Briel, U., Dennerl, K., et al. 2001, A&A, 365, L18

Takahashi, H., Okada, Y., Kokubun, M., & Makishima, K. 2004, ApJ , 615, 242

Takahashi, T., Mitsuda, K., Kelley, R., et al. 2012, 8443, 1

Tamura, T., Iizuka, R., Maeda, Y., Mitsuda, K., & Yamasaki, N. Y. 2015, Publ. Astron. Soc. Jap., 67, 23

Tempel, E., Tamm, A., & Tenjes, P. 2007, Mon.Not.Roy.Astron.Soc., 707, arXiv:0707.4374

Tisserand, P., et al. 2007, Astron. Astrophys., 469, 387

Tremaine, S., & Gunn, J. E. 1979, Phys. Rev. Lett., 42, 407

Turner, M. J. L., Abbey, A., Arnaud, M., et al. 2001, A&A, 365, L27

Uchiyama, H., Nobukawa, M., Tsuru, T. G., & Koyama, K. 2013, PASJ, 65, 19

Urban, O., Werner, N., Allen, S. W., et al. 2015, MNRAS , 451, 2447

Urban, O., Simionescu, A., Werner, N., et al. 2014, MNRAS , 437, 3939

Viel, M., Haehnelt, M. G., & Springel, V. 2004, Mon. Not. Roy. Astron. Soc., 354, 684

Vikhlinin, A., Kravtsov, A., Forman, W., et al. 2006, ApJ , 640, 691

Vikhlinin, A., Burenin, R. A., Ebeling, H., et al. 2009, ApJ , 692, 1033

Walker, M. 2013, Dark Matter in the Galactic Dwarf Spheroidal Satellites, ed. T. D. Oswalt & G. Gilmore, 1039

Watson, C. R., Beacom, J. F., Yuksel, H., & Walker, T. P. 2006, Phys. Rev., D74, 033009

Watson, C. R., Li, Z.-Y., & Polley, N. K. 2012, JCAP, 3, 018

Weber, M., & de Boer, W. 2010, A&A, 509, A25

Weinberg, D. H., Bullock, J. S., Governato, F., de Naray, R. K., & Peter, A. H. G. 2013, 1306.0913

Widrow, L. M., & Dubinski, J. 2005, ApJ , 631, 838

Winter, T. G. 2009, Phys. Rev. A , 80, 032701

Wojtak, R., & Łokas, E. L. 2007, MNRAS , 377, 843

Worsley, M. A., Fabian, A. C., Bauer, F. E., et al. 2006, Mon. Not. Roy. Astron. Soc., 368, 1735

Xue, X. X., Rix, H. W., Zhao, G., et al. 2008, ApJ , 684, 1143

Yuksel, H., Beacom, J. F., & Watson, C. R. 2008, Phys. Rev. Lett., 101, 121301

Zandanel, F., Weniger, C., & Ando, S. 2015, JCAP, 9, 060

Zwicky, F. 1933, Helvetica Physica Acta, 6, 110

PUBLICATIONS

Refereed Publications

Radial Profile of the 3.55 keV Line out to R_{200} in the Perseus Cluster
J. Franse, E. Bulbul, A. Foster, A. Boyarsky, M. Markevitch, M. Bautz, D. Iakubovskyi, M. Loewenstein, M. McDonald, E. Miller, S.W. Randall, O. Ruchayskiy, R.K. Smith, 2016, Astrophys. J., **829**, 124.

Searching for Decaying Dark Matter in Deep XMM-Newton Observation of the Draco Dwarf Spheroidal
O. Ruchayskiy, A. Boyarsky, D. Iakubovskyi, E. Bulbul, D. Eckert, **J. Franse**, D. Malyshev, M. Markevitch, A. Neronov, 2016, Mon. Not. R. Astron. Soc., **460**, 1390.

Checking the Dark Matter Origin of a 3.53 keV Line with the Milky Way Center
A. Boyarsky, **J. Franse**, O. Ruchayskiy, D. Iakubovskyi, 2015, Phys. Rev. Lett., **115**, 161301.

Unidentified Line in X-Ray Spectra of the Andromeda Galaxy and Perseus Galaxy Cluster
A. Boyarsky, O. Ruchayskiy, D. Iakubovskyi, **J. Franse**, 2014, Phys. Rev. Lett., **113**, 251301.

Evolution of the Red Sequence Giant to Dwarf Ratio in Galaxy Clusters out to z $\sim$0.5
C. Bildfell, H. Hoekstra, A. Babul, D. Sand, M. Graham, J. Willis, S. Urquhart, A. Mahdavi, C. Pritchet, D. Zaritsky, **J. Franse**, P. Langelaan, 2012, Mon. Not. R. Astron. Soc., **425**, 204.

Publications in Preparation and Unrefereed Publications

Novel Cross-Correlation Techniques in Weak Line Searches
J. Franse, *in preparation*.

Comment on the Paper "Dark Matter Searches Going Bananas: the Contribution of Potassium (and Chlorine) to the 3.5 keV Line" by T. Jeltema and S. Profumo
A. Boyarsky, **J. Franse**, O. Ruchayskiy, D. Iakubovskyi, 2014, *arXiv:1408.4388*.

Curriculum Vitae

I was born on February 14 1988 in Maarssen. I can not really remember a time when I was not interested in space. It must have been during my early science courses at the 'Christelijk Gymnasium' in Utrecht that I was captivated specifically by the most fundamental things, large and small.

Studying astronomy had been pretty much inevitable since, which I went to do in Leiden after graduating from high school in 2006. I must have liked it there, because I would stay there for the next ten years. Taking a year off during my bachelor studies I was on the board of the student society 'Catena' and learned things I never would have in any lectures. I obtained my bachelor degree in astronomy in 2010, graduating on a project with Henk Hoekstra on the evolution of the giant-to-dwarf ratio of galaxy clusters.

Enrolling for the masters in astronomy, I took the cosmology track (obviously) and would be part of the first wave of graduates in this de Sitter program (quite unbeknownst to me until the graduation). The first project was with Simon Portegies Zwart and Koen Kuijken using N-body simulations of galaxies in an external gravitational field in order to judge the strength of some systematic effects on gravitational lensing shear and flexion measurements. The final project of my masters degree would turn out to be a lead-up to my PhD. Some of the ideas and methods for the correlation project described in this Thesis were tentatively explored under supervision of Alexey Boyarsky.

I graduated cum laude in 2012, immediately to be followed by starting my PhD with Alexey Boyarsky and Ana Achúcarro as a de Sitter fellow in cosmology. The plan starting out was to first develop the basic ideas from the masters thesis on using correlations to look for Dark Matter decay into a mature methodology with accompanying code. That project became lower priority in early 2014, when a potential decay signal was discovered in archival data of galaxies and galaxy clusters. That discovery resulted in three full chapters in this Thesis, with the last one being filled up, finally five years after the initial conception and with little time to spare, by the correlation method.

Acknowledgements

This thesis not only signifies the completion of my doctorate, but also the end of ten years at Leiden University. It has always been a great place to do and study astrophysics, and in ten years I've met a lot of great people at the institute and in Leiden, possibly too many to be able to express all my thanks to adequately on these few pages.

One of the things I appreciated most, was maybe the ease and politeness with which it was possible to have long and interesting discussions about so many topics ranging from science to politics and others. If I have spent more than 5 minutes talking to you, chances are you get my thanks for this. Thanks in particular to those who seemed the most willing (or unlucky) to humor me in this, Ricardo, David, Fabian, Massimo, Emanuelle (or should you be thanking me?), Henriette, Allison and Marcello.

Some people have been here as long as I have. Ricardo, we've trodden very similar paths here, shared many experiences during our studies, during conferences, and endured the inevitable hardships of a PhD student. Thank you for all that, the many conversations about science, politics and our careers, and dragging me along to the sports center.

Fabian, my thanks and appreciation for sharing in the 'de Sitter' journey. Being the first de Sitter fellows was an experience, thank you for your company at the many conferences and in organizing the journal clubs. Also thank you for disagreeing with me on so many political subjects over the years and the ensuing discussion.

Even though I had my office on the astronomy floors and didn't visit the second floor as often, I want to thank all the cosmology people at the Lorentz Institute - Wessel, Vicente, Valeri, Pablo, Kyrylo, Jesus, Bin, Bartosz, Artem, Andrii - for unerringly showing up at the journal clubs and participating eagerly. Bart and Yvette, thank you for taking over the organization of that journal club. To you and to Valeri and Dong-Gang all the best on your own de Sitter journeys. I also want to thank Antonella and Mark especially for the company during travels and conferences and the occasional spot of pleasant collaboration.

While on the subject of conferences, interestingly the astro-particle crowd from Amsterdam I've met more regularly abroad at conferences than in the Netherlands; Fabio, Richard, Michael, Sebastian, Hamish, Francesca, thank you as well for your company and insights.

Thanks to everyone from the Lensing group - Cristobal, Ricardo, Fabian, Marcello, Massimo, Margot, Marco, Remco, Jelte, Merijn, Maciej, Andrej, Martin, Christos, Vivianni, Berenice and Elisabetta - for letting me join your meetings and discussions, even though I stopped doing lensing related things some time ago.

I would like to thank Alexey and Ana for their supervision and guidance in many aspects of academic life. I thank Dima, Oleg and Esra for the successful and pleasant collaborations. Koen and Henk, I want to thank for generously remaining available after

my bachelor and master projects for valuable discussions and the odd piece of needed advice.

For essential help regarding computing and software, administration made all the more esoteric by being part of two institutes at once, and organizational matters, the support staff of both the Observatory and the Lorentz Institute deserve my thanks; Marianne, Fran, Barry, David, Erik, Aart, Roland, Alexandra, Anita, Arianne, Evelijn, Liesbeth.

For keeping the soul healthy with company and amusement, in situations inside and outside the institute(s), there are many people to thank. For trips and outings, craft beer tastings, playing basketball, a solar eclipse cruise, drinks and dinners and much more. Thank you fellow PhD's and differently-titled colleagues, present and past; Mason and Henriette (for literally all of the above), Ricardo, Fabian, David, Emanuelle, Edwin, Cristobal, Leah, Eva, Niels, Marijke, Allison, Cameron, Nico, Christian, Chris, Mike, Mieke, Andrew, Aayush, Vincent, Margot, Clement, Francois, Kirsten, Stephanie, Gabi, Heather, Marco, Berenice, Tiffany, Marissa, Monica, Mattia, Jesse, Alex, Bart, Luke, Anna-Lea, Paula and to everyone else that I hope I didn't forget.

Ik wil mijn ouders bedanken voor hun voortdurende steun en aanmoediging, en voor hun voorbeeld, waardoor ik kritisch op mijzelf én blij met mijzelf kan zijn. Wat betreft het kritisch zijn op mij, bedank ik ook mijn zusje, die altijd het beste met mij voor heeft.

I want to thank Ann-Sofie for her invaluable support and understanding, I can only hope you can say the same of me in a few years.